

DESIGNING IMMUNOTHERAPIES FOR CANCER TREATMENT

by

Zhuoya Wan

B.S. in Pharmacy Sichuan University, 2015

M.S. in Pharmaceutical Sciences, University of Pittsburgh, 2017

Submitted to the Graduate Faculty of the
School of Pharmacy in partial fulfillment
of the requirements for the degree of
Doctor of Philosophy

University of Pittsburgh

2021

UNIVERSITY OF PITTSBURGH

SCHOOL OF PHARMACY

This thesis was presented

by

Zhuoya Wan

It was defended on

October 26, 2021

and approved by

Robert Gibbs, Ph.D., Professor,

Department of Pharmaceutical Sciences, School of Pharmacy, University of Pittsburgh

Christian Fernandez, Ph.D., Associate Professor

Department of Pharmaceutical Sciences, School of Pharmacy, University of Pittsburgh

Da Yang, M.D., Ph.D., Associate Professor,

Department of Pharmaceutical Sciences, School of Pharmacy, University of Pittsburgh

Binfeng Lu, Ph.D., Professor

Department of Immunology, School of Medicine, University of Pittsburgh

Thesis Advisor/Dissertation Director: **Song Li**, M.D., Ph.D.

Department of Pharmaceutical Sciences, School of Pharmacy, University of Pittsburgh

Copyright © by Zhuoya Wan

2021

DESIGNING IMMUNOTHERAPIES FOR CANCER TREATMENT

Zhuoya Wan, M.S.

University of Pittsburgh, 2021

The immunosuppressive tumor microenvironment (TME) represents one of the hallmarks of cancer and underlies the basis for immune evasion and acquired immunotherapy-resistance for cancer therapy. Significant clinical success has been made in cancer treatment through blocking the T cell checkpoints, such as cytotoxic T lymphocyte antigen 4 (CTLA-4) and Programmed Death 1 (PD-1). However, only a subset of patients respond to such approaches.

The reason of non-response is very complicated. On the one hand, additional immunosuppressive mechanisms exist in the TME. A better understanding of the mechanism that regulates the immunosuppressive TME plays a crucial role for developing more efficacious immunotherapies and combination strategies. Here, we reported a novel role of the metabotropic glutamate receptor-4 (GRM4) in suppressing the anti-tumor immunity. We revealed in three murine syngeneic tumor models (B16, MC38, and 3LL) that either genetic knockout (*Grm4*^{-/-}) or pharmacological inhibition led to significant delay in tumor growth and synergized with immune checkpoint inhibitors in male mice. Mechanistically, perturbation of GRM4 resulted in a strong anti-tumor immunity by promoting natural killer (NK), CD4⁺ and CD8⁺ T cells towards an activated, proliferative, and functional phenotype. Single-cell RNA-sequencing and T Cell Receptor (TCR) profiling further defined the clonal expansion and immune landscape changes in CD8⁺ T cells. Mechanistically, *Grm4*^{-/-} intrinsically activated IFN- γ production in CD8⁺ T cells through a cAMP/CREB-mediated pathway. Our study appears to be of clinical significance as a

signature of NK^{high}-GRM4^{low} and CD8^{high}-GRM4^{low} correlated with improved survival in melanoma patients. Therefore, targeting GRM4 could be exploited as a new approach for cancer immunotherapy.

Alternatively, the use of free drug raises the issue of water-solubility, rapid blood elimination and metabolism. Improvement in drug bioavailability and/or codelivery of multiple drugs via a nanocarrier represents a promising strategy to improve therapeutic outcome and patient compliance. We developed a dual-function immuno-stimulatory polymeric prodrug carrier modified with pendent indoximod, an indoleamine 2,3-dioxygenase (IDO) inhibitor that can be used to reverse immune suppression, for co-delivery of Doxorubicin (Dox), a hydrophobic anticancer agent that can promote immunogenic cell death (ICD) and elicit antitumor immunity. The resulting carrier denoted as POEG-b-PVBIND, consisting of poly (oligo (ethylene glycol) methacrylate) (POEG) hydrophilic blocks and indoximod conjugated hydrophobic blocks, is rationally designed to improve immunotherapy by synergistically modulating the tumor microenvironment (TME). Our data showed Dox/POEG-b-PVBIND micelles led to significantly improved tumor regression in an orthotopic murine breast cancer model compared to both Dox-loaded POEG-b-PVB micelles (a control inert carrier) and POEG-b-PVBIND micelles alone, confirming the combination effect of indoximod and Dox in improving the overall antitumor activity.

Table of Contents

<i>Title Page</i>	<i>i</i>
<i>Committee Page</i>	<i>ii</i>
<i>Abstract</i>	<i>iv</i>
<i>List of Tables</i>	<i>xvi</i>
<i>List of Figures</i>	<i>xvii</i>
PREFACE	xxii
1.0 INTRODUCTION	1
1.1 CANCER IMMUNOTHERAPIES	1
1.2 T CELL CHECKPOINT INHIBITOR-MEDIATED CANCER IMMUNOTHERAPY IS NOT SUFFICIENT	2
1.3 EXPLORING NOVEL IMMUNOSUPPRESSIVE MECHANISMS	3
1.3.1 An Overview of Neurotransmitters and Immune Response	3
1.3.2 Expression of mGluR4 on Immune Cells	4
1.3.3 mGluR4 and Immune Response in CNS	5
1.3.4 mGluR4 and Cancer	9
1.3.5 mGluR4 as Novel Target for Cancer Immunotherapy	12
1.4 DEVELOPING MULTIFUNCTIONAL MICELLE DELIVERY SYSTEM FOR ENHANCING IMMUNOTHERAPY	12
1.4.1 . Combination of Immunotherapy with Chemotherapy is a Promising Strategy for Breast Cancer	12

1.4.2	IDO Inhibitors are Promising Immune Therapeutics for Breast Cancer.	13
1.4.3	Tryptophan Pathway, IDO enzymes and Their Targets: Indoximod is a Lead and Safe IDO Inhibitor.....	14
1.4.4	The Limitations of Current Formulations of Indoximod.....	16
1.4.5	POEG-Derivatized Indoximod-Based Multi-Functional Polymeric Micelle system for Enhancing Breast Cancer Immunotherapy.....	17
2.0	<i>TARGETING METABOTROPIC GLUTAMATE RECEPTOR 4 FOR CANCER IMMUNOTHERAPY.....</i>	19
2.1	Abstract.....	19
2.2	Introduction.....	20
2.3	Experiment Procedures.....	23
2.3.1	Mice.....	23
2.3.2	Tumor cell lines.....	24
2.3.3	Tumor model.....	24
2.3.4	Analysis of tumor-infiltrating lymphocytes and myeloid-derived suppressor cells.....	25
2.3.5	Mouse NK and CD8 ⁺ T cells isolation and culture.....	26
2.3.6	MTT assay.....	27
2.3.7	Preparation and characterization of MSOP CaP nanoparticles.....	27
2.3.8	Bulk RNA-Seq analysis.....	29
2.3.9	Analysis of cancer patient data.....	30
2.3.10	Single cell sequencing data processing.....	31
2.3.11	Single cell T-cell-receptor data processing.....	32

2.3.12 Re-analysis of single-cell RNA-seq and ATAC-seq data.....	33
2.3.13 Statistical analysis.....	34
2.4 Results.....	38
2.4.1 <i>Grm4</i> ^{-/-} have significantly delayed tumor growth in male mice.....	38
2.4.2 <i>Grm4</i> ^{-/-} mice skewed tumor microenvironment toward an immunogenic phenotype.....	40
2.4.3 GRM4 is expressed in tumor infiltrating immune cells.....	44
2.4.4 <i>Grm4</i> ^{-/-} reshapes the landscape of tumor-infiltrating immune cells and the related signaling.....	48
2.4.5 <i>Grm4</i> ^{-/-} conditions NK, CD4 ⁺ T, CD8 ⁺ T cells toward a highly proliferative and activated phenotype.....	56
2.4.6 <i>Grm4</i> ^{-/-} -mediated tumor regression is dependent on NK and CD8 ⁺ T cells.....	59
2.4.7 <i>Grm4</i> ^{-/-} -triggered immune activation is associated with induction of immune resistance and synergizes with treatment with immune checkpoint inhibitors.....	60
2.4.8 High-throughput scRNA-Seq identifies the reshaped landscape of tumor infiltrating CD8 ⁺ T cells.....	63
2.4.9 ScTCR profiling maps the subset connectivity by pseudotime state and clonal TCRs.....	69
2.4.10 GRM4/cAMP/CREB signaling modulates the function of NK and CD8 ⁺ T cells.....	74

2.4.11 Pharmacological inhibition of GRM4 significantly delays tumor growth	79
2.4.12 MSOP calcium phosphate nanoparticles significantly improve the anti-tumor effect.	86
2.4.13 NK ^{high} -GRM4 ^{low} and CD8 ^{high} -GRM4 ^{low} signatures predict improved patient survival.	92
2.5 Discussion	95
3.0 <i>Dual Functional Immunostimulatory Polymeric Prodrug Carrier with Pendent Indoximod for Enhanced Cancer Immunochemotherapy.</i>	102
3.1 Abstract	102
3.2 Introduction	103
3.3 Materials and Method	108
3.3.1 Materials	108
3.3.2 Cell lines and tumor models	108
3.3.3 Synthesis of Boc-Protected Indoximod	109
3.3.4 Synthesis of POEG-MacroCTA	110
3.3.5 Synthesis of POEG-b-PVB and POEG-b-PVBIND Polymers	110
3.3.6 Micelle Preparation and Characterization	112
3.3.7 Critical Micelle Concentration (CMC) and Storage Stability	113
3.3.8 In Vitro Cytotoxicity of POEG-b-PVBIND micelles	113
3.3.9 In Vitro Drug Release	114
3.3.10 In Vivo Distribution Profile	115

3.3.11 Anti-tumor Efficacy Study.....	116
3.3.12 Quantification of Tumor-Infiltrating Lymphocytes.....	117
3.3.13 Safety Evaluation.....	118
3.3.14 Statistical Analysis.....	118
3.4 Results and Discussion.....	119
3.4.1 Synthesis and Characterization of POEG-b-PVBIND Polymer.....	119
3.4.2 Physicochemical Characterization of POEG-b-PVBIND and Dox-Loaded Micelles.....	125
3.4.3 <i>In Vivo</i> Distribution of POEG-b-PVBIND Micelles.....	129
3.4.4 <i>In Vivo</i> Therapeutic Efficacy.....	133
3.4.5 Antitumor Immune Response <i>in Vivo</i>	137
3.4.6 Safety Evaluations.....	139
3.5 Conclusions.....	142
4.0 <i>Summary and Perspectives</i>	143
<i>Bibliography</i>	149
 <i>PREFACE</i>	 xxii
 1.0 <i>INTRODUCTION</i>	 1
1.1 CANCER IMMUNOTHERAPIES.....	1
1.2 T CELL CHECKPOINT INHIBITOR-MEDIATED CANCER IMMUNOTHERAPY IS NOT SUFFICIENT.....	2
1.3 EXPLORING NOVEL IMMUNOSUPPRESSIVE MECHANISMS.....	3

1.3.1 An Overview of Neurotransmitters and Immune Response.....	3
1.3.2 Expression of mGluR4 on Immune Cells.....	4
1.3.3 mGluR4 and Immune Response in CNS.....	5
1.3.4 mGluR4 and Cancer.....	9
1.3.5 mGluR4 as Novel Target for Cancer Immunotherapy.....	12
1.4 DEVELOPING MULTIFUNCTIONAL MICELLE DELIVERY SYSTEM FOR ENHANCING IMMUNOTHERAPY.....	12
1.4.1 . Combination of Immunotherapy with Chemotherapy is a Promising Strategy for Breast Cancer.....	12
1.4.2 IDO Inhibitors are Promising Immune Therapeutics for Breast Cancer.	13
1.4.3 Tryptophan Pathway, IDO enzymes and Their Targets: Indoximod is a Lead and Safe IDO Inhibitor.....	14
1.4.4 The Limitations of Current Formulations of Indoximod.....	16
1.4.5 POEG-Derivatized Indoximod-Based Multi-Functional Polymeric Micelle system for Enhancing Breast Cancer Immunochemotherapy.....	17
2.0 TARGETING METABOTROPIC GLUTAMATE RECEPTOR 4 FOR CANCER IMMUNOTHERAPY.....	19
2.1 Abstract.....	19
2.2 Introduction.....	20
2.3 Experiment Procedures.....	23
2.3.1 Mice.....	23
2.3.2 Tumor cell lines.....	24

2.3.3 Tumor model.....	24
2.3.4 Analysis of tumor-infiltrating lymphocytes and myeloid-derived suppressor cells.....	25
2.3.5 Mouse NK and CD8 ⁺ T cells isolation and culture.....	26
2.3.6 MTT assay.....	27
2.3.7 Preparation and characterization of MSOP CaP nanoparticles.....	27
2.3.8 Bulk RNA-Seq analysis.....	29
2.3.9 Analysis of cancer patient data.....	30
2.3.10 Single cell sequencing data processing.....	31
2.3.11 Single cell T-cell-receptor data processing.....	32
2.3.12 Re-analysis of single-cell RNA-seq and ATAC-seq data.....	33
2.3.13 Statistical analysis.....	34
2.4 Results.....	38
2.4.1 <i>Grm4</i> ^{-/-} have significantly delayed tumor growth in male mice.....	38
2.4.2 <i>Grm4</i> ^{-/-} mice skewed tumor microenvironment toward an immunogenic phenotype.....	40
2.4.3 GRM4 is expressed in tumor infiltrating immune cells.....	44
2.4.4 <i>Grm4</i> ^{-/-} reshapes the landscape of tumor-infiltrating immune cells and the related signaling.....	48
2.4.5 <i>Grm4</i> ^{-/-} conditions NK, CD4 ⁺ T, CD8 ⁺ T cells toward a highly proliferative and activated phenotype.....	56
2.4.6 <i>Grm4</i> ^{-/-} -mediated tumor regression is dependent on NK and CD8 ⁺ T cells	59

2.4.7 <i>Grm4^{-/-}</i>-triggered immune activation is associated with induction of immune resistance and synergizes with treatment with immune checkpoint inhibitors	60
2.4.8 High-throughput scRNA-Seq identifies the reshaped landscape of tumor infiltrating CD8⁺ T cells	63
2.4.9 ScTCR profiling maps the subset connectivity by pseudotime state and clonal TCRs	69
2.4.10 GRM4/cAMP/CREB signaling modulates the function of NK and CD8⁺ T cells	74
2.4.11 Pharmacological inhibition of GRM4 significantly delays tumor growth	79
2.4.12 MSOP calcium phosphate nanoparticles significantly improve the anti-tumor effect	86
2.4.13 NK^{high}-GRM4^{low} and CD8^{high}-GRM4^{low} signatures predict improved patient survival	92
2.5 Discussion	95
<i>3.0 Dual Functional Immunostimulatory Polymeric Prodrug Carrier with Pendent Indoximod for Enhanced Cancer Immunotherapy</i>	102
3.1 Abstract	102
3.2 Introduction	103
3.3 Materials and Method	108
3.3.1 Materials	108

3.3.2 Cell lines and tumor models.....	108
3.3.3 Synthesis of Boc-Protected Indoximod.....	109
3.3.4 Synthesis of POEG-MacroCTA.....	110
3.3.5 Synthesis of POEG-b-PVB and POEG-b-PVBIND Polymers.....	110
3.3.6 Micelle Preparation and Characterization.....	112
3.3.7 Critical Micelle Concentration (CMC) and Storage Stability.....	113
3.3.8 In Vitro Cytotoxicity of POEG-b-PVBIND micelles.....	113
3.3.9 In Vitro Drug Release.....	114
3.3.10 In Vivo Distribution Profile.....	115
3.3.11 Anti-tumor Efficacy Study.....	116
3.3.12 Quantification of Tumor-Infiltrating Lymphocytes.....	117
3.3.13 Safety Evaluation.....	118
3.3.14 Statistical Analysis.....	118
3.4 Results and Discussion.....	119
3.4.1 Synthesis and Characterization of POEG-b-PVBIND Polymer.....	119
3.4.2 Physicochemical Characterization of POEG-b-PVBIND and Dox-Loaded Micelles.....	125
3.4.3 <i>In Vivo</i> Distribution of POEG-b-PVBIND Micelles.....	129
3.4.4 <i>In Vivo</i> Therapeutic Efficacy.....	133
3.4.5 Antitumor Immune Response <i>in Vivo</i>	137
3.4.6 Safety Evaluations.....	139
3.5 Conclusions.....	142
4.0 Summary and Perspectives.....	143

Bibliography..... 149

List of Tables

Table 1 Primers for Genotyping.....	23
Table 2 Resource Table.....	35
Table 3 GSEA analysis showing the top enriched gene sets that were regulated in Grm4^{-/-} in comparison to WT mice in their tumor samples.....	42
Table 4 GSEA analysis of the top enriched gene sets that were upregulated in CD45⁺ cells from B16 tumor bearing Grm4^{-/-} mice.....	50
Table 5 Biophysical characteristics of anticancer drug-loaded POEG-b-PVBIND micelles	120
Table 6 Biophysical Characterizations of blank and Dox-loaded POEG-b-PVBIND micelles.	126

List of Figures

Figure 1. Chemical structure of PEG (A) and POEG (B).....	18
Figure 2 Gating Strategies for Different Immune Populations (CD45 ⁺ cells, NK cells, CD4 ⁺ T cells, CD8 ⁺ T cells, DCs, macrophages, and monocytes).....	26
Figure 3. Preparation of MSOP-loaded Cap Nanoparticles. (A) Schematic presentation of the preparation of MSOP-loaded Cap nanoparticles (NPs). (B) Illustration of the steps involved in the preparation of MSOP NPs.....	29
Figure 4 Global Loss of <i>Grm4</i> Does Not Significantly Impact Tumor Growth in B16 Tumor Model in Female Mice.....	38
Figure 5 Global Loss of <i>Grm4</i> Led to Delayed Tumor Growth in Multiple Tumor Models Through Modulating Tumor Microenvironment.....	39
Figure 6 Applying Bulk RNA Sequencing to Study Tumor Microenvironment.....	40
Figure 7 GSEA analysis showing the top enriched gene sets that were significantly regulated in <i>Grm4</i> ^{-/-} mice.....	41
Figure 8 Histograms showing the fold changes in the expression levels of genes differentially expressed between B16 tumors obtained from <i>Grm4</i> ^{-/-} and WT mice.....	43
Figure 9 The expression pattern of GRM4.....	45
Figure 10 Expression Profiles of GRM4 in Different Tumor-infiltrating Immune Cells in Multiple Cancers.....	46
Figure 11 The expression pattern of GRM4 in Tumor-infiltrating Immune Cells in Murine Tumors.....	47
Figure 12 Expression of GRM4 in Male and Female Immune Cells.....	47

Figure 13 Global Loss of Grm4 Led to Delayed Tumor Growth in B16 Tumor Models Through Mediating Anti-tumor Immunity.....	49
Figure 14 Global Loss of Grm4 Led to Delayed Tumor Growth in B16 Tumor Models Through Recruiting NK, CD4⁺, and CD8⁺ T Cells.....	51
Figure 15 Global Loss of Grm4 Led to Delayed Tumor Growth in B16 Tumor Models Through Modulating Mononuclear Phagocyte System.....	53
Figure 16 Depletion of <i>Grm4</i> Shaped the Immunogenic Tumor Microenvironment in MC38 Murine Colon Cancer Model.....	54
Figure 17 Depletion of <i>Grm4</i> Demonstrated Less Impact on Tumor Immune Microenvironment in B16 Murine Melanoma Model in Female mice.....	55
Figure 18 Global Loss of Grm4 Led to Delayed Tumor Growth in Multiple Tumor Models Through Conditioning NK, CD4⁺ T, and CD8⁺ T Cells Toward a Highly Proliferative and Activated Phenotype.....	57
Figure 19 Depletion of <i>Grm4</i> Shaped the Spenocytes Microenvironment in B16 Murine Melanoma Model.....	58
Figure 20 <i>Grm4</i>^{-/-}-mediated tumor regression is dependent on NK and CD8⁺ T cells.....	60
Figure 21 <i>Grm4</i> Depletion Induced Adaptive Immune Resistance and Synergized with Immune Checkpoint Inhibitors-based Treatments.....	62
Figure 22 The scheme of the overall study design. Single-cell RNA sequencing was applied to CD8⁺ T cells obtained from B16 tumor tissues, and the output data were used for gene expression analysis and TCR profiling.....	63
Figure 23 High-Throughput Single-Cell RNA-Seq of Tumor-Infiltrating CD8⁺ T Cells Revealed Distinct Transcriptional Signatures between WT and <i>Grm4</i>^{-/-} Mice.....	66

Figure 24	The expression of selected genes across the t-SNE plot. The color keys indicate the gene expression values for exhausted markers and inhibitory receptors.....	68
Figure 25	High-Throughput Single-Cell TCR-Seq of Tumor-Infiltrating CD8⁺ T Cells Revealed Distinct Difference.....	70
Figure 26	The ordering of CD8⁺ T cells along pseudotime in a three-dimensional state-space defined by Monocle 3.....	71
Figure 27	High-Throughput Single-Cell RNA-Seq of Tumor-Infiltrating CD4⁺ T Cells.....	73
Figure 28	The experimental scheme for isolation, <i>in vitro</i> culture, and <i>in vitro</i> stimulation of CD8⁺ T cells, and the subsequent flow cytometry analysis.....	74
Figure 29	The Enhanced Anti-tumor Activity and IFN-γ Production of Stimulated <i>Grm4</i>^{-/-} CD8⁺ T Cells.....	75
Figure 30	NK Cells Contributed to the <i>Grm4</i>^{-/-}-mediated Anti-tumor Effect and Enhanced IFN-γ Production.....	76
Figure 31	GSEA plot of upregulated cAMP signaling pathway in isolated <i>Grm4</i>^{-/-} CD45⁺ cells in comparison to WT.....	77
Figure 32	The Enhanced Anti-tumor Activity and IFN-γ Production of Stimulated <i>Grm4</i>^{-/-} CD8⁺ T Cells Was Correlated with Activation of cAMP-CREB-Immune Pathway.....	78
Figure 33	The Enhanced Anti-tumor Activity of Stimulated <i>Grm4</i>^{-/-} CD8⁺ T Cells Was Correlated with Activation of cAMP-CREB-Immune Pathway.....	79
Figure 34	Pharmacological Inhibition of GRM4 with MSOP Significantly Delayed Tumor Growth.....	80
Figure 35	Pharmacological Inhibition of GRM4 with MSOP Does not Delay Tumor Growth in Female Mice.....	81

Figure 36 MTT Assay of Riluzole (GRM1 antagonist), MSOP, and MAP-4 (GRM4 antagonist) Against Cultured B16, MC38, and 3LL Cancer Cells.....	82
Figure 37 MSOP Mediated Anti-tumor Immunity is Dependent on IFN-γ.....	83
Figure 38 Flow Cytometry Analysis and the Quantification of PD-1⁺ NK, CD4⁺ T, and CD8⁺ T cells, and Treg cells after MSOP treatments.....	84
Figure 39 MSOP Synergize with Immune Checkpoint Inhibitors.....	85
Figure 40 Design and Fabrication of MSOP-loaded Cap Nanoparticles.....	87
Figure 41 Characterization of MSOP Cap NPs.....	87
Figure 42 In Vivo Efficacy of MSOP Cap NPs.....	88
Figure 43 Changes in Body Weights after MSOP-NP Treatments.....	89
Figure 44 Safety Profiles of MSOP-NPs.....	90
Figure 45 <i>In Vitro</i> Cytotoxicity of MSOP and MSOP NPs.....	91
Figure 46 NK (CD8)^{high}-GRM4^{low} Signature is Associated with Improved Patient Survival in Male Melanoma Patients.....	93
Figure 47 NK (CD8)^{high}-GRM4^{low} is Associated with Improved Patient Survival in Male Melanoma Patients.....	94
Figure 48 IND-based polymeric micelles for immuno-chemotherapy.....	107
Figure 49 Calibration for quantification of Dox by fluorescence spectrometry.....	115
Figure 50 Synthesis scheme of POEG-G-IND polymer via RAFT polymerization.....	120
Figure 51 Synthesis of POEG-b-PVBIND polymer via RAFT polymerization and post-modification.....	121
Figure 52 ¹H NMR spectrum of POEG MacroCTA polymer reaction mixture in CDCl₃.....	122
Figure 53 ¹H NMR spectrum of POEG MacroCTA polymer in CDCl₃.....	122

Figure 54	¹H NMR spectrum of (A) POEG-b-PVB, (B) POEG-b-PVBIND-Boc, and (C) POEG-b-PVBIND polymers in DMSO.....	123
Figure 55	¹H NMR Spectrum of Boc-Protected IND.....	124
Figure 56	<i>In vitro</i> biophysical and biological characterizations of IND-based polymeric micelles.....	127
Figure 57	DOX release profiles of DOX-loaded POEG-b-PVBIND micelles.....	128
Figure 58	Release profile of IND from POEG-b-PVBIND in presence of esterase.....	129
Figure 59	Characterization of DiR-loaded POEG-b-PVB micelles.....	130
Figure 60	Tumor accumulation of NPs in a subcutaneous xenograft mouse model (4T1.2).	131
Figure 61	The distribution of Dox fluorescence in tumor tissues.....	132
Figure 62	The evaluation of <i>in vivo</i> antitumor efficiency.....	135
Figure 63	Size distribution of POEG-b-PVB micelles/Dox. (carrier: drug, 20:1, w/w).....	136
Figure 64	Expression of Ki-67 protein in tumor tissues following various treatments.....	136
Figure 65	<i>In vivo</i> antitumor immune response after various treatments.....	139
Figure 66	Safety evaluations.....	141
Figure 67	Summary of GRM4^{-/-} Mediated Anti-tumorImmunity.....	145
Figure 68	Summary of How GRM4^{-/-} Shape CD8⁺ T Landscape.....	146
Figure 69	Overall Summary of Chapter II.....	147

PREFACE

This Ph.D. dissertation is a summary of my research work accomplished in the Center for Pharmacogenetics, Department of Pharmaceutical Sciences, in University of Pittsburgh under the dedicated supervision and kind guidance of my dear advisor, Dr. Song Li. I express my sincere appreciation to those who have contributed to this thesis and supported me during this unforgettable journey.

I feel very fortunate to have met my advisor, Dr. Song Li on this very challenging journey. He has always been very supportive, even before I came to Pitt Pharmacy to join his lab. I appreciate all his contributions of time, resource, money, energy, effort, and ideas to support my research. He is a contagious, passionate, and open-minded scientist, who sets an example of excellence as a mentor, leader, and role model in my life. He taught me that always being curious, collaborative, and encouraged me to step out of my comfort zone. These are all precious characteristics for a scientist. Under his guidance, I obtained the opportunities to be trained as a chemist, formulation scientist, immunologist, and computational biologist. This journey is extremely challenging but it is definitely worthwhile when I look back. All these experiences equipped me with the ability and confidence to learn how to become a unique scientist.

I would also like to extend my gratitude to my thesis committee members Dr. Binfeng Lu, Dr. Da Yang, Dr. Robert Gibbs, and Dr. Christian Fernandez for all their insightful comments from various perspectives and the precious time and efforts they have committed during this process. Their instructions and comments helped broaden my horizon and their enlightening

teaching has provided me with a solid foundation to accomplish my thesis work and will always be of great value for my future career and academic research.

I also would like to express my deep thanks to Dr. Jingjing Sun for her great help in the polymer synthesis as well as many precious collaborative opportunities she provided. I learned a lot of philosophy and wisdom from Jingjing both in science and personal life. Thank Dr. Jiang Li for teaching me the first ever cell culture experiment and continuous sharing of his broad knowledge in medicine. Thank Runzi Sun for sharing his valuable experience in immunology and bring the first insight for single RNA seq analysis to me. Thank Sihan Li for sharing his knowledge in bioinformatics and collaboration opportunity. Thank Pearl Moharil and Bei Zhang for bring me joy and laugh during the tough journey of graduate study. Many thanks to other dear lab members, collaborators, and center members (Dr. Yichao Chen, Dr. Jieni Xu, Dr. Yue Zhang, Zhangyi Luo, Haozhe Huang, Ziqian Zhang, Yuang Chen, Apurva Pardeshi, Dr. Wuyueyang Liu, Dr. Pengfei Ren, Dr. Guolian Ren, Dr. Junjie Zhu, Dr. Pengfei Xu, Junchi Xu, Dr. Yuqian Du, Dr. Lei Liang, Dr. Chaogang Wei, Dr. Yanhua Liu, and Xinran Cai), who inspired and helped me in every step forward.

Many thanks for all of faculties and members in Center for Pharmacogenetics. Special thanks to Dr. Wen Xie, Dr. Xiaochao Ma, Dr. Da Yang and Dr. Christian Fernandez who create such a great environment for us to study and research. Many thanks go to the faculties from School of Pharmacy at the University of Pittsburgh. Special thanks to Dean. Patricia Dowley Kroboth, Dr. Randall B. Smith, Dr. Samuel M. Poloyac, Dr. Barry Gold, Dr. Robert B Gibbs, Dr.

Sean Xie, Dr. Maggie Folan, Lori M. Altenbaugh, Dolly Hornick for their support and help all these years.

Many thanks to Dr. James Conway, who provided me the valuable opportunity to pursue an internship in AstraZeneca. I feel fortunate to have found a mentor with such relevant experience, from a bench scientist to a computational biologist. Thanks for his valuable suggestions, kind help, and encouragement for my future career.

I would also acknowledge my dearest friends and colleagues during my PhD journey: Jing Chen, Dr. Xu Song, Pearl Moharil, Ruohui Zheng, Runzi Sun, Evan Sun, Hua Sun, Yang Xie, Yen Long, Matt Madruga, Jie Lu, Peihao Fan, Beihong Ji who made my time at Pitt wonderful and lively.

Finally, I would especially like to thank my amazing family for their unconditional love, dedication, and support. I want to thank my parents, Tianyun Wan and Wanqun Chen. They provided me the freedom and courage to chase my dream. They taught me to be strong and persistent. Many thanks to all the other Wan family members. They have been a constant motivation for me to achieve my goals and conquer every difficulties ahead of me.

1.0 INTRODUCTION

1.1 CANCER IMMUNOTHERAPIES

Cancer immunotherapies have been designed to stimulate our body's immune system to better recognize and fight cancer [1]. Since bacterial toxins were first reported by William B. Coley for treating sarcoma in patients in 1891, immunotherapies have revolutionized oncology and offer novel treatment strategies for many types of cancers in the past few decades [2, 3]. The immune system is composed of lymphoid tissues and immune cells, and cancer immunotherapies aim to train these anti-tumor immune cells in the tumor microenvironment (TME) for detecting and killing cancerous cells [4-6]. There are several types of immune cells that play essential roles in initiating or enhancing anti-tumor immune response, including effector T cells, regulatory T cells, dendritic cells, natural killer cells, myeloid-derived suppressor cells, and tumor-associated macrophages [3]. There are several strategies for stimulating strong anti-tumor immunity against aberrant cancer cells, such as cytokines, cancer vaccines, antibodies, and immune-stimulating adjuvants. These strategies are working on re-awakening the immunosuppressive immune microenvironment as well as enhancing the existing anti-tumor immunity [7].

1.2 T CELL CHECKPOINT INHIBITOR-MEDIATED CANCER IMMUNOTHERAPY IS NOT SUFFICIENT

Cancer immunotherapy is a very powerful weapon and seeks to boost the body's own "immune system" to fight against cancer[8]. The immunosuppressive TME represents one of the hallmarks of cancer and underlies the basis for immune evasion and acquired immunotherapy-resistance for cancer therapy [9]. Significant progress has been made to identify a variety of targets in the tumor microenvironment that can be manipulated to improve the efficacy of cancer immunotherapies[10-12]. Among these targets, blocking the T cell checkpoints, such as cytotoxic T lymphocyte antigen 4 (CTLA-4) and Programmed Death 1 (PD-1), has shown great clinical success. In particular, the Yevoy[®] and Opdivo[®] that target CTLA-4 and PD-1 demonstrated great success in treating many diverse cancer types [13-16]. However, only a subset of patients respond to such approaches, and currently the low response to T cell checkpoint immunotherapy is one of the most important clinical challenges in cancer treatment.

The reason for non-response is very complicated. **On the one hand, additional immunosuppressive mechanisms exist in the TME** [10-12]. Therefore, a better understanding of the mechanisms that regulate the immunosuppressive TME plays a crucial role for developing more efficacious immunotherapies and combination strategies. **On the other hand,** the use of the free drug raises the issue of water-solubility, rapid blood elimination and metabolism. Improvement in drug bioavailability and/or co-delivery of multiple drugs via a nanocarrier represents a promising strategy to improve the therapeutic outcome and patient compliance.

1.3 EXPLORING NOVEL IMMUNOSUPPRESSIVE MECHANISMS

1.3.1 An Overview of Neurotransmitters and Immune Response

Neurotransmitters (NTs) have recently received increasing appreciation as important immune modulators. The immune cells express receptors for many classes of NTs and the communication between NTs and their receptors establish neuro-immune interactions for regulating effective immune response in both CNS and peripheral tissues [17]. Interestingly, the role of NTs is very complicated and the same NTs can even exert opposing effects for promoting or inhibiting tissue immunity in different contexts [18-22].

Studies of the NTs and their receptors in modulating immunity are limited and therein are important areas of investigations. L-Glutamate (Glu) is the major excitatory neurotransmitter in the mammalian CNS [23]. It acts via two classes of receptors, ligand gated ion channels (ionotropic receptors (iGluRs))-regulating rapid responses upon activation, and G-protein coupled (metabotropic) receptors-modulating signal transduction cascades. Eight different types of mGluRs, mGluR1 to mGluR8 are divided into groups I, II, and III on the basis of their intracellular signal transduction mechanisms, agonist pharmacology, and sequence homologies [24]. Group I includes mGluR1 and mGluR5, coupled to Gq protein; group II includes mGluR2 and mGluR3, coupled to Gi and Go proteins; group III includes mGluR4, mGluR6, mGluR7 and mGluR8, coupled to Gi and Go proteins in heterologous expression systems.

mGluR4 is expressed at high levels in CNS and plays a role in various physiological and pathophysiological processes in CNS [25, 26], such as learning, memory, and cognitive

impairment. In addition, growing evidence indicates that mGluRs are expressed in peripheral tissues such as thymus and lymphocytes [27]. These results suggest a potential role of mGluR4 in immune regulation.

1.3.2 Expression of mGluR4 on Immune Cells

Clinical data indicate that elevated plasma concentrations of Glu are associated with immune deficiency [28, 29]. In addition, in vitro assays show that high concentrations of Glu (>100 uM) can inhibit mitogen-induced T-cell proliferation [28, 29]. Therefore, it is not surprising that immune cells express mGluRs. It has been proposed that mGluRs can mediate an emergency mechanism once high levels of Glu are reached.

Using immunostaining and Western blot analysis, Rezzani et al. observed the expression of mGluR4 in rat thymic cells [30]. The expression of mGluR4 was abundant in dendritic cells (DCs) and lymphocytes of the thymic medulla but was weak in lymphocytes of the cortex. It is interesting to note that a rapid inhibition of mGluR4 expression was induced in the rat thymus after treatment with cyclosporine (an immunosuppressant). mGluR4 expression was undetectable after longer treatment with cyclosporine.

Other evidence also shows that the expression of mGluRs is not exclusive to young immune cells because mature lymphocytes are activated by selective mGluR ligands. In addition, rat peripheral lymphocytes responded by producing reactive oxygen species (ROS) when they were exposed to the group III mGluR agonist L-2-amino-4-phosphonobutyric acid (L-AP4) [31]. ROS play important roles in T-cell biology and participate in activation-induced T cell apoptosis

and hence in the termination of the immune response [32]. Moreover, DCs are capable of secreting glutamate when interacting with T lymphocytes, a process that might be essential for the function of lymphocytes. This hypothesis is based on the fact that the absence of glutamate led to impaired Th1 (Interleukin-2 (IL-2) and interferon- γ) and proinflammatory (IL-6 and tumor necrosis factor-alpha) cytokine production. However, these changes were not correlated with a decrease in T-cell proliferation.

1.3.3 mGluR4 and Immune Response in CNS

A role for mGluR4 in immune modulation was first described in an autoimmune disease model [33]. Fallarino et al. reported that mGlu4 knockout mice ($Grm4^{-/-}$) were highly susceptible to experimental autoimmune encephalomyelitis (EAE), a model of multiple sclerosis. More specifically, $Grm4^{-/-}$ mice and their wild-type (WT) counterparts were immunized with myelin oligodendrocyte glycoprotein (MOG35–55), which can induce EAE in C57BL/6 mice. The EAE clinical scores were recorded periodically and a lack of mGluR4 was found to be associated with earlier onset, more severe, and ultimately fatal EAE in >40% of the hosts. Along with these changes, white matter demyelination and inflammatory infiltrates were more prevalent in the spinal cord of MOG-vaccinated $Grm4^{-/-}$ mice in comparison to their WT counterparts, according to the morphological changes. The phenotype has also been characterized in littermates as well (heterozygote breeding—with cohorts of mice being matched for gender and age) and the disease indications were also more severe in $Grm4^{-/-}$ and $Grm4^{+/-}$ mice than in WT mice. In contrast, treatment of N-Phenyl-7-(hydroxyimino) cyclopropa [b] chromen-1a-carboxamide (PHCCC), a $Grm4$ -positive allosteric modulator, led to increased resistance to EAE.

This was in agreement with previous reports demonstrating that long-term treatment of L-AP4 can increase the recovery rate from EAE in Lewis rats [33, 34].

There was significant infiltration of CD4⁺ T cells, CD8⁺ T cells and B220⁺ B cells in both peripheral lymphoid organs and the CNS in both Grm4^{-/-} and WT mice, but the percentages of CD4⁺ and CD8⁺ T cells as well as CD11b⁺ and CD11c⁺ cells were significantly higher in the CNS of Grm4^{-/-} mice at the peak of disease [33]. Extended studies using littermates from heterozygote breeding further showed that the disease course was more severe in Grm4^{-/-} and Grm4^{+/-} mice than in WT mice. The cytokine profiling of sorted CD4⁺ T cells from brain-infiltrating leukocytes (BILs) and pooled lymph nodes demonstrated a significant increase in *Rorc* transcripts (encoding the T_H17 specification factor), a reduction in *Foxp3* (Treg) transcripts, and no change in *Tbx21* (coding for Tbet; a T_H1 maker) in Grm4^{-/-} mice during the neurologic signs. No changes were observed in *Gata3* (a T_H2 marker) in both groups. These data suggested that Grm4^{-/-} tipped the balance of transcriptional activation in favor of inflammatory genes in response to MOG vaccination. In particular, Grm4^{-/-} favored the emergence of T_H17 over Treg cells, which would sustain inflammation and exacerbate EAE [34].

Expression of mGluR4 was confirmed in several immune subpopulations, such as CD4⁺ T cells, CD8⁺ T cells, $\gamma\delta$ T cells, B220⁺ B cells, CD11b⁺ and CD11c⁺ cells, particularly in CD4⁺ T and CD11c⁺ cells, suggesting those cells as potential targets for Grm4 mediated effects. The expression of mGluR4 was also confirmed in DC subsets in splenocytes, including conventional DCs (cDCs; CD11b⁺CD11c^{high}) and plasmacytoid DCs (pDCs; mPDCA1⁺ CD11c^{low}). They have further shown that treatment with toll-like receptor ligands such as lipopolysaccharide (LPS) and

CpG-oligonucleotide (CpG-ODN) led to increased Grm4 expression. Modulation of mGluR4 expression in activated nTreg cells (CD4⁺ CD25⁺) and LPS-stimulated cDCs was also confirmed, further supporting that mGluR4 activation within an immunologic synapse contributes to the crosstalk and reciprocal influence between T and accessory cells [33].

IL-17-producing T helper (Th17) cells are considered mediators of autoimmunity in multiple sclerosis and EAE. The accumulation of Th17 cells in the CNS as well as in the periphery is also associated with the development of demyelinating plaques of multiple sclerosis [35]. Fallarino et al also pointed out that the absence of mGlu4 in dendritic cells is key to inducing a differentiation of T helper cells toward the Th17 phenotype. More specifically, possible regulatory function of mGluR4 in the interaction between CD4⁺ T cells and DCs has been examined. Both cDCs and pDCs from Grm4^{-/-} mice produced higher amounts of IL-6 and IL-23, but less IL-12 and IL-27, compared to their WT counterparts in response to LPS or CpG-ODN, respectively [33].

The notable results of co-culturing WT CD4⁺ T cell and Grm4^{-/-} DCs demonstrated an increase of IL-17A⁺ CD4⁺ T cells, along with a significant reduction in IFN- γ producing CD4⁺ T cells (a portion of which also expressed IL-17A). However, they failed to see this effect when the co-culture consisted of WT DCs and Grm4^{-/-} T cells, suggesting that the effect of mGluR4 depletion was largely dependent on DCs in this *in vitro* system. The cytokine production in culture supernatants has been examined and there are decreased amounts of TH1-associated IL-2 in co-culture system involving Grm4^{-/-} cDCs. IL-27 is known to counter the effect of IL-6 in directing TH17 cell development, which can limit the EAE progression. The decrease in IL-27

during activation of naïve CD4⁺ T cells might be another reason for favoring the emergence of Th17 cells [33].

They also suggest that activation of mGlu4 (as a result of elevated levels of glutamate during the neuroinflammation) might exert a protective effect by preventing an unbalance in T helper cells. Such mechanism presents a clear therapeutic potential for treating autoimmune-related disorders.

The underlying mechanism for Grm4-mediated immune regulation is not clear at present. However, there appears to be a cross-talk and reciprocal influences between Grm4 and indoleamine 2,3-dioxygenase 1 (IDO-1) pathways [36]. IDO1 is well known to be involved in generating an immunosuppressive environment through catalyzing the metabolism of tryptophan, resulting in tryptophan depletion and accumulation of kynurenine [37]. A protective role of IDO-1 has been shown in mice with different forms of EAE including acute, relapsing-remitting, and adoptively transferred disease [38]. Interestingly, in addition to the direct immunosuppressive effect of kynurenine through inhibition of CD8⁺ T cells and activation of Treg cells, kynurenine metabolites such as cinnabarinic acid (CA) act as selective, although weak, orthosteric agonists of mGluR4 [39]. The therapeutic effect of CA in acute EAE was reduced in Grm4^{-/-} mice [40]. On the other hand, activation of Grm4 could positively impact the IDO1 pathway. Treatment of DCs with ADX88178, a positive allosteric modulator (PAM) of Grm4, led to both increased expression levels of IDO-1 and phosphorylation of IDO-1 [36]. These effects require a Gi-independent, alternative signaling pathway that involves phosphatidylinositol-3-kinase (PI3K), Src kinase, and the signaling activity of IDO1. Moreover, the effect of ADX88178 on the

expression of several cytokines was impaired in IDO1^{-/-} DCs [36]. Therefore, Grm4 and IDO1 constitute a loop that provides a positive feedback mechanism to amplify the immune-protective effect in EAE and possibly other immune-related diseases [36].

1.3.4 mGluR4 and Cancer

Most studies on the role of glutamate receptor in cancers have been focused on iGluRs [41, 42]. Tumor cells originated from neuronal tissues express iGluR subunits and iGluR antagonists have shown inhibitory effects on the proliferation of the tumor cells. Similarly, iGluR subunits have been shown to be expressed in several peripheral cancers, and blockade of the N-methyl-D-aspartate (NMDA) and α -amino-3-hydroxy-5-methyl-4-isoxazolepropionic acid (AMPA) ionotropic glutamate receptor subtypes leads to decreased cell proliferation and migration [42].

mGluRs are also expressed in several cell lines derived from human tumors, including neuroblastoma, thyroid carcinoma, rhabdomyosarcoma/medulloblastoma, lung carcinoma, multiple myeloma, glioma, colon adenocarcinoma, astrocytoma, T cell leukemia, and breast carcinoma [43]. In particular, mGluR1 has been shown to be expressed in subsets of human melanomas [44]. Ectopic expression of mGluR1 in melanocytes drives the development of melanoma in mouse models. Pharmacological inhibition of mGluR1 led to inhibition of tumor cell growth both in vitro and in vivo. Riluzole, an antagonist of mGluR1 signaling has advanced to phase II clinical trials in patients with advanced melanoma [45, 46].

The studies on the roles of mGluR4 in cancers are very limited and controversial. Change et al. studied the expression pattern of mGluR4 in several healthy and diseases-derived human tissues [47]. mGluR4 receptor expression was identified in 68% of colorectal carcinomas, 50% of laryngeal carcinoma, and 46% of breast carcinomas. In the case of colorectal carcinoma, overexpression of mGluR4 was correlated with poor prognosis, and cell lines derived from human colorectal carcinomas showed increased cell invasiveness when treated with L-AP4. In another study, comparative proteomics was used to characterize a human colon cancer cell line that was resistant to 5-fluorouracil (5-FU, a common chemotherapy agent). Interestingly, 5-FU resistant cells were found to overexpress mGluR4 in comparison with parental cancer cells. It has been demonstrated that cell survival was increased by the group III mGlu receptor agonist L-AP4 in the non-resistant parent cancer cells; conversely, survival was synergically decreased by 5-FU and the group III receptor antagonist MAP4 in 5-FU-resistant cells. It is noteworthy to mention that 5-FU downregulated mGluR4 expression, and MAP4 has a dose dependent cytotoxic effect in both cell lines [48].

In contrast to the above reports, mGluR4 agonists are shown to inhibit the proliferation of human breast and bladder cancer cells in a GRM4-dependent manner [49]. In the study by Lasek et al., the expression of mGlu4 was shown to be inversely correlated with the severity of human medulloblastoma [50]. After scoring the extent of immunoreactivity for mGlu4 in human biopsies of medulloblastoma, the absence of spinal metastases, cerebrospinal fluid spread, and tumor recurrence as well as the survival of patients were all shown to be associated with high levels of mGlu4 immunoreactivity. Treatment with PHCCC (which is considered a group I mGlu receptor antagonist but can also act as a positive allosteric modulator of mGlu4 receptor) reduced

the proliferation of cultured medulloblastoma cells and inhibited the growth of medulloblastoma implants in mice. In addition, subcutaneous or intracranial injections of PHCCC during the first week of life reduced the incidence of medulloblastoma from 85 to 28% in a mutant mouse model known to develop the disease upon X-ray irradiation. This indicates that activation of mGlu4 receptors also affects early events in tumorigenesis [51].

The above studies focus on the role of tumor cell-derived Grm4. It has been reported that the plasma levels of Glu are generally elevated in patients with carcinoma and seem to correlate with an impairment in immune function [52]. However, the role of immune cell-derived mGluR including mGluR4 has hardly been studied. Kansara et al. reported that Grm4^{-/-} mice showed accelerated radiation-induced tumor development in an irradiation-induced osteosarcoma model [53]. Outside the CNS, mGluR4 is highly expressed by DCs, as well as CD4⁺ T cells [33]. In the mouse osteosarcomas, they found that mGluR4 is predominantly expressed by CD45⁺CD11c⁺MHC⁺ myeloid cells within the TME instead of tumor cells. Few CD4⁺ T cells were detectable to characterize mGluR4 expression. In consistent with the study by Fallarino et al. in an EAE model, Grm4^{-/-} DCs isolated from the tumors showed increased expression of IL-23. Interestingly, high expression of IL-23 has been observed in primary osteosarcomas and allografted cell lines relative to normal bone, while ex-vivo cultured osteosarcoma cell lines and primary tumor cells did not express IL23. A role of IL-23 in tumorigenesis has been well established from previous studies [54]. Indeed, IL23^{-/-} mice were resistant to the irradiation-induced osteosarcoma. They hypothesized that knockout of Grm4 in DCs facilitates the oncogenesis of osteosarcoma through increased production of IL-23 [53].

1.3.5 mGluR4 as Novel Target for Cancer Immunotherapy

Our studies demonstrated that targeting GRM4 could be exploited as a new approach for cancer immunotherapy. We have shown in three murine syngeneic tumor models (B16, MC38, and 3LL) that either genetic knockout ($Grm4^{-/-}$) or pharmacological inhibition led to significant delay in tumor growth. Mechanistically, perturbation of GRM4 resulted in a strong anti-tumor immunity by promoting natural killer (NK), $CD4^{+}$ and $CD8^{+}$ T cells towards an activated, proliferative, and functional phenotype. We have further shown that the antitumor activity of $Grm4$ antagonists can be further improved through combination with anti-PD-1 antibody. Gender differences also have been reported in this study. Overall, we provided a new avenue for enhancing cancer immunotherapies.

1.4 DEVELOPING MULTIFUNCTIONAL MICELLE DELIVERY SYSTEM FOR ENHANCING IMMUNOTHERAPY

1.4.1 . Combination of Immunotherapy with Chemotherapy is a Promising Strategy for Breast Cancer

The idea of combining conventional chemotherapeutic agents with immunotherapies has been regarded as a very promising therapeutic approach for cancer treatment [55]. This is supported by promising data from clinical trials [56]. The mechanism behind this successful combination may be due to the enhanced immune response of conventional anticancer drugs in addition to their direct killing effects on tumor cells. As reported, certain anticancer drugs

including Dox, can induce a protective immune response, which might help to enhance the overall antitumor efficacy [57]. However, the effectiveness of the chemotherapeutics-induced immune response is limited by feedback suppressive circuits activated during tumor development and cancer treatment [58]. These feedback suppression circuits were reported to induce suppressive immune microenvironment such as upregulation of inhibitory T-cell pathways (especially programmed death ligand 1/programmed death 1 (PD-L1/PD-1)), regulatory immune cells, and metabolic enzymes such as indoleamine-2,3-dioxygenase (IDO) [59].

1.4.2 IDO Inhibitors are Promising Immune Therapeutics for Breast Cancer

Based on the findings discussed above, a blockade of inducible negative feedback mechanisms represents one of the most promising approaches to enhance the immune response for cancer treatment. Indeed, exciting results have been obtained from preclinical and clinical trials with the use of the CTLA-4 and PD-1 pathway inhibitors, known as Ipilimumab (Yevoy®) and Nivolumab (Opdivo®) [13, 14]. The aforementioned CTLA-4 and PD-1 are two important inhibitory proteins involved in immune checkpoint pathways and their expression is upregulated on activated T cells. As researchers continue to explore immune checkpoints as targets for anti-cancer therapies, the IDO pathway has emerged as the leading contender to yield the next batch of new drugs for boosting immune response. Based on recent clinical evidence, the IDO protein or IDO enzyme, plays an important role in generating an immunosuppressive microenvironment [58]. Interestingly, IDO enzyme is also reported to interact both with CTLA-4 and PD-1 checkpoints via complex loops that are not clearly elucidated[58, 60]. Based on the existing evidence, the expression of CTLA-4 on regulatory T (Treg) cells leads to upregulation of IDO

enzymes on dendritic cells (DCs), while the upregulated IDO enzymes increase the expression of PD-1 on Treg cells. Therefore, the pharmacological inhibition of IDO enzymatic activity represents a promising approach to enhance immune response. For these reasons, numerous IDO inhibitors have been developed for increasing therapeutic efficacy of cancer treatment.

1.4.3 Tryptophan Pathway, IDO enzymes and Their Targets: Indoximod is a Lead and Safe IDO Inhibitor

Tryptophan is an essential amino acid with a typical indole ring in its structure, which can be metabolized to kynurenine by three distinctive IDO enzymes, including indoleamine 2,3-dioxygenase 1 (IDO1), indoleamine 2,3-dioxygenase 2 (IDO2), and tryptophan 2,3-dioxygenase (TDO). Indeed, as demonstrated in pre-clinical models starting over a decade ago, inhibiting the IDO1 enzyme can empower the efficacy of cytotoxic chemotherapy without increasing their side effects [61-64]. The IDO1 enzyme is activated in many human cancers in tumor, stromal, and innate immune cells where its expression tends to be associated with poor prognosis. Its role in immunosuppression is multifaceted, involving the suppression of CD8⁺ T effector cells and natural killer (NK) cells as well as increased activity of CD4⁺ T regulatory cells (Tregs) and myeloid-derived suppressor cells (MDSC). The increased kynurenine metabolites by activation of IDO1 can also bias differentiation of macrophages toward tumor associated macrophages (TAMs), an immunosuppressive phenotype. The increased infiltration of MDSCs, Tregs and TAMs is an important clinical indicator for poor patient prognosis and possible resistance to therapies. Therefore, IDO1 targeting is a promising strategy for reversing immune-suppressive environment and there are preclinical proofs that IDO1 inhibitors can safely empower the efficacy of cytotoxic or targeted chemotherapy. Furthermore, there is emerging interest in two

other tryptophan catabolic enzymes, TDO and IDO2, which also appear to influence inflammatory programs, with ongoing exploration of IDO1 inhibitors that also block TDO and IDO2 to deepen efficacy, limit inherent or acquired resistance to IDO1 blockade, and reduce autoimmune side effects of immune therapy.

1-methyl-D, L-tryptophan (1-D, L-MT), a racemic mixture of two stereoisomers (1-D-MT, 1-L-MT), is one of the first well-studied IDO inhibitors. There has been a long-standing debate as to which stereoisomer is superior for cancer immunotherapy. Interestingly, the L counterpart of 1-MT has a higher potency in cell-based assays, while its D counterpart has proved to be more effective regarding immunostimulatory effects in vivo. Hence, 1-methyl-D-tryptophan (indoximod) is selected as the potential candidate in clinical trials as an adjunct approach to conventional chemotherapy [65]. Indoximod was first identified as an IDO1-specific enzymatic inhibitor. One puzzling issue has been the fact that this compound does not exhibit significant inhibition of the IDO1 enzyme in vitro, but closely mimics the biological consequence of IDO1 enzymatic inhibition in vivo. A later study demonstrated that Indoximod has no inhibitory effect on IDO1 enzyme activity. A number of studies have addressed the MOA of Indoximod, including indirectly inhibition of the IDO2 isoform [66-69]. In addition, Indoximod acts as a high-potency tryptophan mimetic in reversing mTORC1 inhibition and the accompanying autophagy that is induced by tryptophan depletion in cells. As a central integrator of cell growth signals, mTORC1 receives signals that monitor levels of essential amino acids needed to activate cell growth, including in T cells. Interestingly, Indoximod was able to relieve mTORC1 suppression created by tryptophan deprivation with a higher potency than tryptophan itself [70].

Learning more about the distinct mechanism of action of Indoximod may yield significant insights. As it relieves a common downstream IDO/TDO effector signal in mTORC1, Indoximod is rationalized to attack tumors that overexpress any tryptophan catabolizing enzyme. Furthermore, its narrower MOA opens the possibility that relieving mTORC1 blockade in T cells is sufficient for anticancer efficacy by an IDO/TDO enzyme inhibitor, meaning that inhibiting all IDO/TDO function is unnecessary and may even heighten side effects. This hypothesis is based on the clinical evidence [71, 72] that Phase I studies of Indoximod suggest it is well tolerated: in a dose escalation study of 22 evaluable advanced cancer patients receiving taxotere, the co-administration of Indoximod was found to be well tolerated to the maximum delivered dose of 1,200 mg twice daily. Further studies of the connections between tryptophan catabolism and mTORC1 control may yield an important new crop of useful immunoregulatory principles. In developing the intriguing research direction opened by Indoximod, a prodrug form termed NLG-802 with superior pharmacokinetics has been reported and has entered phase I testing [73].

1.4.4 The Limitations of Current Formulations of Indoximod

Different formulations of Indoximod have been investigated such as salts, spray dry dispersion and a series of prodrugs with different salt forms [74]. Nevertheless, the results of these studies showed that only a few selected prodrugs can result in improved solubility and increased in vivo exposure upon oral administration. In addition, there are other issues that negatively affect the therapeutic efficacy such as limited absorption and fast blood clearance of small molecules, which necessitates the use of frequent dosing. These limitations have prompted

us to develop an intravenous strategy for improving the formulation bioavailability of Indoximod at tumor tissues.

1.4.5 POEG-Derivatized Indoximod-Based Multi-Functional Polymeric Micelle system for Enhancing Breast Cancer Immunotherapy

The free base form of 1-D-MT is barely soluble in aqueous solutions. One common strategy to enhance the solubility of hydrophobic drugs is to solubilize them in organic solvents at first and then dilute this stock solution with aqueous buffers. However, the solubility of 1-D-MT in these organic solvents is limited as well, such as tetrahydrofuran (THF), dimethyl sulfoxide (DMSO), and methanol and dimethylformamide (DMF). It is difficult to load 1-D-MT into a micelle carrier due to the limited solubility of 1-D-MT in both volatile solvents and aqueous solvents [60]. In order to address this issue, 1-D-MT can be conjugated with PEG to generate a “PEGylated polymeric prodrug” to enhance its solubility in aqueous solutions. An additional advantage is that the PEG modification can prevent the rapid elimination of these small molecules and prolong their circulation time in the body due to the following mechanisms: 1) PEG has shielding effects by masking the 1-D-MT agent from recognition by the host immune system (reduced antigenicity and immunogenicity), 2) with the modification of PEG, the overall hydrodynamic size of the 1-D-MT-PEG micelle is increased, which helps to reduce renal clearance of the drug, 3) PEG modification can prevent the interaction of amine groups with plasma proteins through the PEG outer shell. Unlike linear PEG, poly (oligo (ethylene glycol) methacrylate) (POEG) is a hydrophilic block chain, which can be polymerized into a polymeric backbone in a tunable manner. POEG provides benefits similar to the benefits of PEG summarized above (Figure 1).

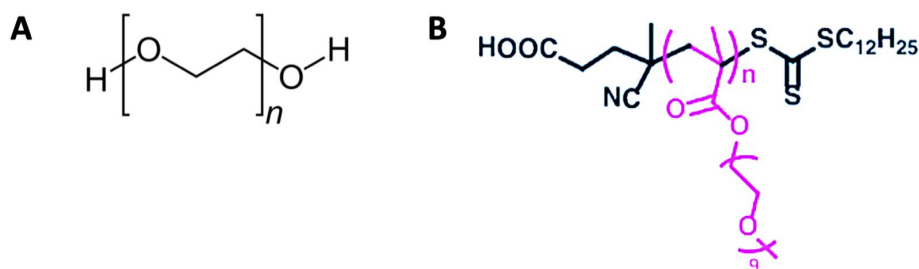


Figure 1. Chemical structure of PEG (A) and POEG (B).

As mentioned, the proposed strategy is to administer 1-D-MT in combination with other traditional chemotherapeutic agents. We hypothesize that our polymeric micellar carrier that is based on a prodrug of 1-D-MT can simultaneously deliver the 1-D-MT agent and another conventional therapy such as Dox into the tumor sites to achieve a synergistic effect. Dox is one of the most effective chemotherapeutics in clinical application for breast cancer treatment. We have recently shown that delivery of paclitaxel (PTX) using the PEG_{2k}-Fmoc-NLG nanocarrier, a PEG-derivatized prodrug of NLG919, leads to significantly improved tumor immune microenvironment and enhanced antitumor response. NLG919 is an IDO1 inhibitor. In this new study we will examine the therapeutic potential of a new nanocarrier that is based on a prodrug of Indoximod. Unlike NLG919, Indoximod has been reported to enhance antitumor immunity via a different MOA. In this proposal, the nanocarrier will be developed via reversible addition fragmentation transfer (RAFT) polymerization. In addition to the simplicity of the synthesis of the nanocarrier, the amount of Indoximod that can be incorporated into the polymer can be readily tuned via controlling the degree of polymerization. Then we will test the functionality of this carrier.

2.0 TARGETING METABOTROPIC GLUTAMATE RECEPTOR 4 FOR CANCER IMMUNOTHERAPY

2.1 Abstract

The complex mechanism regulating the immunosuppressive tumor microenvironment (TME) remains poorly understood. Here, we reported a novel role of the metabotropic glutamate receptor-4 (GRM4) in suppressing the anti-tumor immunity. We revealed in three murine syngeneic tumor models (B16, MC38, and 3LL) that either genetic knockout (*Grm4*^{-/-}) or pharmacological inhibition led to significant delay in tumor growth and synergized with immune checkpoint inhibitors in male mice. Mechanistically, perturbation of GRM4 resulted in a strong anti-tumor immunity by promoting nature killer (NK), CD4⁺ and CD8⁺ T cells towards an activated, proliferative, and functional phenotype. Single-cell RNA-sequencing and T Cell Receptor (TCR) profiling further defined the clonal expansion and immune landscape changes in CD8⁺ T cells. Mechanistically, *Grm4*^{-/-} intrinsically activated IFN- γ production in CD8⁺ T cells through cAMP/CREB-mediated pathway. Our study appears to be of clinical significance as a signature of NK^{high}-GRM4^{low} and CD8^{high}-GRM4^{low} correlated with improved survival in melanoma patients. Therefore, targeting GRM4 could be exploited as a new approach for cancer immunotherapy.

2.2 Introduction

The immunosuppressive tumor microenvironment (TME) represents one of the hallmarks of cancer and underlies the basis for immune evasion and acquired immunotherapy-resistance for cancer therapy [9]. Significant clinical success has been made in cancer treatment through blocking the T cell checkpoints, such as cytotoxic T lymphocyte antigen 4 (CTLA-4) and Programmed Death 1 (PD-1). However, only a subset of patients respond to such approaches, indicating that additional immunosuppressive mechanisms exist in the TME [10-12]. Therefore, a better understanding of the mechanism that regulates the immunosuppressive TME plays a crucial role for developing more efficacious immunotherapies and combination strategies.

Neurotransmitters (NTs) have recently received increasing appreciation as important immune modulators [18, 19]. The immune cells express receptors for many classes of NTs and the communication between NTs and their receptors establishes neuro-immune interactions for regulating effective immune response in both CNS and peripheral tissues. Interestingly, the role of NTs is complicated and the same NTs can exert opposing effects on immunity in different contexts [17]. The studies of the NTs and their receptors in modulating immunity are limited and therein are important areas of investigations. L-Glutamate (Glu) is a major excitatory neurotransmitter in the mammalian CNS. It acts via two classes of receptors, ligand gated ion channels (ionotropic receptors) and G-protein coupled (metabotropic) receptors (mGluRs) [23]. Eight different types of mGluRs, mGluR1 to mGluR8 (GRM1 to 8) are divided into group I, II, and III. Group I include mGluR1 and mGluR5, which are coupled with Gq protein; group II includes mGluR2 and mGluR3, which are coupled with Gi and Go proteins; group III includes

mGluR4, mGluR6, mGluR7 and mGluR8, which are also coupled with Gi and Go proteins in heterologous expression systems.

GRM4 is expressed at high levels in CNS and plays a role in various physiological and pathophysiological processes in CNS such as learning, memory, and cognitive impairment. The expression of GRM4 in a variety of immune cells has also been reported in previous studies [23, 33, 53]. The role of GRM4 in regulating autoimmune disorders in CNS was first reported by Fallarino and colleagues. Mice lacking *Grm4* were shown to be highly susceptible to experimental autoimmune encephalomyelitis (EAE, a mouse model of multiple sclerosis). It appears that knockout of *Grm4* in DCs drives the activation and polarization of naïve CD4⁺ T cells into interleukin-17-producing T helper (Th17) cells, which leads to the EAE progression [33].

The studies on the roles of GRM4 in cancers are very limited and controversial. While the expression of GRM4 is associated with poor prognosis in several types of cancers (malignant gliomas, colorectal cancer, and rhabdomyosarcoma) [47] and drug resistance in colon cancer [48], GRM4 agonists are shown to inhibit the proliferation of cultured cancer cells of non-CNS origin including bladder cancer cells [49] and breast cancer cells [75]. A role of GRM4 in myeloid cells in regulating tumorigenesis was recently reported by Kansara et al: genetic knockout of *Grm4* promoted the initiation and progression of irradiation-induced osteosarcoma through increased production of IL-23 [53].

We report herewith that either genetic knockout (*Grm4*^{-/-}) or pharmacological inhibition of GRM4 led to significant delay of tumor growth in male mice in three syngeneic tumor models

(B16, MC38, and 3LL) through activating anti-tumor immunity. To unravel the complex Grm4 depletion-mediated changes in the immune system, changes in the phenotypic landscape of tumor infiltrating immune populations were characterized by flow cytometry, followed by single-cell RNA-sequencing (scRNA-Seq) and T cell receptor (TCR) sequencing profiling. The effect of Grm4 deficiency on naive immune cells and the underlying mechanism were also studied. We further explored the therapeutic potential of GRM4 inhibitor, alone or in combination with anti-PD-1 or anti-CTLA-4 antibody. Our study suggests that GRM4 is a negative regulator of anti-tumor immunity and targeting of GRM4 may represent a novel strategy to improve cancer immunotherapy.

2.3 Experiment Procedures

2.3.1 Mice

Heterozygous $Grm4^{+/-}$ mice, on a C57/BL6 background, were purchased from Jackson Laboratory. Mice were bred and maintained at the animal facility of University of Pittsburgh, under specific pathogen-free conditions in accordance with all standards of animal care. Littermates ($Grm4^{+/+}$ or $Grm4^{-/-}$) were from $Grm4^{+/-}/Grm4^{+/-}$ breeding offspring; $Grm4^{+/+}$ mice were referred to as WT controls and $Grm4^{-/-}$ as $Grm4$ knockout (KO). All mice used in these studies were genotyped by PCR of DNA isolated from tail clippings (**Table 1**). $Ifng^{-/-}$ mice and WT C57/BL6 mice were purchased from Jackson Laboratory. Experiments were conducted with age- (6-12 weeks old) and gender-matched mice (male and female). All experiments were approved by the Institutional Animal Care and Use Committees of SJCRH and University of Pittsburgh.

Table 1 Primers for Genotyping

Target genes	Gene-specific primer sequences
<i>Grm4</i> KO primers	5' GGTGGATGTGGAATGTGTGCG 3' 5' ATGCAGAGGTGTCTCATACCTG 3' 5' GCCTGGGCTACTGTCTGTCAT 3'

2.3.2 Tumor cell lines

The mouse B16 melanoma cells, 3LL Lewis lung carcinoma cells, and MC38 colon adenocarcinoma cells were purchased from ATCC. B16 cells were cultured in RPMI1640 supplemented with 10% FBS and 100 U/mL penicillin/streptomycin. MC38 and 3LL cells were cultured in Dulbecco's modified Eagle's medium (DMEM) supplemented with 10% FBS and 100 U/mL penicillin/streptomycin. The cells were all cultured in the humidified incubator at 37 °C and 5% CO₂.

2.3.3 Tumor model

B16, MC38 and 3LL tumor cells were subcutaneously injected into C57/BL6, Grm4^{+/+} or Grm4^{-/-} mice, respectively, and the sizes of tumor were monitored every 2~3 days. Tumor volume was calculated by the following formula: tumor volume = 0.5 x length x width². To study the contribution of NK and CD8⁺ T cells to the antitumor effect, five mice in each group were i.p. injected with 200 µg anti-CD8a (Clone: 2.43) (BioXCell), or anti-mouse NK1.1 (Clone: PK136) (BioXCell) antibody or rat IgG2a isotype control (Clone: 2A3) (BioXCell) four times before and after tumor inoculation (day -2, 1, 7, 14). To test the therapeutic effect of combinational blockade of GRM4 and either PD-1 or CTLA-4, control antibody, anti-PD-1 (clone RMP1-14, BioXCell) or anti-CTLA-4 (clone 9D9, BioXCell) was administered at 200 µg per dose via i.p.. MSOP was i.v. injected at a dosage of 10 mg/kg for either single or combination therapy.

2.3.4 Analysis of tumor-infiltrating lymphocytes and myeloid-derived suppressor cells

Flow cytometry experiments were all performed with the instrument LSRII (BD) Aurora (Cytek Biosciences) and analyzed by Flowjo (BD) (Figure 2). Single-cell suspensions were prepared from mouse spleens or tumors as previously described [76]. Briefly, tumors were dissected and transferred into RPMI medium. Tumors were disrupted mechanically using scissors, digested with a mixture of 0.3 mg/mL DNase I (Sigma-Aldrich) and 0.25 mg/mL TL Liberase (Roche) in serum-free RPMI medium for 30 min, and dispersed through a 70- μ m cell strainer (BD Biosciences).

After red blood cell lysis, live/dead cell discrimination was performed using Ghost Dye™ Violet 510 (Tonbo Biosciences) or Zombie Aqua Fixable Viability Kit (BioLegend). Surface staining was performed at 4°C for 30 minutes in FACS staining buffer (1 x PBS / 5% FBS / 0.5% sodium azide) containing designated antibody cocktails. For transcription factor (Ki67) and intracellular proteins staining, cells were fixed and permeabilized using Foxp3 Transcription Factor Buffer Set (eBioscience), following the manufacturer's instructions. For intracellular cytokine staining, cells were stimulated with PMA (100 ng/mL) and Ionomycin (500 ng/mL) for 5 hours in the presence of Monensin. Cells were fixed/permeabilized using the BD Cytotfix/Cytoperm kit prior to cell staining. More detailed information can be found in the **Table 2**.

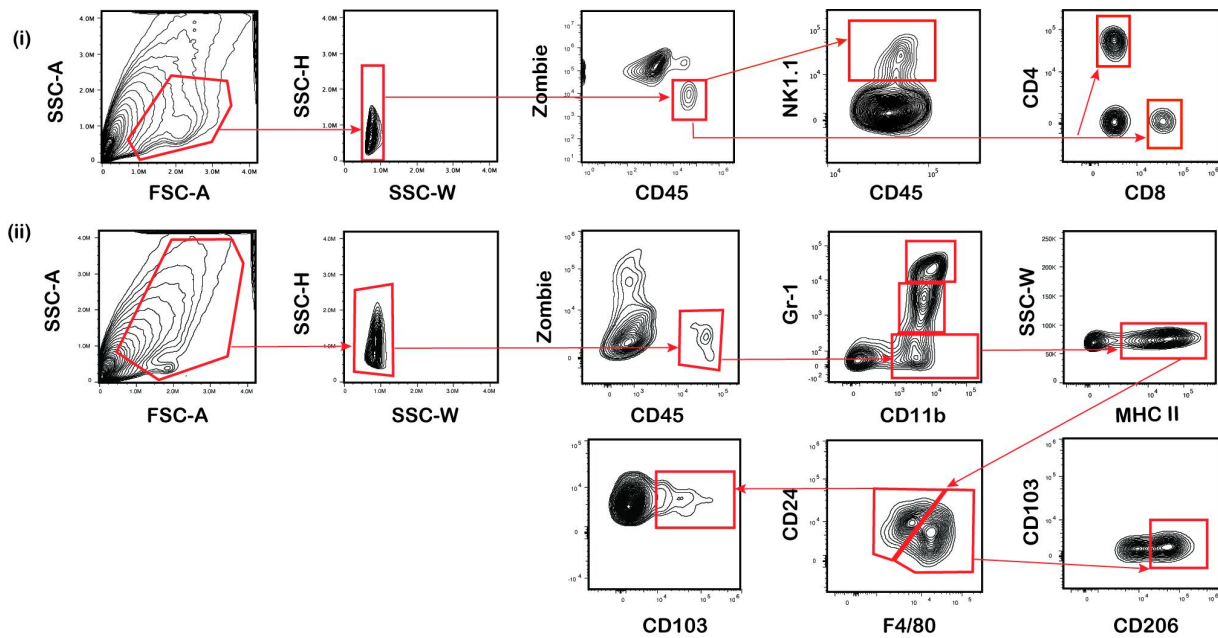


Figure 2 Gating Strategies for Different Immune Populations (CD45⁺ cells, NK cells, CD4⁺ T cells, CD8⁺ T cells, DCs, macrophages, and monocytes).

2.3.5 Mouse NK and CD8⁺ T cells isolation and culture

NK cells were isolated by negative selection from WT mouse spleen and lymph node with NK Cell Isolation Kit (Miltenyi), and cultured for seven days in RPMI-1640 supplemented with 10% FBS, 1% L-glutamine, 100 U/mL penicillin/streptomycin, 50 μ M beta-mercaptoethanol, 1% MEM non-essential amino acids, 1 mM sodium pyruvate, and 1700 U/mL recombinant human IL-2 (rhIL-12). For stimulation, the cultured NK cells were treated with 1 ng/mL recombinant mouse IL-12 and 10 ng/mL recombinant mouse IL-18 (MBL) or Cell Activation Cocktail.

CD8⁺ T cells were isolated from the mouse spleen and lymph node by negative selection according to the manufacture's protocol. They were initially plated at 1×10^6 per well in a 24-

well plate, in the presence of plated-coated anti-CD3 (5 µg/mL) and anti-CD28 (2 µg/mL) and cultured in RPMI1640 medium supplemented with rhIL2 (20 U/mL) and 10% FBS. After 5 days of culture, CD8⁺ T cells were treated with Cell Activation Cocktail.

2.3.6 MTT assay

The in vitro cytotoxicity of MSOP and MAP-4 (GRM4 antagonist), and riluzole (GRM1 antagonist and glutamate transporter inhibitor) against B16, MC38 and 3LL were evaluated and compared by 3- [4, 5-dimethylthiazol-2-yl] -2, 5-diphenyltetrazolium bromide (MTT) assay. Cells were seeded into a 96-well plate at a density of 1500 cells/well (B16 and MC38) and 1800 cells/well (3LL) and incubated in 100 µL of DMEM or RPMI containing 10% FBS. After 12 hours of incubation, cell culture medium was removed and a series of concentrations of MSOP, MAP-4 and riluzole were added into the cells in the presence of 2% FBS DMEM or RPMI. After 48 or 72 hours of incubation, 50 µL of MTT solution (2 mg/mL) were added to each well and the cells were incubated for another 4 hours. After gently removing the medium, 200 µL of DMSO were added into each well so as to dissolve the MTT formazan crystals. The optical density was measured using a microplate reader and the cell viability was calculated using untreated cells as a control.

2.3.7 Preparation and characterization of MSOP CaP nanoparticles

Lipid/Calcium/Phosphate nanoparticles (LCP) were prepared and characterized in vitro and in vivo (Figure 3). At first, LCP cores were prepared by water-in-oil micro-emulsions in the

oil phase containing Igepal CO-520/cyclohexane solution (29/72, v/v) [77]. One hundred and eighty μL of 20 mM MSOP was well mixed with 12.5 mM Na_2HPO_4 (pH = 9.0) to a total volume of 600 μL before adding 20 mL oil phase with continuous stirring. The calcium micro-emulsion was prepared by adding 600 μL of 2.5 M CaCl_2 to a separate 20 mL oil phase. Four hundred μL of 20 mM DOPA in chloroform was added to the phosphate phase and then the two separate micro-emulsions were mixed. After stirring for 5 min, another 400 μL of 20 mM DOPA was added into the emulsion. The emulsion was stirred continuously for 25 min before adding 40 mL absolute ethanol. The ethanol emulsion mixture was centrifuged at 9000 g for 30 min to pellet the LCP core. The LCP core was washed twice with absolute ethanol and dried in the presence of nitrogen. The LCP core pellets were dissolved in 2 mL chloroform and stored in a glass vial at -20°C .

To prepare the MSOP-loaded LCPs (MSOP-LCP-PEG) with an outer lipid coating, 330 μL LCP core in chloroform was mixed with 38.7 μL of 10 mg/mL cholesterol, 28 μL of 25 mg/mL DOTAP, and 96 μL of 25 mg/mL DSPE-PEG. The final molar ratio for cholesterol, DOTAP and DSPE-PEG was 7:7:6. After evaporation of the chloroform, the residual lipids were dissolved in 30 μL THF followed by addition of 50 μL absolute ethanol and 160 μL water. After brief sonication, the solution was dialyzed in distilled water to remove THF and ethanol. The particle size and zeta potential of the formulated MSOP NPs were determined by Dynamic light scattering (DLS) using a Malvern ZetaSizer Nano series. MSOP encapsulation efficiency was measured by UPLC-QTOFMS analysis. Transmission electron microscope (TEM) images of MSOP-loaded NPs were acquired through the use of JEOL 100CX II TEM (Tokyo, Japan).

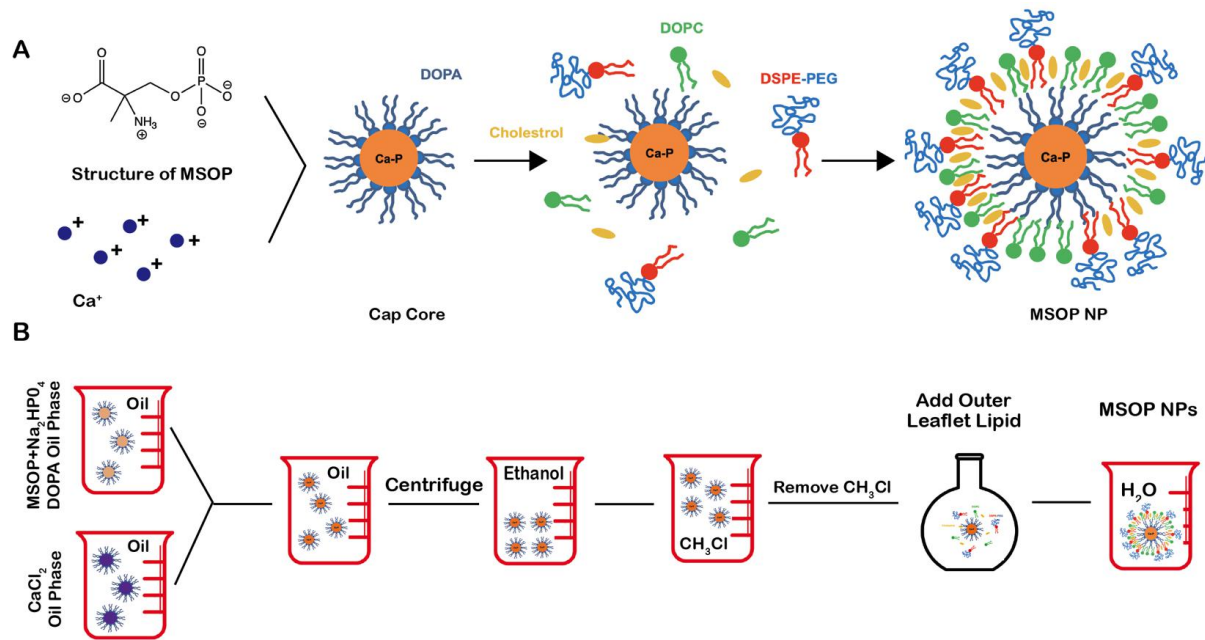


Figure 3. Preparation of MSOP-loaded Cap Nanoparticles. (A) Schematic presentation of the preparation of MSOP-loaded Cap nanoparticles (NPs). (B) Illustration of the steps involved in the preparation of MSOP NPs.

2.3.8 Bulk RNA-Seq analysis

RNA-seq was performed by the Health Sciences Sequencing Core at Children's Hospital of Pittsburgh. RNA-Seq libraries were sequenced as 75-bp paired-end reads at a depth of ~73-77 million reads per sample. Reads were mapped to the mouse genome (GRCm38) using STAR Aligner 2.6.1a [78]. Gene expression quantification and differential expression analysis between *Grm4*^{-/-} and WT was performed using Cuffdiff of Cufflinks 2.2.1 [79]. Volcano plots were generated to show the overall differential expression, where the x-axis indicates the log₂(fold change) (log₂FC) between KO and WT and the y-axis indicates the corresponding -log₁₀(p-value).

To interpret the function of regulated genes in CD45+ cells/tumor cells in Grm4^{-/-} mice in comparison with those in wild-type mice, the gene set enrichment analysis (GSEA) [80, 81] was performed based on the gene list ranked by the log₂FC between KO and WT, using ‘gseapy’ python package. The gene sets we used, including Hallmark gene sets, Kyoto encyclopedia of Genes and Genomes (KEGG) gene sets, gene ontology (GO) gene sets, and other topic related gene sets, were collected and downloaded from Molecular Signatures Database (MSigDB) [80, 82].

2.3.9 Analysis of cancer patient data

Survival analysis was done based on gene expression data and patient clinical information. For TCGA data, gene expression data were downloaded from TCGA Pan-Cancer project (Data Freeze 1.3). Clinical information of TCGA patients were collected from TCGA Pan-Cancer Clinical Data Resource [83]. The other 2 melanoma datasets were downloaded from cBioPortal (<https://www.cbioportal.org/>), including an Acral Melanoma dataset from the Translational Genomics Research Institute [84] and a metastatic melanoma dataset from the Dana-Farber Cancer Institute [85]. Due to the availability of gene expression data and clinical follow-up data of the patients, 33 out of 34 patients in the Acral melanoma dataset and 40 out of 110 patients in the metastatic melanoma data, were used to perform the survival analysis, respectively.

The NK signature consists of the NK-associated genes NCR1, NCR3, KLRB1, CD160, and PRF1 [86]. The CD8 signature consists of the CD8-associated genes CD8A and CD8B. The PKA/Creb immune pathway was summarized from the study of Yao et al [87], including

PRKACA, PRKACB, PRKACG, PRKAR1A, PRKAR1B, PRKAR2A, PRKAR2B, CRTC2, CREB1, IL12RB2, IFNGR1, and IL2RB.

To study the correlation between NK (or CD8)-GRM4 signature and patient survival, we first ranked the patients based on NK (or CD8) signature level.. We also obtained a reversed rank of the patients based on GRM4 expression. Then, we used the average rank of the two metrics to divide the patients into three groups: the top one third were classified as NK (CD8)^{high}-GRM4^{low}, the low one third as NK (CD8)^{low}-GRM4^{high}, while the remaining patients were classified as intermediate. When gender information was included, patients were first separated by gender, and then grouped based on the NK (CD8)-GRM4 signature. Log-rank test was used to compare the survival distribution of NK (CD8)^{high}-GRM4^{low} and NK (CD8)^{low}-GRM4^{high} group.

2.3.10 Single cell sequencing data processing

Data analysis of single cell RNA-Sequencing (scRNA-Seq) was performed with the help of UPMC Genome Center. Paired-end sequencing reads were subjected to Cell Ranger (version 3.0.2, 10x genomics) pipeline analysis. In brief, reads were mapped to the mouse reference genome (mm10) using STAR [78]. Only the reads that can be uniquely aligned to a single gene identifier were used for the unique molecular identifier (UMI) counting. As a result, Cell Ranger recovered 7043, 7877, 3913, 4411 cells in WT-GEX, KO-GEX, WT-TCR, and KO-TCR group, respectively.

We analyzed the UMI count gene-by-cell matrix using the ‘Seurat’ R package [88]. In brief, low quality cells were first filtered out if cells did not satisfy the following criteria: (i) the number of total UMIs must be above 3, (ii) the number of detected genes must be above 200, and (iii) the percentage of UMIs derived from mitochondrial genes must be below 5%. This resulted in 6601, 7171, 3601, 4004 cells in WT-GEX, KO-GEX, WT-TCR, and KO-TCR groups, respectively. We performed gene expression normalizations for each cell according to their total expression, (i) multiplication by a scale factor 10000; (ii) log transformation of the results. Highly variable genes were selected by outlier identification on a mean-variability plot for principal component analysis (PCA), and the first 50 PCs were used for clustering analysis and visualization of the clustering results by t-distributed Stochastic Neighbor Embedding (t-SNE). After clustering cells, we further filtered out the cell clusters which have no expression of CD8a and CD8b genes, ultimately resulting in 1672, 1544, 1504, and 1366 cells being selected in WT-GEX, KO-GEX, WT-TCR, and KO-TCR groups, respectively.

Cluster-specific marker genes were detected by identifying differentially expressed genes between two groups of cells using a Wilcoxon Rank Sum test which was provided in the ‘Seurat’ R-package. (V3.2.3) [https://www.cell.com/cell/fulltext/S0092-8674\(19\)30559-8](https://www.cell.com/cell/fulltext/S0092-8674(19)30559-8)

2.3.11 Single cell T-cell-receptor data processing

The single cell TCR data were processed by Cell ranger (version 4.0.0, 10x genomics) pipeline. The TCR data were first filtered with the following criteria: (i) A barcode must have a contig that aligns to a V segment to be identified as a targeted cell, (ii) There must also be at

least three filtered UMIs with at least two read pairs each. The filtered data were analyzed using the R-package scRepertoire (V 1.1.2) [89]. Clonotypes were removed if any cell barcode had more than two immune receptor chains. ScTCR data were merged with scRNA-seq data of the T cell clusters only based on the cell barcodes. TCR clones that matched barcodes of cells that were not located in T cell clusters (based on our previous annotations using Seurat) were removed. The top 10 most frequent TCRs were labeled and projected in the t-SEN map associated with cell barcode and CDR3 amino acid (aa) sequences. Finally, we calculated the overlap of CDR3 aa sequences from each CD8 clusters in either WT or KO group.

2.3.12 Re-analysis of single-cell RNA-seq and ATAC-seq data

To examine the GRM4 expression in different immune populations, we analyzed publicly available scRNA-Seq data of hepatocellular carcinoma (HCC) [GSE140228 [90]], non-small cell lung cancer (NSCLC) [GSE99254 [91], GSE127465 [92]], and skin cutaneous melanoma (SKCM) [GSE72056 [93]], and RNA-Seq data of CD45⁺ cells from B16 and MC38 tumor models [GSE132748 [94]]. “N/A” indicates that the specific immune populations were not available in a dataset.

To examine the chromatin accessibility of GRM4 promoter in different cell identities, scATAC-Seq data [95] generated from the tumor microenvironment of basal cell carcinoma (BCC) were visualized in the WashU Epigenome Browser.

2.3.13 Statistical analysis

Statistical analysis was performed using GraphPad Prism software. Values are reported as means \pm SEM. When comparing two groups, P values were calculated using two-tailed Student's T tests. For time to event and survival analysis, P values for the Kaplan–Meier survival curves were calculated with a log-rank (Mantel–Cox) test. Significance was conventionally accepted at P values equal to or less than 0.05. For multiple treatment group comparisons, significance was determined by one-way analysis of variance, followed by the Tukey post hoc multiple comparisons test, where *, $P < 0.05$; **, $P < 0.01$; ***, $P < 0.001$; ****, $P < 0.0001$.

Table 2 Resource Table

REAGENT or RESOURCE	SOURCE	IDENTIFIER
Antibodies		
Anti-mouse CD45-BUV395 (30-F11)	BD Biosciences	Cat # 564279
Anti-mouse CD45-PerCP (30-F11)	Biolegend	Cat # 103129
Anti BV510 live/dead	Tonbo Biosciences	Cat # 13-0870-T100
Anti-mouse CD8a-BV480 (53-6.7)	BD Biosciences	Cat # 566169
Anti-mouse CD8a-Pacific Blue	BD Biosciences	Cat # 558106
Anti-mouse CD4-BUV737 (GK1.5)	BD Biosciences	Cat # 564298
Anti-mouse CD4-BV785 (GK1.5)	Biolegend	Cat # 100453
Anti-mouse NK1.1-APC (PK136)	BD Biosciences	Cat # 550627
Anti-mouse NK1.1-APC-Cy7 (IgG2a, κ)	BD Biosciences	Cat # 560618
Rat Anti-CD11b-APC (M1/70)	BD Biosciences	Cat # 553312
Anti-mouse Ly-6G/Ly-6C-PE (Gr-1) (RB6-8C5)	BD Biosciences	Cat # 553128
Anti-mouse Ly-6G/Ly-6C-BV711 (Gr-1) (RB6-8C5)	Biolegend	Cat # 108443
Anti-mouse I-A/I-E (MHCII)-Pacific Blue (IgG2b)	Biolegend	Cat # 107620
Anti-mouse CD24-BV510 (M1/69)	BD Biosciences	Cat # 747717
Anti-mouse F4/80-APC-Cy7 (BM8)	Biolegend	Cat # 123118
Anti-mouse CD103-PE-CF594 (M290)	BD Biosciences	Cat # 565849
Anti-mouse CD11c-BUV737 (HL3)	BD Biosciences	Cat # 612796
Anti-mouse CD366	Biolegend	Cat # 119721
Anti-mouse CD279 (PD-1)-APC-Cy7 (J43)	Biolegend	Cat # 135223
Anti-mouse CD279 (PD-1)-PE (J43)	BD Biosciences	Cat # 561788
Anti-mouse CD223 (Lag3)-BV510 (C9B7W)	BD Biosciences	Cat # 745037
Anti-mouse CD69-APC/Cy7 (H1.2F3)	Biolegend	Cat # 104525
Anti-mouse CD44	Biolegend	Cat # 103037
Anti-mouse/human granzyme B-AF647 (GB11)	Biolegend	Cat # 515405
Anti-mouse/human granzyme B-FITC (GB11)	Biolegend	Cat # 515403
Anti-mouse IFN-r-PE-Cy7 (XMG1.2)	BD Biosciences	Cat # 557649
Anti-mouse S100A9-AF647 (2B10)	BD Biosciences	Cat # 565833
Anti-mouse Foxp3-PE-CF594 (MF23)	BD Biosciences	Cat # 562466
Anti-mouse Ki-67-Pacific Blue (16A8)	Biolegend	Cat # 652421
Ki-67 mAbs-APC (SolA15)	eBioscience	Cat # 17569880
Anti-mouse CD206-FITC (IgG2a)	Biolegend	Cat # 141703
Goat Anti-Rabbit IgG H&L (HRP)	Abcam	Cat # ab205718
Anti-Metabotropic Glutamate Receptor 4/MGLUR4 antibody	Abcam	Cat # ab53088
PE anti-mouse Siglec H Antibody	Biolegend	Cat # 129605
Chemicals, Peptides, and Recombinant Proteins		
Zombie NIR™ Fixable Viability Kit	Biolegend	Cat # 423105
Cell Activation Cocktail (with Brefeldin A)	Biolegend	Cat # 423303
Anti-Mouse Ig, κ/Negative Control Compensation Particles Set	BD Biosciences	Cat # 51909001229
Anti-Rat and Anti-Hamster Ig κ /Negative Control Compensation Particles Set	BD Biosciences	Cat # 51909000949
ACK Lysing Buffer	GIBCO	Cat # A1049201

Liberase™ TL Research Grade	Roche	Cat # 05401020001
Deoxyribonuclease I from bovine pancreas	Sigma	Cat # D5025-150KU
eBioscience™ Permeabilization Buffer (10X)	Invitrogen™	Cat # 501129059
Intracellular Fixation & Permeabilization Buffer	Invitrogen™	Cat # 88882400
Hank's Buffered Saline Solution (HBSS)	Lonza	Cat # BE10-508F
Dulbecco's Modified Eagle Medium (DMEM)	Lonza	Cat # BE12-604F
Hyclone Liquid RPMI 1640 Medium	HyClone	Cat # SH30027.01
Fetal Bovine Serum (FBS)	GIBCO	Cat # 10082147
Trypsin-EDTA solution	Sigma	Cat # T4147
Penicillin-Streptomycin (10,000 U/mL)	GIBCO	Cat # 11548876
Thiazolyl Blue Tetrazolium Bromide	BIOSYNTH	Cat # T-3450
DMSO	Fisher Chemical	Cat # D128-4
Riluzole hydrochloride	TOCRIS	Cat # 0768
(S)-2-Amino-2-methyl-4-phosphonobutanoic acid (MAP-4)	TOCRIS	Cat # 0711
(RS)- α -Methylserine-O-phosphate (MSOP)	TOCRIS	Cat # 0830
1,2-Dioleoyl-3-trimethylammonium-propane chloride salt (DOTAP)	Avanti Polar Lipids, Inc	Cat # 890890P
Dioleoyl phosphatidic acid (DOPA)	Avanti Polar Lipids, Inc	Cat # 840875C
1,2-distearoyl-sn- glycerol-3-phosphoethanolamine-N- [methoxy(polyethyleneglycol-2000) ammonium salt (DSPE-PEG ₂₀₀₀)	Avanti Polar Lipids, Inc	Cat # 880120C
Recombinant Human IL-2 Protein (rhIL-2)	R&D Systems	Cat # 202-IL
<i>InVivo</i> MAb anti-mouse CD8 α	Bio X Cell	BE0004-1
<i>InVivo</i> MAb rat IgG2a isotype control, anti- trinitrophenol	Bio X Cell	BE0089
<i>InVivo</i> MAb anti-mouse NK1.1	Bio X Cell	Cat # BE0036
<i>InVivo</i> MAb anti-mouse PD-1 (CD279)	Bio X Cell	Cat # BP0033-2
<i>InVivo</i> Plus anti-mouse CTLA-4 (CD152)	Bio X Cell	Cat # BP0164
Critical Commercial Assays		
High-Capacity cDNA Reverse Transcription Kit	Applied Biosystems	Cat # 4374966
BCA Protein Assay Kit	Thermo Fisher	Cat # 23225
Power SYBR Green PCR Master Mix	Applied Biosystems	Cat # 4367659
AccuStart™ GelTrack® PCR SuperMix	QuantaBio	Cat # 050118
NK Cell Isolation Kit, Mouse	Miltenyi Biotec	Cat # 130115818
CD8a ⁺ T Cell Isolation Kit, Mouse	Miltenyi Biotec	Cat # 130104075
CD45 (TIL) Micro-Beads, Mouse	Miltenyi Biotec	Cat # 130110618
cAMP Assay Kit (Competitive ELISA)	Abcam	Cat # ab65355
Deposited Data		
RNA-seq data of mouse tumor		This paper
RNA-seq data of isolated CD45 ⁺		This paper
ScRNA-seq data of mouse of NK and T cells		This Paper
ScATAC-seq data derived from BCC	PMID: 31375813	
ScRNA-seq data derived from HCC	PMID: 31675496	GSE140228
ScRNA-seq data derived from NSCLC	PMID: 29942094	GSE99254
ScRNA-seq data derived from NSCLC	PMID: 30979687	GSE127465
ScRNA-seq data derived from SKCM	PMID: 27124452	GSE72056

RNA-seq data of isolated CD45 ⁺ in B16 and MC38 TCGA	PMID: 31350177 PMID: 29625055	GSE132748 Pan-Cancer Clinical Data Resource
Whole exome sequencing and transcriptome analysis of 34 Acral Melanoma patients	PMID: 28373299	
Whole-exosome sequencing of 110 metastatic melanoma tumor normal pairs and data of patient survival	PMID: 26359337	

Software and Algorithms

FlowJo software 10.7-1	FlowJo™	https://www.flowjo.com/solutions/flowjo/downloads
GraphPad Prism	Graphpad	https://www.graphpad.com/scientific-software/prism/
Microsoft Excel	Microsoft	https://www.microsoft.com
Python	Python Software Foundation	https://www.python.org
Cell Ranger version 3.0.2	10x Genomics	https://support.10xgenomics.com/single-cell-gene-expression/software/pipelines/latest/what-is-cell-ranger
R version R ≥ 3.5	R core team	https://www.r-project.org
'Seurat' R package		https://satijalab.org/seurat/

2.4 Results

2.4.1 *Grm4*^{-/-} have significantly delayed tumor growth in male mice

To investigate whether GRM4 has a tumor-suppressive or promoting effect, a series of experiments were performed using three syngeneic tumor models. We first investigated the growth of B16 melanoma cells s.c. inoculated into *Grm4*^{-/-} mice and their wild-type (WT) littermates in a C57BL/6 background (Figure 4A and Figure 5A). No significant difference was observed in tumor growth in the female littermates (Figure 4B and Figure 4C).

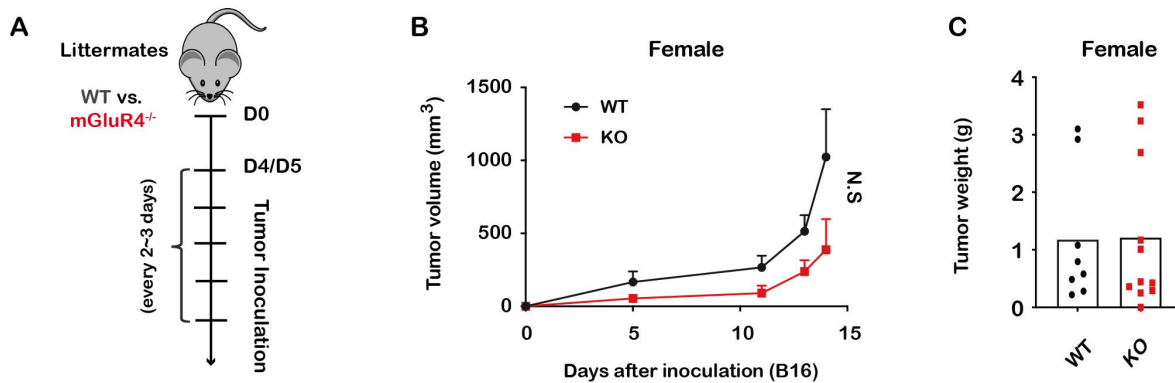


Figure 4 Global Loss of *Grm4* Does Not Significantly Impact Tumor Growth in B16 Tumor Model in Female Mice.

(A-B) Female *Grm4*^{-/-} or WT mice were s.c. inoculated with equal numbers of B16 tumor cells on Day 0 and tumor growth was followed every 2~3 days. (C) Tumors were weighed at the completion of the experiments. Two-way ANOVA was used to determine statistical significance for tumor measurements at time points when all mice were alive. Bar graphs represent data summarized as means \pm S.E.M. and were analyzed by two-tailed unpaired Student's T test. Data shown are representative of three experiments. * $p < 0.05$, ** $p < 0.01$, *** $p < 0.001$, **** $p < 0.0001$, ns (non-significant).

However, in comparison to their *Grm4*^{+/+} littermates, the male *Grm4*^{-/-} mice demonstrated markedly delayed tumor growth (Figure 5B), which was also correlated with a significantly prolonged survival (Figure 5C). Similar results were observed in murine colon adenocarcinoma (MC38) and Lewis lung carcinoma (3LL) models (Figure 5D-F). Collectively, our observations indicated that global loss of *Grm4* markedly inhibited the tumor growth in male mice in multiple murine tumor models. All subsequent studies were performed in male mice.

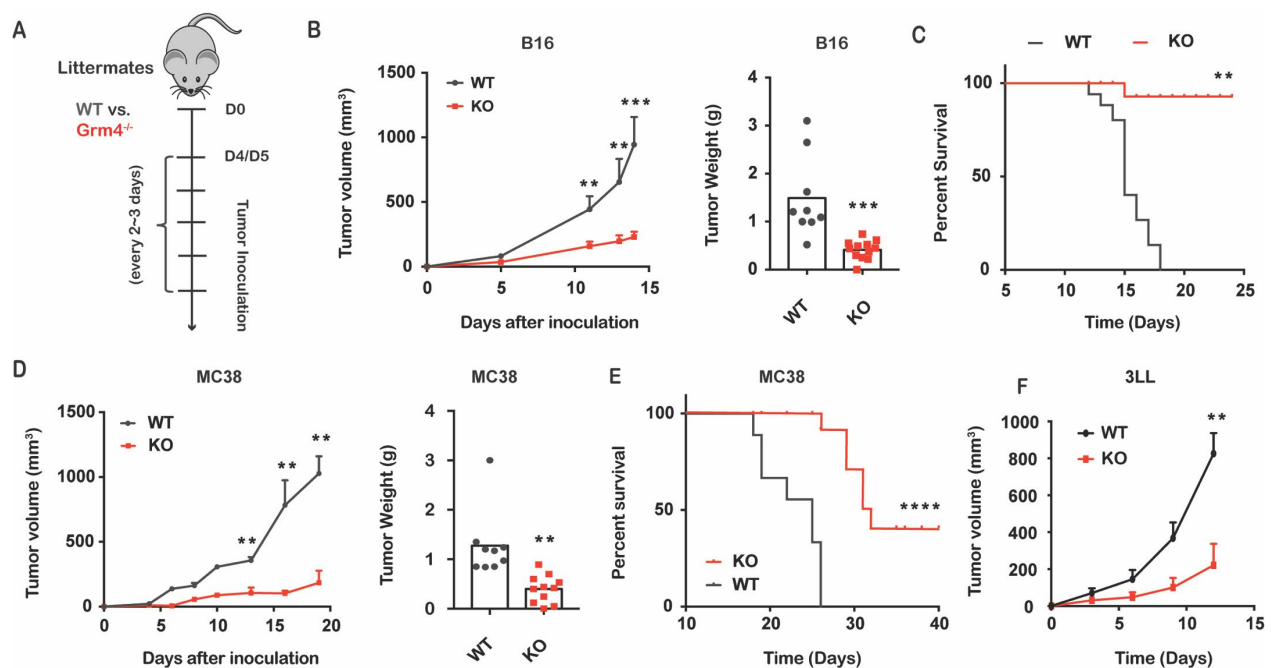


Figure 5 Global Loss of *Grm4* Led to Delayed Tumor Growth in Multiple Tumor Models Through Modulating Tumor Microenvironment

(A-F) Male *Grm4*^{-/-} or WT mice were s.c. inoculated with equal numbers of B16, MC38, and 3LL tumor cells, respectively on Day 0 and tumor growth was followed every 2~3 days. Tumors were weighed at the completion of the experiments (B, D, and F). (C, E) Kaplan-Meier tumor-free survival curves for mice inoculated with B16 or MC38 tumor cells (n = 9~12 mice for each group).

2.4.2 *Grm4*^{-/-} mice skewed tumor microenvironment toward an immunogenic phenotype

To explore the underlying mechanism for this *Grm4*^{-/-}-mediated anti-tumor response, RNA sequencing (RNA-Seq) was performed on B16 tumor tissues harvested from either the *Grm4*^{-/-} or their WT littermates (Figure 5A). This analysis identified 290 significantly upregulated and 260 significantly downregulated genes in tumors from *Grm4*^{-/-} mice (> 1.3-fold, $P < 0.05$) (Figure 5B).

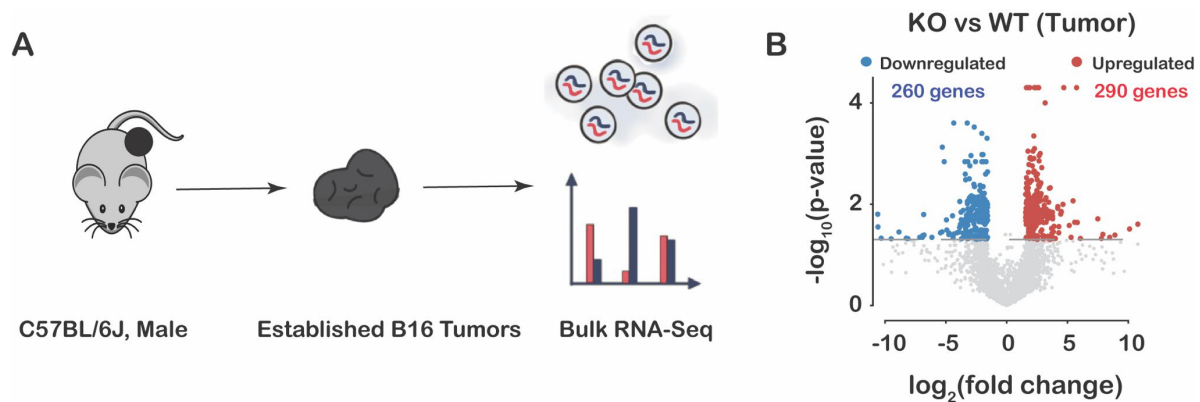


Figure 6 Applying Bulk RNA Sequencing to Study Tumor Microenvironment

(A) Bulk RNA sequencing (RNA-Seq) was applied to the B16 tumor tissues either from *Grm4*^{-/-} or WT mice, and the output data were used for gene expression and pathway analysis. (B) Volcano plot showing all differentially expressed genes between tumor samples from *Grm4*^{-/-} and WT mice. Statistical significance $-\log_{10}(P\text{-value})$ was plotted against \log_2 fold change of gene expression levels (*Grm4*^{-/-}/WT).

Gene set enrichment analysis (GSEA) revealed significant downregulation of several signaling pathways that promote tumor growth, including tricarboxylic acid (TCA)-cycle, ribosome, oxidative phosphorylation, Myc, butanoate metabolism, glycolysis, proteasome, and spliceosome signaling pathways (Figure 2I, **Table. S1**) [96-101], which may partially explain

our observed phenotype in tumor growth. Nonetheless, the most striking changes in *Grm4*^{-/-} mice were related to the immune pathways. Indeed, 10 out of the top 15 upregulated pathways revealed in RNA-Seq were immune-related, suggesting that loss of *Grm4* plays important roles in modulating the tumor immune microenvironment. Among these pathways, the most significantly enriched ones are related to inflammatory response, adaptive immune response, interferon gamma response, natural killer (NK) cells-mediated cytotoxicity, T cell receptor (TCR) signaling, T cell activation, interferon-alpha response, myeloid cell activation, JAK STAT Signaling, toll-like receptor signaling, and innate immune response (Figure 7, Table 3). In addition, we observed significant upregulation in antigen presentation and processing, MHC I protein binding, and MHC II biosynthetic process, along with downregulation of tryptophan metabolism.

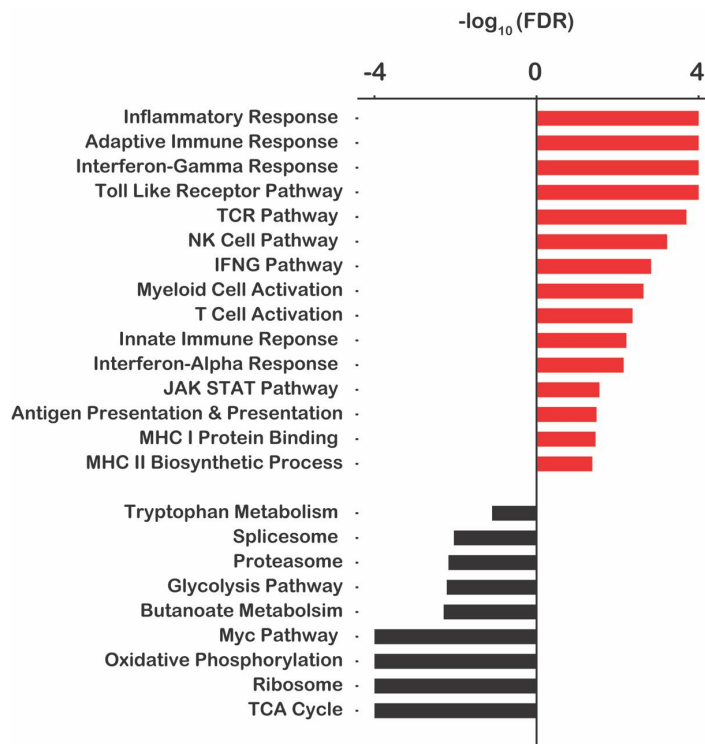


Figure 7 GSEA analysis showing the top enriched gene sets that were significantly regulated in *Grm4*^{-/-} mice.

Table 3 GSEA analysis showing the top enriched gene sets that were regulated in *Grm4*^{-/-} in comparison to WT mice in their tumor samples

	Gene Set	Abbreviation	Size	ES	NES	P-val	FDR
1	HALLMARK_INFLAMMATORY_RESPONSE	Inflammatory Response	200	0.55	2.34	0	0
2	GO_ACTIVATION_OF_INNATE_IMMUNE_RESPONSE	Innate Immune Response	315	0.37	1.64	0.001	0.006
3	GO_ADAPTIVE_IMMUNE_RESPONSE	Adaptive Immune Response	621	0.50	2.25	0	0
4	BIOCARTA_NKCELLS_PATHWAY	NK Cell Pathway	20	0.70	1.95	0	0.0005
5	GO_T_CELL_ACTIVATION	T Cell Activation	459	0.45	2.09	0	0.0042
6	PID_IFNG_PATHWAY	IFNG Pathway	40	0.56	1.88	0.003	0.0014
7	HALLMARK_INTERFERON_GAMMA_RESPONSE	Interferon-Gamma Response	200	0.54	2.33	0	0
8	HALLMARK_INTERFERON_ALPHA_RESPONSE	Interferon-Alpha Response	97	0.50	1.89	0	0.007
9	KEGG_TOLL_LIKE_RECEPTOR_SIGNALING_PATHWAY	Toll Like Receptor Pathway	102	0.59	2.30	0	0
10	KEGG_T_CELL_RECEPTOR_SIGNALING_PATHWAY	TCR Pathway	108	0.55	2.19	0	0.0001
11	KEGG_JAK_STAT_SIGNALING_PATHWAY	JAK STAT Pathway	155	0.43	1.68	0	0.028
12	GO_MHC_CLASS_I_PROTEIN_BINDING	MHC I	20	0.65	1.66	0.015	0.035
13	KEGG_ANTIGEN_PROCESSING_AND_PRESENTATION	Antigen Presentation & Processing	89	0.50	1.65	0.014	0.033
14	GO_MHC_CLASS_II_BIOSYNTHETIC_PROCESS	MHC II	12	0.71	1.70	0.019	0.042
15	GO_MYELOID_CELL_ACTIVATION_INVOLVED_IN_IMMUNE_RESPONSE	Myeloid Cell Activation	41	0.59	1.94	0	0.0022
16	KEGG_TRYPTOPHAN_METABOLISM	Tryptophan Metabolism	40	-0.46	-1.54	0.04	0.08
17	HALLMARK_MYC_TARGETS_V1	MYC Pathway	200	-0.55	-2.79	0	0
18	KEGG_GLYCOLYSIS_GLYCONEOGENESIS	Glycolysis Pathway	62	-0.55	-2.06	0	0.006
19	KEGG_OXIDATIVE_PHOSPHORYLATION	Oxidative Phosphorylation	135	-0.62	-2.91	0	0
20	KEGG_RIBOSOME	Ribosome	88	-0.68	-2.77	0	0
21	KEGG_BUTANOATE_METABOLISM	Butanoate Metabolism	34	-0.61	-2.10	0	0.005
22	KEGG_PROTEASOME	Proteasome	48	-0.54	-2.05	0	0.0066
23	KEGG_SPLICEOSOME	Spliceosome	128	-0.43	-1.97	0	0.009
24	KEGG_CITRATE_CYCLE_TCA_CYCLE	TCA Cycle	32	-0.45	-1.57	0.026	0.082
25	REACTOME_TCA_CYCLE_AND_RESPIRATORY_ELECTRON_TRANSPORT	TCA Cycle	141	-0.65	-3.02	0	0

Further analysis of the above data clearly suggests a more active tumor immune microenvironment in *Grm4*^{-/-} mice as evident from increased transcriptional expression of various genes involved in antitumor activity including (i) Th1 polarizing cytokine *IL-12b* [102, 103]; (ii) T-Cell and NK cell cytotoxic and cytokine genes *Prfl* and *Ifnɣ* [104, 105]; (iii) T cell co-stimulatory molecules *Tnfsf10* and *Tnfsf14*; (iv) T cell activation transcription factors *Stat1*, *Irf3*, *Irf4*, and *Irf9*; (v) Pro-inflammatory cytokines and cytokine receptors *Ccl3*, *Ccl22*, *Il1b*, *Il23a* [106-108], and *Il18r1* [109, 110] (Figure 8). These results suggest that loss of *Grm4* leads to enhanced immune responses in TME, which likely plays an important role in controlling the tumor growth.

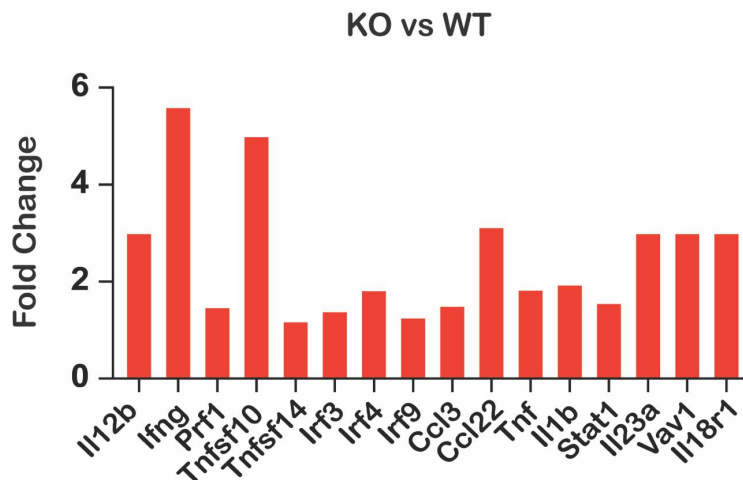


Figure 8 Histograms showing the fold changes in the expression levels of genes differentially expressed between B16 tumors obtained from *Grm4*^{-/-} and WT mice.

2.4.3 GRM4 is expressed in tumor infiltrating immune cells

GRM4 has been shown to be expressed in naïve dendritic cells (DC) and CD4⁺ T cells isolated from mouse splenocytes [33]. Moreover, its expression was identified in the tumor-infiltrating DCs (CD45⁺, MHCII, CD11c) in a mouse model of irradiation-induced osteosarcoma. However, only few CD4⁺ T cells were detectable to characterize GRM4 expression in this bone cancer model [53]. These results demonstrated that expression of GRM4 could be context dependent in the population of immune cells. To date, few studies have examined the expression profile and functionality of GRM4 in immune cells in the context of cancer.

To determine the expression pattern of GRM4 in human cancer TME, we analyzed both the single-cell ATAC-Seq (scATAC-seq) and single-cell RNA-Seq (scRNA-seq) data. By analyzing the chromatin accessibility profile in GRM4 promoter regions in basal cell carcinoma (BCC) tumors (Figure 9), we revealed that the GRM4 promoter regions are generally active in various immune populations, including naïve CD4⁺ T cells, regulatory T (Treg) cells, naïve CD8⁺ T cells, memory CD8⁺ T cells, effector CD8⁺ T cells, and NK cells.

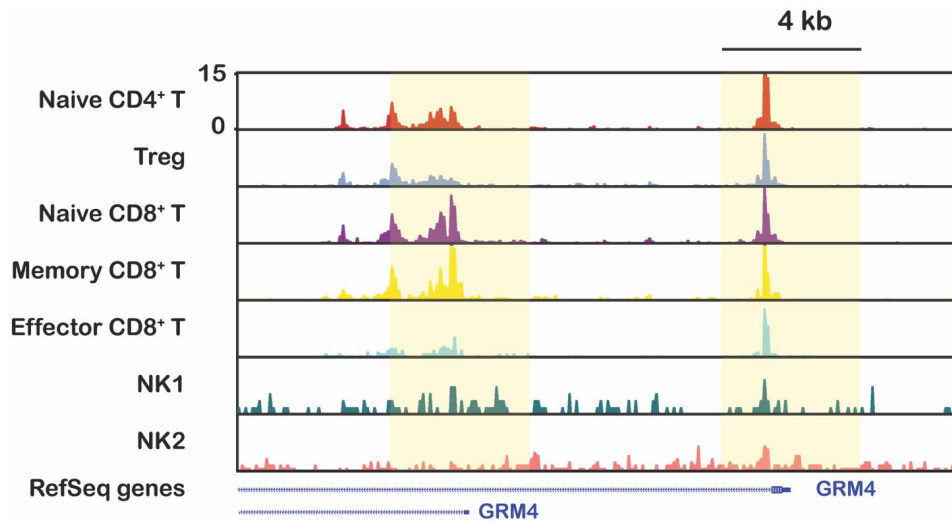


Figure 9 The expression pattern of GRM4.

Genome tracks of aggregate scATAC-seq data in basal cell carcinoma (BCC) TME in patients, peaks indicating the accessible regions (highlighted in yellow) in the promoter regions of GRM4 gene locus.

We have also analyzed four additional scRNA-Seq data from patients with hepatocellular carcinoma (HCC), non-small cell lung cancer (NSCLC), and skin cutaneous melanoma (SKCM). As shown in (Figure 10), the expression of GRM4 was found in several types of immune cells analyzed including CD4⁺ T cells, CD8⁺ T cells, NK cells, DCs, monocytes, and macrophages. We further examined the expression of GRM4 in the tumor-infiltrating immune cells (CD45⁺) isolated from B16 or MC38 tumor-bearing *Grm4*^{+/+} mice.

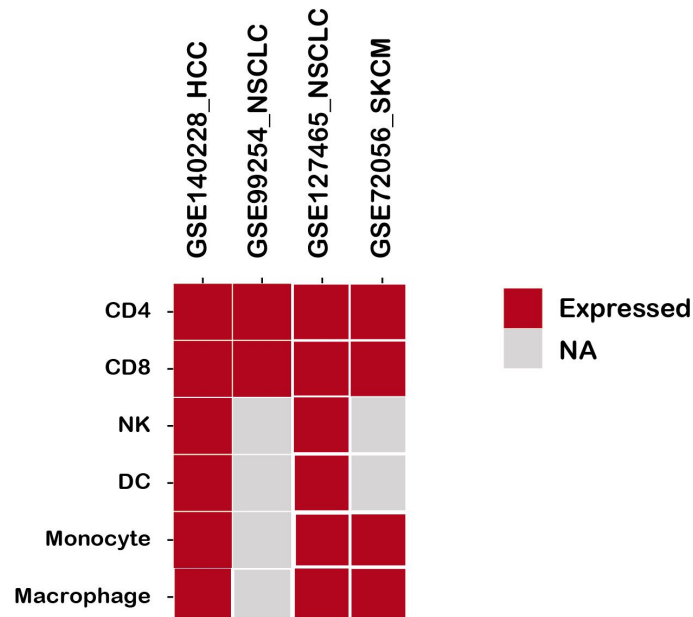


Figure 10 Expression Profiles of GRM4 in Different Tumor-infiltrating Immune Cells in Multiple Cancers.

Single-cell RNA-Seq data of human cancer patients (HCC, NSCLC, and SKCM) were reanalyzed and the expression of GRM4 was confirmed in CD4⁺ T cells, CD8⁺ T cells, NK cells, DCs, monocytes, and macrophages.

NA: not available.

Consistent with the study of Thomas et al., GRM4 was expressed in the tumor-infiltrating CD45⁺ as confirmed by both RNA-Seq (Figure 11A) and flow cytometry (Figure 11B). More specifically, our data have demonstrated that GRM4 was expressed in tumor-infiltrating NK, CD4⁺ T, and CD8⁺ T cells, suggesting those cells as potential targets of GRM4-mediated effects (Figure 11B).

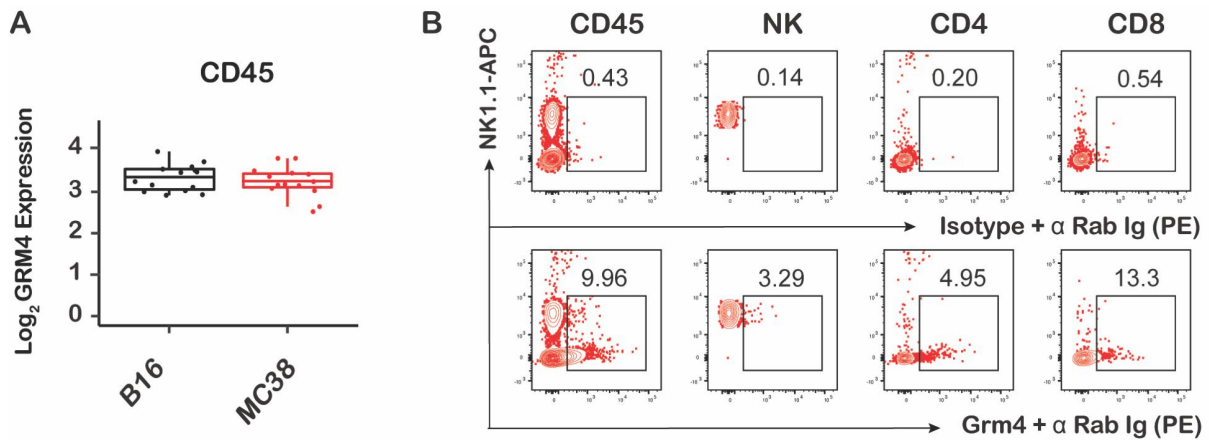


Figure 11 The expression pattern of GRM4 in Tumor-infiltrating Immune Cells in Murine Tumors.

Reanalysis of bulk RNA-Seq data in GEO dataset of WT tumors reveals expression of GRM4 in CD45⁺ cells in B16 and MC38 tumors. (M) Flow cytometry analysis of the expression of GRM4 in tumor-infiltrating lymphocytes CD45⁺, CD45⁺NK1.1⁺, CD45⁺CD4⁺ T cells, and CD45⁺CD8⁺ T cells.

There were no significant differences between male and female *Grm4*^{+/+} mice in the levels of GRM4 expression in several immune cell subpopulations in spleen (NK, CD4⁺ T, and CD8⁺ T cells) as assessed by flow cytometry (Figure 12A). In addition, analysis of Genotype-Tissue Expression (GTEx) Portal database revealed no differences between males and females in humans in the expression levels of *Grm4* in splenocytes (Figure 12B).

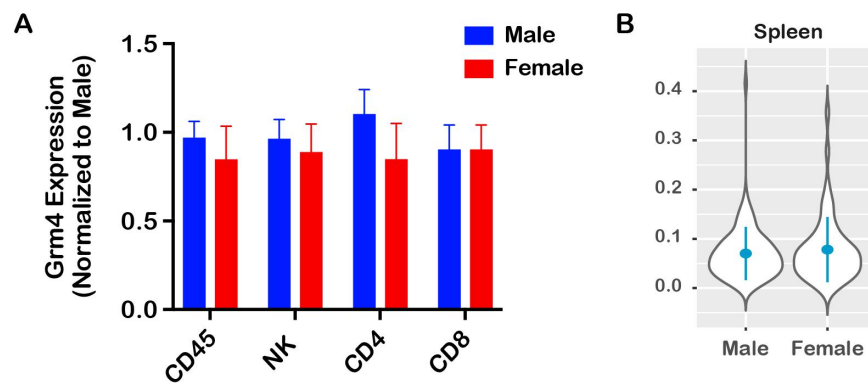


Figure 12 Expression of GRM4 in Male and Female Immune Cells.

(A) Expression of *Grm4* in different immune populations (CD45⁺, NK, CD4⁺ T, and CD8⁺ T cells) isolated from male or female murine splenocytes by flow analysis; (B) Expression of *Grm4* in male or female human splenocytes through analysis of Genotype-Tissue Expression (GTEx) Portal database.

2.4.4 *Grm4*^{-/-} reshapes the landscape of tumor-infiltrating immune cells and the related signaling

The above data suggest that whole-body *Grm4*^{-/-} led to a proinflammatory TME and that GRM4 was expressed in several major immune cell subpopulations. To further investigate how the *Grm4*^{-/-} shaped the TME and the antitumor response, we characterized tumor-infiltrating leukocytes (TILs) in B16 tumor model by flow cytometry. As shown in Figure 13A, both the percentage and the total number of CD45⁺ leukocytes were significantly increased in B16 tumors of *Grm4*^{-/-} mice versus WT control. To more clearly define the global changes in immune profile after *Grm4*^{-/-}, we further performed RNA seq on FACS-sorted tumor-infiltrating CD45⁺ cells from the *Grm4*^{-/-} and the WT littermates (Figure 13B). There are distinct differences between the gene expression profiles of the tumor-infiltrating CD45⁺ cells from *Grm4*^{-/-} and the WT mice, with significant upregulation of 290 genes and the significant repression of 247 genes (> 1.3-fold, $P < 0.05$) (Figure 13C). GSEA showed that CD45⁺ cells from the *Grm4*^{-/-} mice have a transcriptional program that is enriched with pathways that promote anti-tumor immunity, which is consistent with the enhanced anti-tumor immunity in tumor tissues (RNA-Seq) (Figure 13D, **Table. 4**).

Table 4 GSEA analysis of the top enriched gene sets that were upregulated in CD45⁺ cells from B16 tumor bearing Grm4^{-/-} mice.

	Gene Set	Abbreviation	Size	ES	NES	P-val	FDR
1	KEGG_NATURAL_KILLER_CELL_MEDIATED_CYTOTOXICITY	NK Cytotoxicity pathway	137	0.358	1.445	0.02	0.146
2	GO_NK_T_CELL_ACTIVATION	NK&T activation Pathway	12	0.744	1.858	0.004	0.003
3	GO_POSITIVE_REGULATION_OF_ACTIVATED_T_CELL_PROLIFERATION	Activated T Cell Proliferation Pathway	27	0.547	1.610	0.02	0.057
4	GO_POSITIVE_REGULATION_OF_ALPHA_BETA_T_CELL_PROLIFERATION	$\alpha\beta$ T cell Proliferation Pathway	19	0.735	2.069	0	0
5	GO_LYMPHOCYTE_ACTIVATION_INVOLVED_IN_IMMUNE_RESPONSE	Lymphocyte activation	98	0.479	1.927	0	0.007
6	GO_T_CELL_ACTIVATION_INVOLVED_IN_IMMUNE_RESPONSE	T Cell Activation	60	0.492	1.722	0.008	0.021
7	GO_POSITIVE_REGULATION_OF_ALPHA_BETA_T_CELL_ACTIVATION	$A\beta$ T Cell Activation Pathway	62	0.575	2.174	0	0.0012
8	GO_POSITIVE_REGULATION_OF_CD4_POSITIVE_ALPHA_BETA_T_CELL_ACTIVATION	$A\beta$ CD4 T Activation Pathway	35	0.671	2.283	0	0
9	GO_CD8_POSITIVE_ALPHA_BETA_T_CELL_ACTIVATION	$A\beta$ CD8 T Cell Activation Pathway	23	0.435	1.299	0.132	0.152
10	GO_CYTOKINE_PRODUCTION_INVOLVED_IN_IMMUNE_RESPONSE	Cytokine production	17	0.551	1.486	0.064	0.078
11	HALLMARK_INTERFERON_GAMMA_RESPONSE	IFN- γ Pathway	200	0.514	2.362	0	0
12	HALLMARK_INTERFERON_ALPHA_RESPONSE	IFN- α Pathway	97	0.562	2.295	0	0
13	KEGG_TOLL_LIKE_RECEPTOR_SIGNALING_PATHWAY	Toll Like Receptor Pathway	102	0.467	1.897	0	0.007
14	KEGG_T_CELL_RECEPTOR_SIGNALING_PATHWAY	TCR Pathway	108	0.419	1.752	0	0.021
15	KEGG_RIG_I_LIKE_RECEPTOR_SIGNALING_PATHWAY	RIG-I Pathway	71	0.456	1.698	0.002	0.029
16	HALLMARK_IL2_STAT5_SIGNALING	IL2-STAT5 Pathway	200	0.320	1.487	0	0.115
17	HALLMARK_TNFA_SIGNALING_VIA_NFKB	TNF Pathway	200	0.462	2.180	0	0
18	GO_REGULATION_OF_T_HELPER_1_TYPE_IMMUNE_RESPONSE	Type I T-helper Pathway	22	0.652	1.978	0.0023	0.007
19	GO_POSITIVE_REGULATION_OF_IMMUNE_EFFECTOR_PROCESS	Immune effector	156	0.425	1.905	0	0.007
20	GO_T_CELL_DIFFERENTIATION_INVOLVED_IN_IMMUNE_RESPONSE	T differentiation Pathway	29	0.572	1.892	0	0.008
21	GO_POSITIVE_REGULATION_OF_PRODUCTION_OF_MOLECULAR_MEDIATOR_OF_IMMUNE_RESPONSE	Molecular Mediator Production Pathway	64	0.485	1.836	0.002	0.009
22	GO_IMMUNOGLOBULIN_PRODUCTION_INVOLVED_IN_IMMUNOGLOBULIN_MEDIATED_IMMUNE_RESPONSE	Immunoglobulin Pathway	24	0.625	1.732	0.018	0.021
23	GO_REGULATION_OF_CYTOKINE_SECRETION_INVOLVED_IN_IMMUNE_RESPONSE	Cytokine secretion pathway	11	0.784	1.734	0.009	0.022
24	GO_POSITIVE_REGULATION_OF_TYPE_2_IMMUNE_RESPONSE	Type II Immune Response	26	0.526	1.685	0.009	0.024
25	GO_IMMUNE_RESPONSE_REGULATING_CELL_SURFACE_RECEPTOR_SIGNALING_PATHWAY	Cell surface receptor pathway	323	0.29	1.464	0	0.085

As shown in Figure 14A and Figure 14B, the percentage of NK cells in the tumors was increased strikingly in *Grm4*^{-/-} mice. The absolute numbers of the NK cells in the tumors were also significantly higher in the *Grm4*^{-/-} mice compared to those in WT mice (Figure 14B). GSEA plots showed that the signaling of NK cells-mediated cytotoxicity was significantly enriched in *Grm4*^{-/-} mice compared to WT mice (normalized enrichment score [NES] = 1.544; FDR = 0.026) (Figure 14C). There were no significant differences in the percentages of CD4⁺ T or CD8⁺ T cells in B16 tumors between WT and *Grm4*^{-/-} mice. However, because of a large increase in CD45⁺ TILs overall, the total numbers of CD4⁺ and CD8⁺ T cells were significantly increased (Figure 14D and Figure 14E). This is likely due to increases in both recruitment and local proliferation of CD4⁺ and CD8⁺ T cells. Along with increases in the numbers of CD4⁺ and CD8⁺ T cells, GSEA plots showed that TCR signaling was significantly enriched in *Grm4*^{-/-} mice (NES = 1.772, FDR = 0.018) (Figure 14 F).

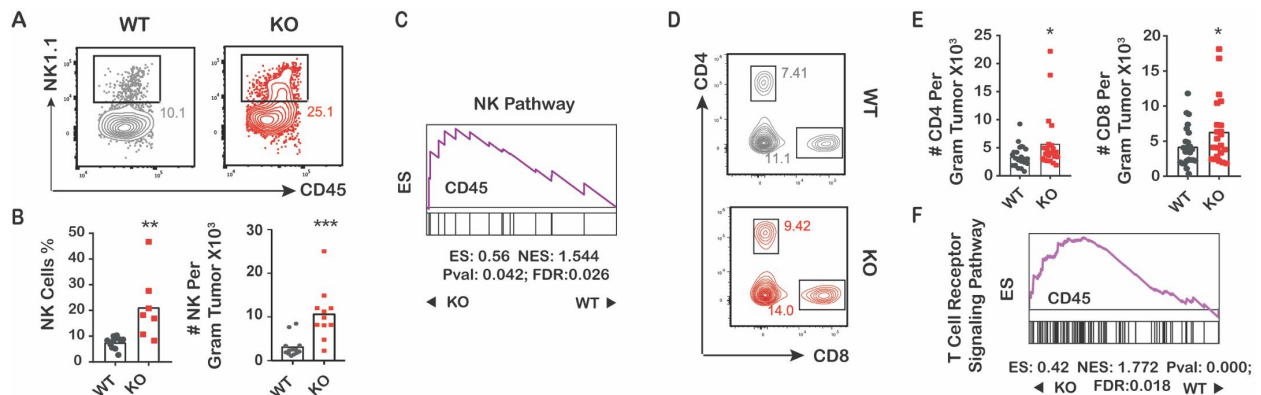


Figure 14 Global Loss of *Grm4* Led to Delayed Tumor Growth in B16 Tumor Models Through Recruiting NK, CD4⁺, and CD8⁺ T Cells.

(A) Representative flow cytometric plots of NK 1.1⁺ cells. (B) The quantification of the percentages and the numbers of NK1.1⁺ cells within the gated CD45⁺ population in the tumor tissues from WT or *Grm4*^{-/-} mice. (C)

GSEA analysis of upregulated NK cytotoxicity pathway in tumor tissues from *Grm4^{-/-}* mice in comparison to WT mice. (D) Representative flow cytometric plots of CD4⁺ and CD8⁺ T cells. (E) The quantification of the percentages and the numbers of infiltrated CD4⁺ and CD8⁺ T cells in the tumor tissues. (F) GSEA analysis of upregulation of T cell receptor signaling pathway in tumor tissues from *Grm4^{-/-}* mice in comparison to WT mice.

Various classes of cell types derived from the mononuclear phagocyte system (MPS) [111], such as tumor infiltrating monocytes, macrophages and myeloid-derived suppressor cells (MDSCs), have been implicated in promoting tumor development and metastasis while inhibiting a productive immune response by T cells and NK cells [112-114]. FACS analysis revealed no differences in the monocyte (Figure 15A) and macrophage (Figure 15B) populations between WT and *Grm4^{-/-}* mice. However, the percentage of tumoral MDSCs (CD11b⁺ Gr1⁺) was significantly decreased in *Grm4^{-/-}* mice (Figure 15C). Along with this change, GSEA plots further showed that MDSC signaling pathway was significantly downregulated in *Grm4^{-/-}* mice (NES = -1.226, FDR = 0.066).

DCs, another cell type derived from the MPS, are the preeminent antigen presenting cells (APCs) for T cells in lymphoid organs and in tissues. As shown in Figure 15D, the number of DCs was significantly increased in *Grm4^{-/-}* mice. GSEA plots showed that antigen processing and presentation was significantly upregulated in tumors isolated from *Grm4^{-/-}* mice (NES = 1.784, FDR = 0.016). The level of MHC class II molecules was also significantly increased (Figure 15E). GSEA plots showed that MHC II protein synthesis was strikingly enriched in *Grm4^{-/-}* mice (NES = 1.548, $P < 0.05$). The higher levels of MHC II suggest that the APC cells are most likely to be effective for incoming effector T cells [111].

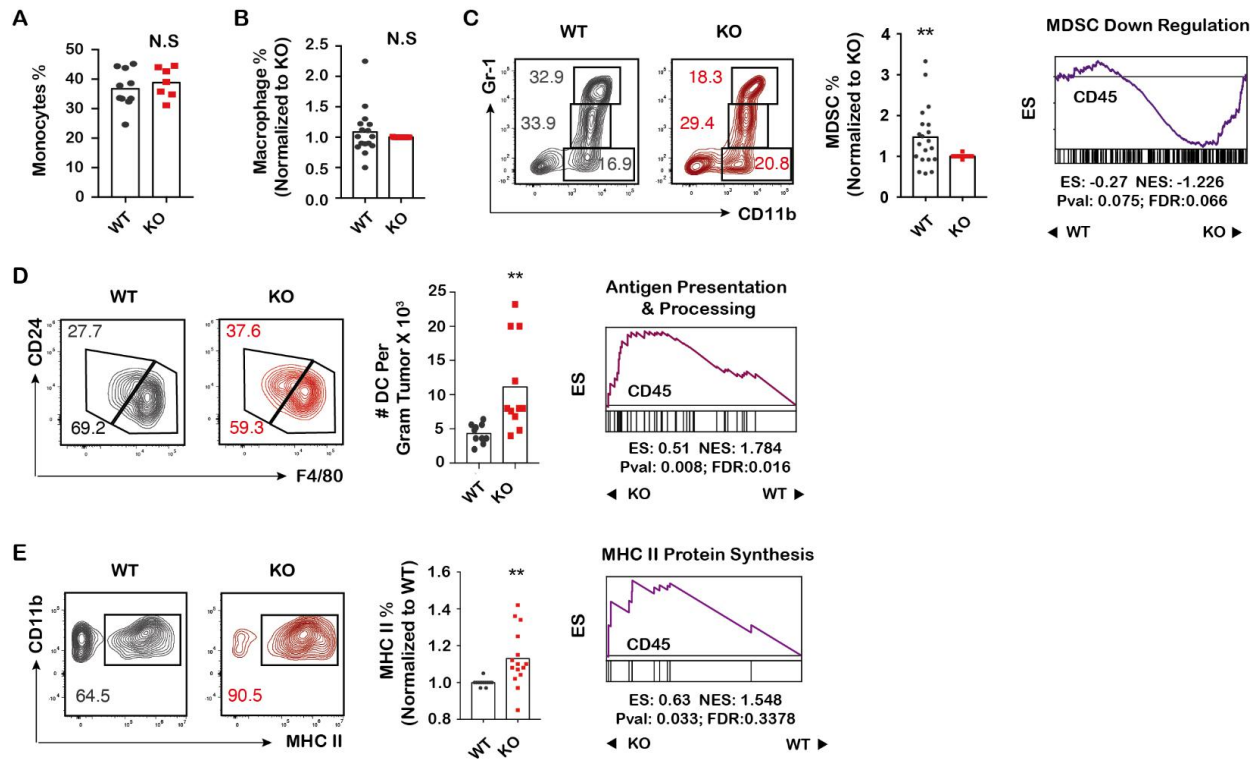


Figure 15 Global Loss of *Grm4* Led to Delayed Tumor Growth in B16 Tumor Models Through Modulating Mononuclear Phagocyte System.

(A-B) Quantification of the percentages of TIL monocytes (A) and tumor associated macrophages (B). (C) Representative flow cytometric plots, the quantification of the relative percentage of MDSCs in the tumor tissues from WT and *Grm4*^{-/-} mice, and GSEA of downregulated MDSC pathway in CD45⁺ from *Grm4*^{-/-} mice in comparison to WT mice. (D) Representative flow cytometric plots, the quantification of the numbers of DCs, and GSEA of upregulated antigen presentation & processing pathway in CD45⁺ from *Grm4*^{-/-} mice in comparison to WT mice. (E) Representative flow cytometric plots, the quantification of the relative percentage of MHC II⁺ cells, and GSEA of upregulated MHC II protein synthesis pathway in CD45⁺ from *Grm4*^{-/-} mice in comparison to WT mice.

The above data suggest that *Grm4*^{-/-} promoted an immunostimulatory TME, which was favorable for anti-tumor immune responses in B16 tumor model. A similar study was also conducted in MC38 syngeneic tumor model, which is a more immunogenic model than B16 [115]. Compared to B16, MC38 model showed similar trends of changes in CD45⁺, NK cells,

CD4⁺ T cells, CD8⁺ T cells, monocytes, macrophages, MDSCs and DCs after *Grm4*^{-/-} (Figure 16A-J). In addition, the changes in T cells were more dramatic in the MC38 tumor bearing mice.

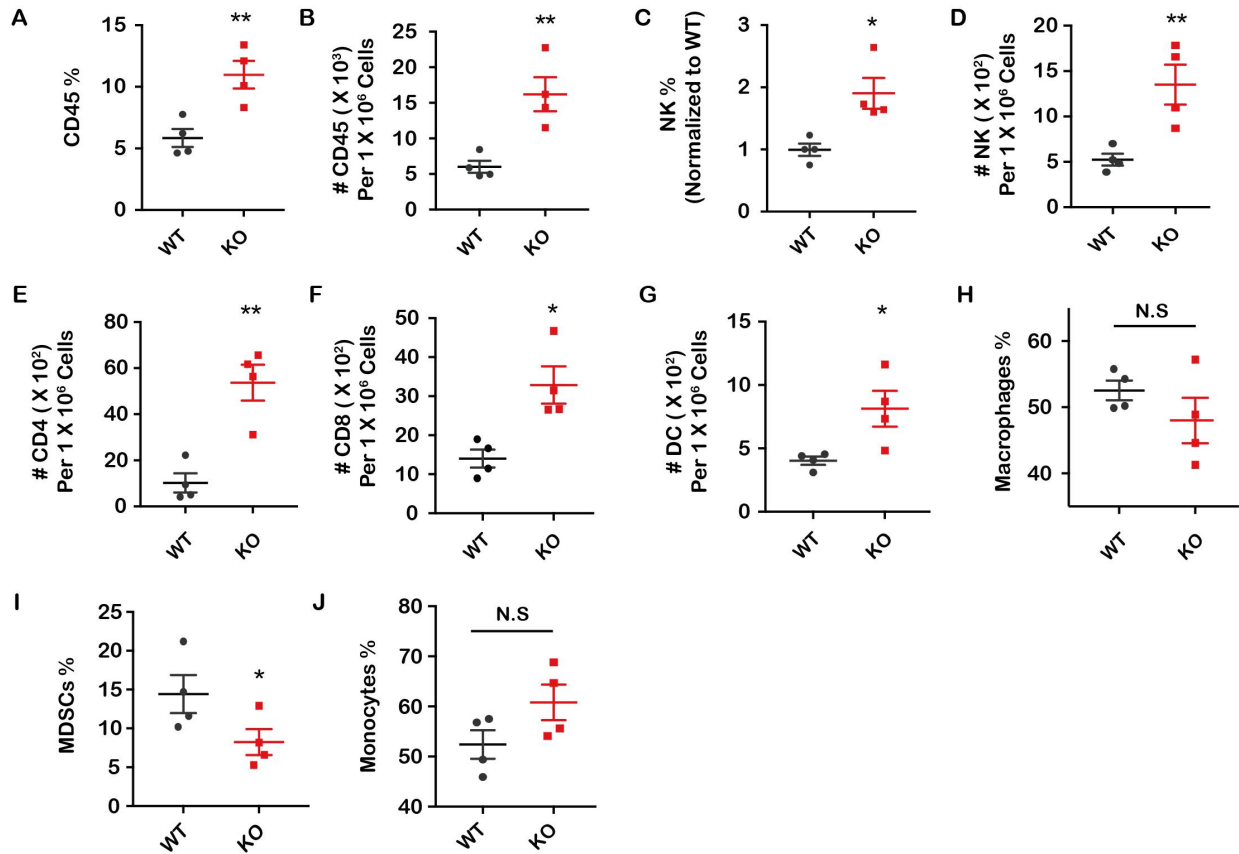


Figure 16 Depletion of *Grm4* Shaped the Immunogenic Tumor Microenvironment in MC38 Murine Colon Cancer Model.

(A-B) Flow cytometric analyses demonstrate significantly higher percentages and numbers of infiltrated CD45⁺ in the tumor tissues from *Grm4*^{-/-} in comparison to WT mice. (C-D) Flow cytometric analyses demonstrate significantly higher percentages and numbers of infiltrated NK cells in the tumor tissues from *Grm4*^{-/-} in comparison to WT mice. (E-G) Flow cytometric analyses demonstrate significantly higher numbers of infiltrated CD4⁺ T, CD8⁺ T cells and DCs in the tumor tissues from *Grm4*^{-/-} in comparison to WT mice. (H) No significant changes in the infiltration of macrophages between WT and *Grm4*^{-/-} mice. (I) There are significantly fewer infiltrated MDSCs in *Grm4*^{-/-} mice in comparison to WT mice. (J) No significant changes in the infiltration of monocytes between WT and

Grm4^{-/-} mice. Strip Plots represent data summarized as mean ± S.E.M. and were analyzed by two-tailed unpaired Student's T test. *p < 0.05, **p < 0.01, ***p < 0.001, ****p < 0.0001, ns (non-significant).

Interestingly, although we observed an increase in the total number of CD45⁺ cells in female B16 tumor-bearing *Grm4*^{-/-} mice compared to female WT mice, there were no significant differences in other immune populations including CD8⁺ T cells and IFN- γ producing CD8⁺ T cells (Figure 17A- F). Taken together, these data suggested a pivotal role of immune cells in *Grm4*^{-/-}-mediated anti-tumor response.

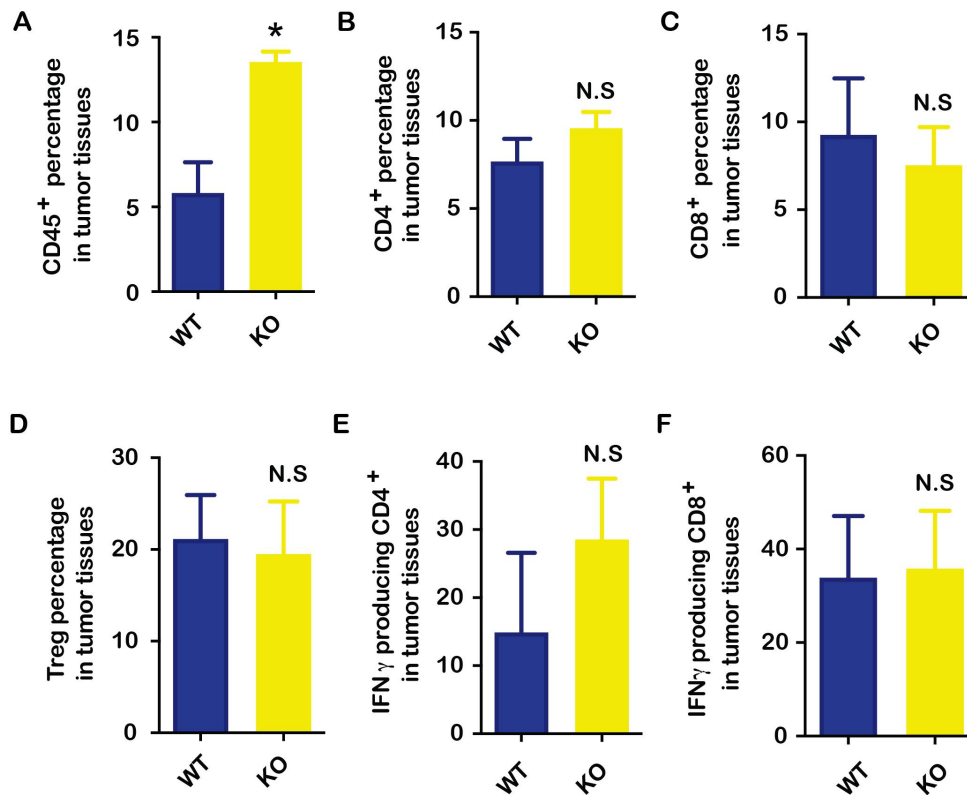


Figure 17 Depletion of *Grm4* Demonstrated Less Impact on Tumor Immune Microenvironment in B16 Murine Melanoma Model in Female mice.

2.4.5 *Grm4*^{-/-} conditions NK, CD4⁺ T, CD8⁺ T cells toward a highly proliferative and activated phenotype

Our studies so far have shown significant changes in the numbers of immune cell populations and the associated gene expression profiles after loss of *Grm4*. Further studies showed that the most dramatic changes in the proinflammatory cytokine profiles were associated with NK, CD4⁺ and CD8⁺ T cells (RNA-Seq from isolated CD45⁺) (Figure 13D, **Table. S2**). We went to further characterize the functionality of the three immune cell subpopulations via flow cytometry. Ki-67 is a marker of cell proliferation and CD44 is a cell activation marker. (Figure 18A and Figure 18B) shows that the expression levels of Ki-67 were significantly upregulated in *Grm4*^{-/-} NK cells, CD4⁺ T and CD8⁺ T cells in comparison to WT controls. GSEA analysis indicates that T cell proliferation pathway was significantly upregulated (NES = 2.069, FDR = 0.000) (Figure 18D). Similar results were obtained for the expression profile of CD44 in all three immune cell subpopulations (Figure 18B). GSEA analysis further confirmed the activation of NK (NES = 1.858, FDR = 0.003) (Figure 18E) and T cell at transcriptional level (NES = 2.174, FDR = 0.001) (Figure 18F). Upon activation and clonal expansion, these immune cells gain effector functions and can produce large quantities of effector cytokines such as IFN- γ and Granzyme B. IFN- γ is produced predominantly by NK cells, CD4⁺ and CD8⁺ T cells as part of the innate and adaptive immune responses, respectively [116]. (Figure 18C) shows that *Grm4* deficiency led to significant increases in the expression levels of IFN- γ among all three immune cell subpopulations, indicative of their heightened effector cytokine production. GSEA plots show that IFN- γ signaling pathway was significantly enriched (NES = 2.362, FDR = 0.000) (Figure 18G, **and Table. 4**) and ranked top among the cytokine pathways.

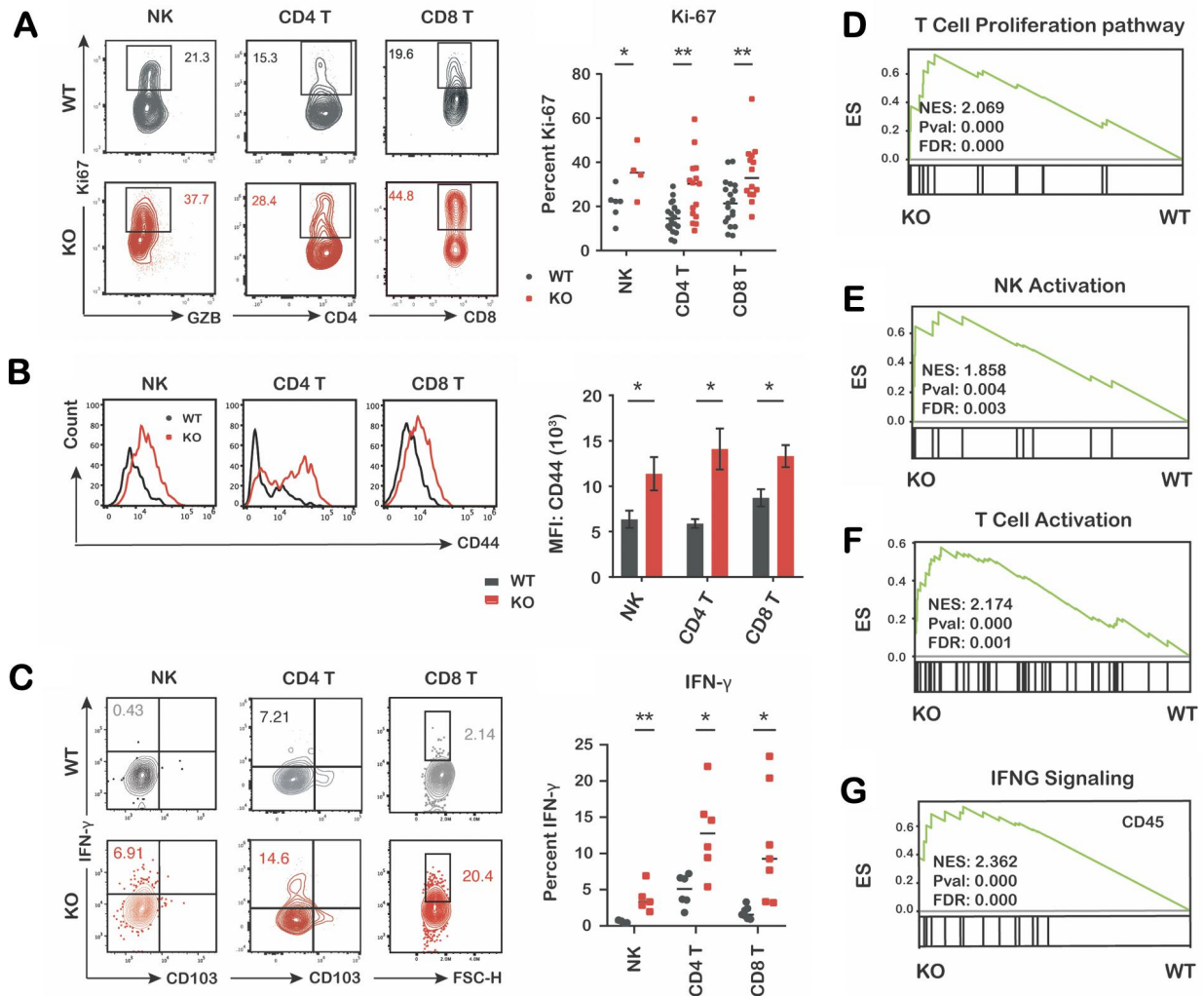


Figure 18 Global Loss of Grm4 Led to Delayed Tumor Growth in Multiple Tumor Models Through Conditioning NK, CD4⁺ T, and CD8⁺ T Cells Toward a Highly Proliferative and Activated Phenotype.

(A) Flow cytometric plots and strip plots depicting the percentages of Ki-67⁺-positive NK, CD4⁺ T, and CD8⁺ T cells. (B) Representative histograms showing the mean fluorescence intensity (MFI) of CD44⁺ cells within NK cells, CD4⁺ T cells, and CD8⁺ T cells and Bar graphs indicating the median fluorescence intensity (MFI) of CD44⁺ cells within NK, CD4⁺ T, and CD8⁺ T cells. (C) Flow cytometric plots and bar graphs depicting the percentages of IFN- γ producing NK, CD4⁺ T, and CD8⁺ T cells. (D) GSEA of upregulation of T cell proliferation pathways in isolated CD45⁺ cells from Grm4^{-/-} mice in comparison to WT mice. (E) GSEA of upregulation of NK and (F) T cell activation pathways in isolated CD45⁺ cells from Grm4^{-/-} mice in comparison to WT mice. (G) GSEA of upregulation of IFNG signaling pathways in isolated CD45⁺ cells from Grm4^{-/-} mice in comparison to WT mice

The above data showed drastic changes in immune landscape in TME of *Grm4*^{-/-} mice. A preliminary study was also conducted to examine changes in spleen to evaluate a role of GRM4 in mediating systemic anti-tumor immunity. No significant differences were observed in the IFN- γ -producing NK cells in mouse spleen (Figure 19A). However, the expression of IFN- γ was significantly upregulated in CD4⁺ and CD8⁺ T cells in *Grm4*^{-/-} mice (Figure 19B), suggesting GRM4 regulates same sets of genes in the tumor tissues and secondary lymphoid system [117]. There were no statistical differences in the percentages of granzyme B (GZB)-producing NK and CD8⁺ T cells (Figure 19C and Figure 19D) in both tumors and spleens, despite that there were trends of increased GZB-producing CD8⁺ T cells. Taken together, our data suggest that *Grm4* deficiency promotes TIL activation, proliferation, and IFN- γ production.

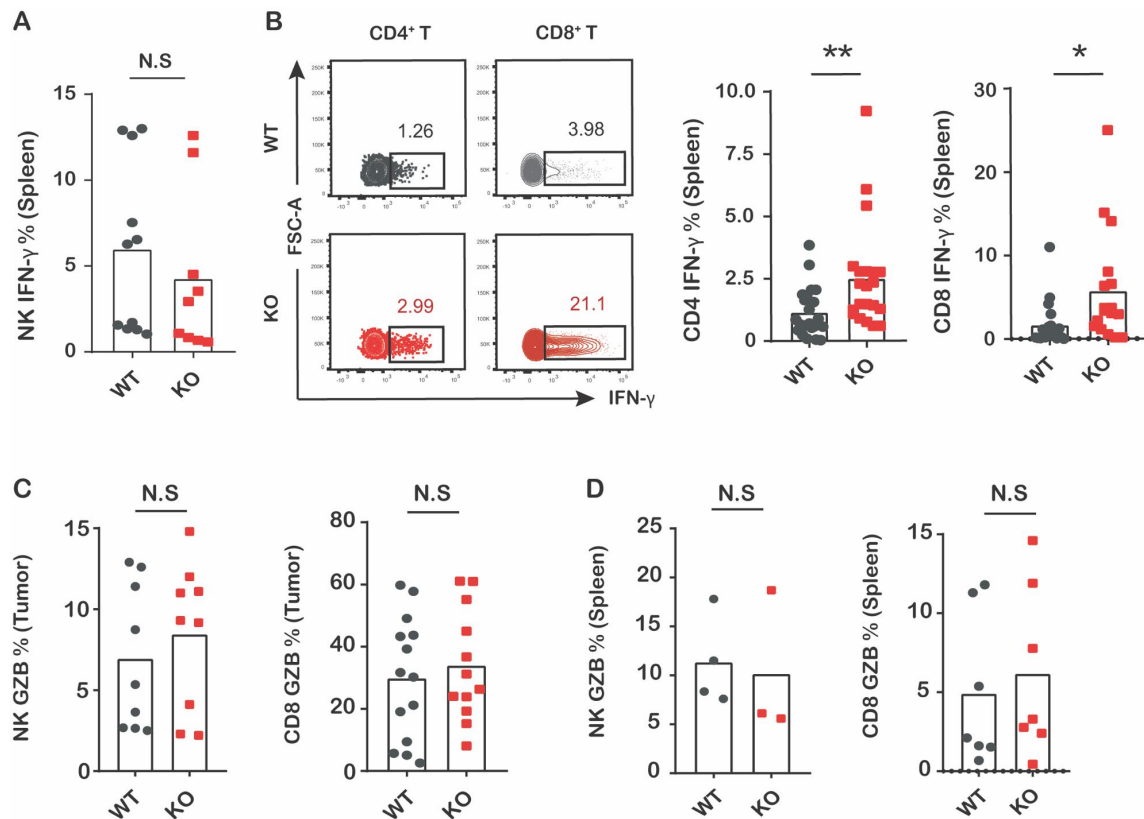


Figure 19 Depletion of *Grm4* Shaped the Spenocytes Microenvironment in B16 Murine Melanoma Model.

(A) Quantification of bar graphs depicting the percentages of IFN- γ producing NK cells in splenocytes from tumor-bearing *Grm4^{-/-}* and WT mice. (B) Flow cytometric plots and the quantification of bar graphs depicting the percentages of IFN- γ producing CD4⁺ T and CD8⁺ T cells in splenocytes from tumor-bearing *Grm4^{-/-}* and WT mice. (C-D) Bar graphs depicting the percentages of GZB-producing NK and CD8⁺ T cells in tumor tissues (C) and splenocytes (D) from tumor-bearing *Grm4^{-/-}* and WT mice. Bar graphs represent data summarized as mean \pm S.E.M. and were analyzed by two-tailed unpaired Student's T test. *p < 0.05, **p < 0.01, ***p < 0.001, ****p < 0.0001, ns (non-significant).

2.4.6 *Grm4^{-/-}*-mediated tumor regression is dependent on NK and CD8⁺ T cells

NK cells play an important role in cancer innate immunity while CD8⁺ T cells are critically involved in the adaptive immune response against cancer [118, 119]. In addition, these two populations can directly engage with and kill the tumor cells in comparison to many other immune cells. In the *Grm4^{-/-}* TME, NK and CD8⁺ T cells were not only increased in numbers but also conditioned to be more active, proliferative, and functional. We sought to characterize the role of NK and CD8⁺ T cells in the significant tumor inhibition in *Grm4^{-/-}* mice. NK and CD8⁺ T cell neutralizing monoclonal antibodies (mAbs) were used for depletion of NK or CD8⁺ T cells, respectively, and the tumor growth was similarly monitored as described before. Consistent with the data of an early study, B16 tumor grew significantly slower in *Grm4^{-/-}* mice compared to WT mice when they were treated with an isotype-matched control IgG. Intraperitoneal (IP) injection of either anti-NK or anti-CD8 mAb significantly abolished the tumor growth inhibition in the *Grm4^{-/-}* mice (Figure 20). This implies that both NK cells and cytotoxic CD8⁺ T cells contributed significantly to the anti-tumor immunity in *Grm4^{-/-}* mice.

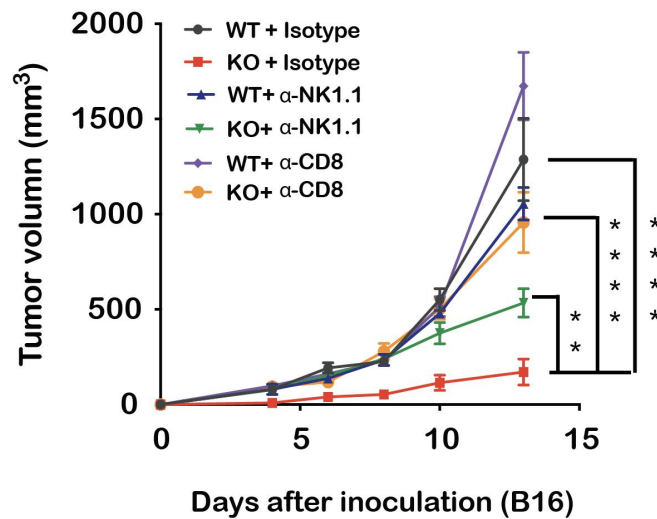


Figure 20 *Grm4*^{-/-}-mediated tumor regression is dependent on NK and CD8⁺ T cells

Grm4^{-/-} and WT mice inoculated with B16 tumor cells were injected i.p. with anti-CD8 or anti-NK1.1 antibody or isotype-matched control IgG. Tumor sizes were measured every 2~3 days (n = 5). **p < 0.01 (anti-CD8 or anti-NK1.1 vs control IgG).

2.4.7 *Grm4*^{-/-}-triggered immune activation is associated with induction of immune resistance and synergizes with treatment with immune checkpoint inhibitors

Although *Grm4*^{-/-} led to an immune-active TME, it also triggered concurrent induction of immune checkpoint molecules. The RNA-seq data of either the tumor tissues or isolated CD45⁺ cells revealed significant upregulation of PD-1 and CTLA-4 signaling (Figure 21A). Consistent with RNA-Seq data, FACS showed significant upregulation of PD-1 expression in NK cells, CD4⁺ T cells, and CD8⁺ T cells (Figure 21B) in tumors from *Grm4*^{-/-} mice. In addition, we observed higher percentages of FoxP3⁺ CD4⁺ Treg cells in tumor tissues and splenocytes of *Grm4*^{-/-} mice (Figure 21C). CTLA-4 is constitutively expressed in mouse Treg cells [120], in

part because FOXP3 directs CTLA-4 transcription [121]. This is consistent with the upregulated CTLA-4 signaling as described above.

The induction of PD-1/CTLA-4 signaling is likely attributed to a feedback mechanism following immune activation [122]. We hypothesize that the tumor growth inhibition in *Grm4*^{-/-} mice can be further improved through combination with anti-PD-1- or anti-CTLA-4-based immune checkpoint blockade (ICB). Indeed, treatment with anti-PD-1 antibody led to further growth inhibition of B16 tumors in *Grm4*^{-/-} mice compared to *Grm4*^{-/-} mice treated with control IgG (Figure 21D). Similar results were seen in *Grm4*^{-/-} mice treated with anti-CTLA-4 antibody (Figure 21D).

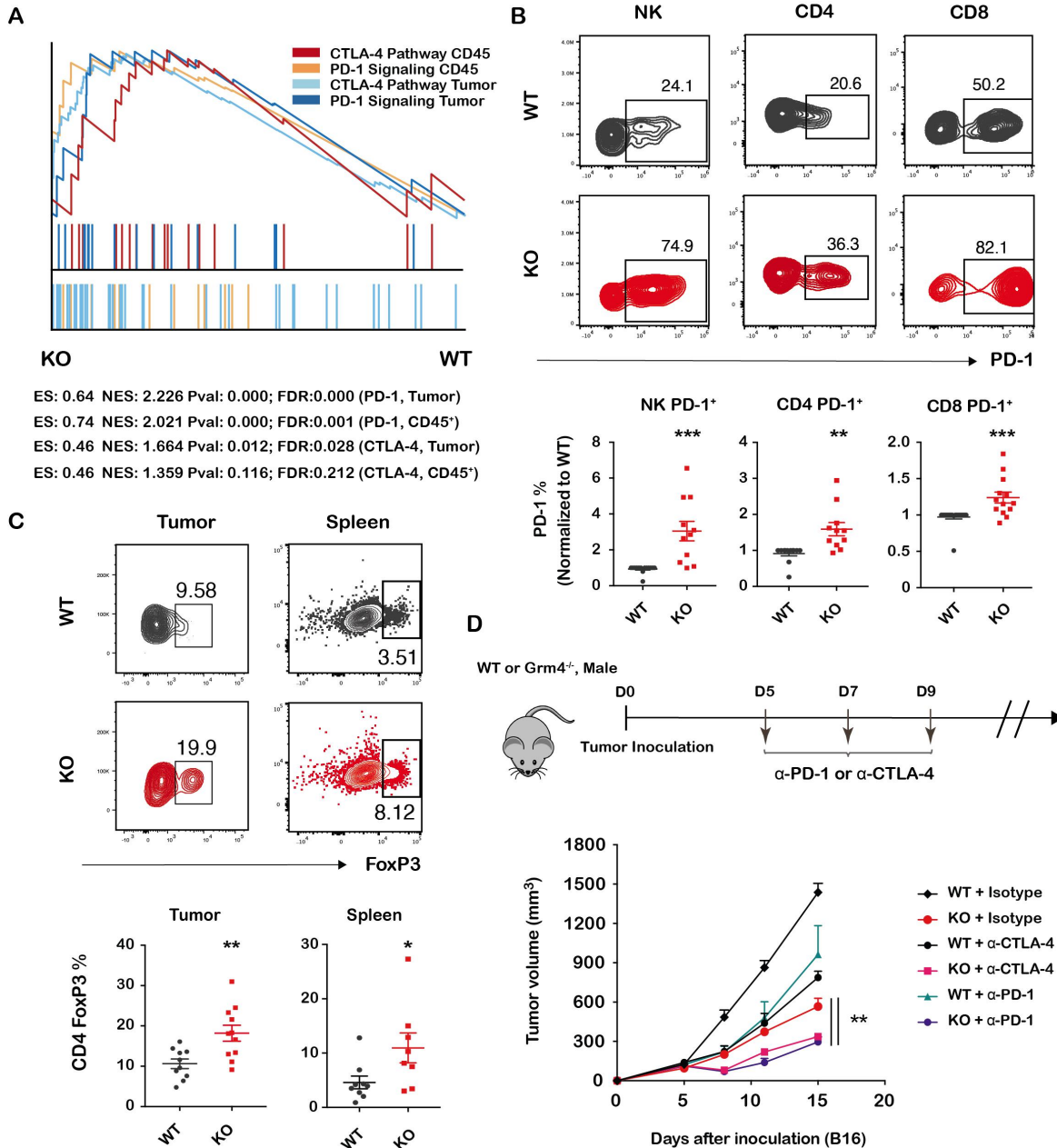


Figure 21 *Grm4* Depletion Induced Adaptive Immune Resistance and Synergized with Immune Checkpoint Inhibitors-based Treatments

(A) GSEA analysis of the PD-1 and CTLA-4 signaling pathways in either B16 tumor tissues or sorted CD45⁺ cells from *Grm4*^{-/-} mice in comparison to WT mice. (B) Representative flow cytometric plots and the quantification of the percentages of PD-1⁺ cells within the gated NK1.1⁺, CD4⁺ T, and CD8⁺ T populations in B16 tumors. (C) Representative flow cytometric plots and the percentages of FoxP3⁺ cells within the gated CD4⁺ T population in

B16 tumors and spleens. (D) The treatment regimen of anti-PD1 and CTLA4 antibodies, and the tumor growth curves in WT and *Grm4*^{-/-} mice. Data shown are representative of three to five experiments.

2.4.8 High-throughput scRNA-Seq identifies the reshaped landscape of tumor infiltrating CD8⁺ T cells

Studies conducted so far were focused on the impact of *Grm4*^{-/-} on the overall changes in NK or CD8⁺ T cells at transcriptional or protein level. Both innate and adaptive immune responses seemingly work together to constitute *Grm4*^{-/-}-mediated anti-tumor immunity, but the adaptive immune system plays a pivotal role in mediating robust and highly specific immune responses against tumors [123]. Therefore, we went to further investigate how *Grm4*^{-/-} modulated the global landscape of tumor-infiltrating CD8⁺ T cells. To address the intrinsic heterogeneity and complex changes within CD8⁺ T cells from *Grm4*^{-/-} and WT mice in an unbiased approach, we used combination approaches of scRNA-seq (10x Genomics) and TCR sequencing (Figure 22).

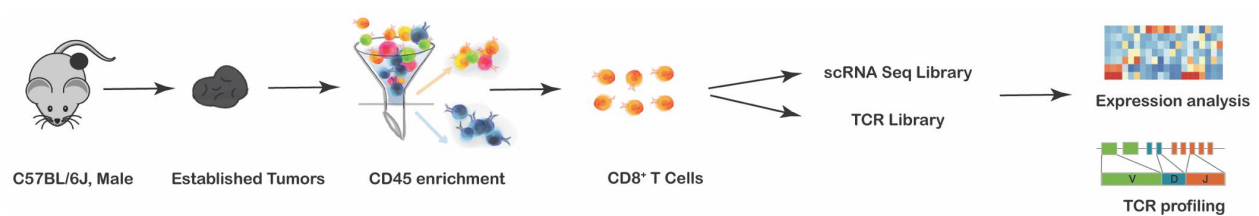


Figure 22 The scheme of the overall study design. Single-cell RNA sequencing was applied to CD8⁺ T cells obtained from B16 tumor tissues, and the output data were used for gene expression analysis and TCR profiling.

We analyzed 3216 single CD8⁺ T cells (1672 WT and 1544 KO) and performed unsupervised clustering of all sequenced CD8⁺ T cells. The CD8⁺ T cells revealed eight distinct clusters based on the gene expression signatures using t-SNE analysis (Figure 23A and Figure 23B). The CD8⁺ T cell marker genes were coded in color for eradicating noise signals (Figure 23C). According to the differentially expressed genes (DEGs), T cell subclusters were designated as CD8-C0-Sell (naïve), CD8-C1-Xcl1 (stem-like) [124, 125], CD8-C2-Ccl5 (tissue-resident memory), CD8-C3-Tigit (exhausted), CD8-C4-Hmgb2 (cycling), CD8-C5-Cdca7 (memory), CD8-C6-Prfl (cytotoxic), and CD8-C7-Itgb1 (superior cytotoxic), with *Grm4*^{+/+} and *Grm4*^{-/-} CD8⁺ T cells showing a distinct distribution across the clusters (Figure 23D and Figure 23E). The proportions of each cluster in either WT or *Grm4*^{-/-} CD8⁺ T cells among either the total CD8⁺ T cells (Figure 23F) or within the total cells in each cluster (Figure 23G) were quantitated.

Of note, ~27% CD8⁺ T cells from the *Grm4*^{+/+} mice were distributed in the cluster of CD8-C0-Sell in comparison with ~19% in *Grm4*^{-/-} mice, indicating that *Grm4*^{-/-} TME potentially primes the differentiation of the naïve CD8⁺ T cells into functional states (Figure 23F). It has been previously recognized that T cells within the TME are prone to exhaustion, thus preventing such CD8⁺ T cells from eliciting sufficient T cell-mediated killing of tumor cells. Focusing our analysis on tumor infiltrating CD8⁺ T cells in the context of B16 melanoma, we observed fewer effector CD8⁺ T cells but a large proportion of T cells with exhausted phenotypes in the TME. As shown in Figure 23F and Figure 23G, the exhausted subcluster CD8-C3-Tigit occupied ~17% CD8⁺ T cells while only ~4.6% and ~3% of CD8⁺ T cells were in the clusters of CD8-C6-Prfl and CD8-C7-Itgb1 in WT mice, respectively. It seems that *Grm4*^{-/-} might maintain the cytotoxic

status and prevent CD8⁺ T cells from entering into an exhausted state because a significant reduction of CD8-C3-Tigit (~9%) was observed in *Grm4*^{-/-} mice. Interestingly, the data from scRNA-seq further defined that *Grm4*^{-/-} selectively increased the cytotoxic CD8⁺ T cells. More than 60% of all cells in the clusters of CD8-C6-Prf1 and CD8-C7-Itgb1 were *Grm4*^{-/-} CD8⁺ T cells (Figure 23G). As a cytotoxic marker of CD8⁺ T cells, Prf1 is predominately accumulated in the subcluster of CD8-C6-Prf1 and partially in CD8-C7-Itgb1. There was a significant increase in the percentage of the subcluster of CD8-C6-Prf1 in *Grm4*^{-/-} mice (~8%) compared to the WT mice (~4.6%) (Figure 23F). Itgb1 (CD29) identifies IFN- γ -producing and marks superior cytotoxic CD8⁺ T cells [126]. As shown in (Figure 23E and Figure 23H), IFN- γ is majorly accumulated in the cluster of CD8-C7-Itgb1. Here, there were approximately 6.5% CD8-C7-Itgb1 in *Grm4*^{-/-} mice vs about 3% in WT mice, indicative of significantly increased (> 2-fold) IFN- γ producing cells after knockout of *Grm4*. In addition, this phenotype is consistent with the increased expression of MKi67 (Ki-67), Cd44, and Tnfsf10 (co-stimulatory molecules) [127] (Figure 23H). Our data from the early study suggest that *Grm4*^{-/-} conditioned CD8⁺ T cells toward an activated and proliferative phenotype at the overall transcriptional and protein levels (Figure 13D and Figure 18). Here, scRNA-seq data defined that *Grm4*^{-/-} preferentially increased the proliferative and activated functionality in the sub-cluster of CD8-C7-Itgb1.

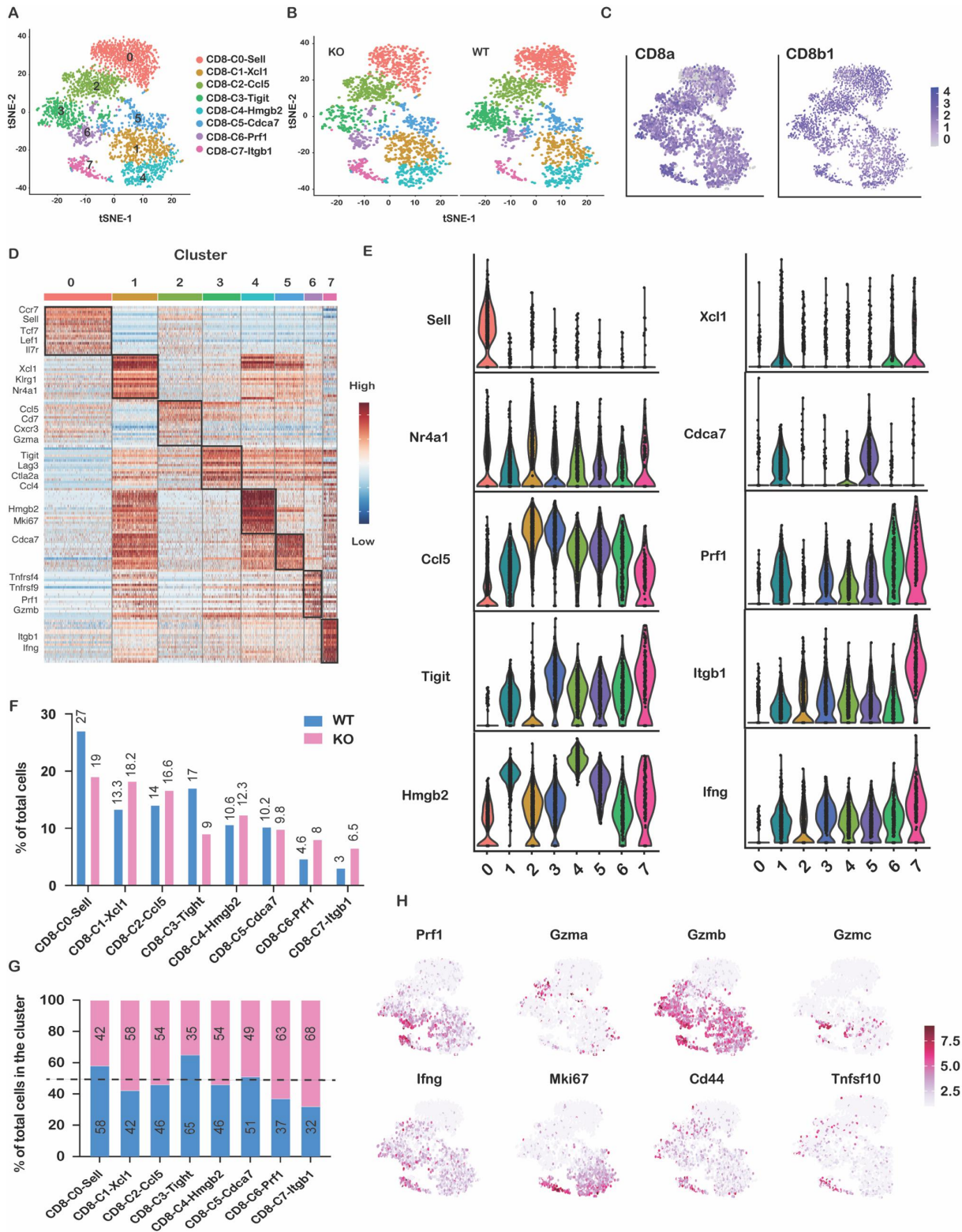


Figure 23 High-Throughput Single-Cell RNA-Seq of Tumor-Infiltrating CD8⁺ T Cells Revealed Distinct Transcriptional Signatures between WT and *Grm4*^{-/-} Mice.

(A-B) The 8 clusters defined from the t-Distribution Stochastic Neighbor Embedding (t-SNE) projection of the total 3216 single T cells from both WT and *Grm4*^{-/-} mice (1672 WT and 1544 *Grm4*^{-/-}) (A) and the CD8⁺ T cells from each strain of mice (B). (C) The color coded for the expression of CD8⁺ T marker genes. (D) Heatmap of the top differentially expressed genes within the eight clusters. (E) Violin plot shows the expression of the top marker genes in each cluster. (F-G) The percentages of WT and *Grm4*^{-/-} CD8⁺ T cells among the total CD8⁺ T cells (F) and within each cluster (G). (H) The expression of selected genes across the tSNE plot. The color keys indicate the gene expression values for maturation markers, activating receptors, cytotoxic effector molecules and effector cytokines, respectively.

Elevated expression of transcripts encoding PD-1 (*Pdcd1*) and CTLA-4 (*Ctla4*), the corresponding T cell inhibitory receptors, were also observed in effector CD8⁺ subsets particularly in CD8-C7-Itgb1 (Figure 24), which is consistent with previous research [128]. These results might be due to the feedback mechanisms: (1) the released IFN- γ can trigger the inducible expression of PD-L1 [129] and CTLA-4 [130], (2) the proliferating subsets are more likely to express receptors PD-1 and CTLA-4 [131]. In melanoma, a higher proportion of Ki67⁺ CD8⁺ T cells was associated with improved response to checkpoint inhibitors, which is consistent with the enhanced tumor growth inhibition in *Grm4*^{-/-} mice treated with immune checkpoint inhibitors (Figure 21D).

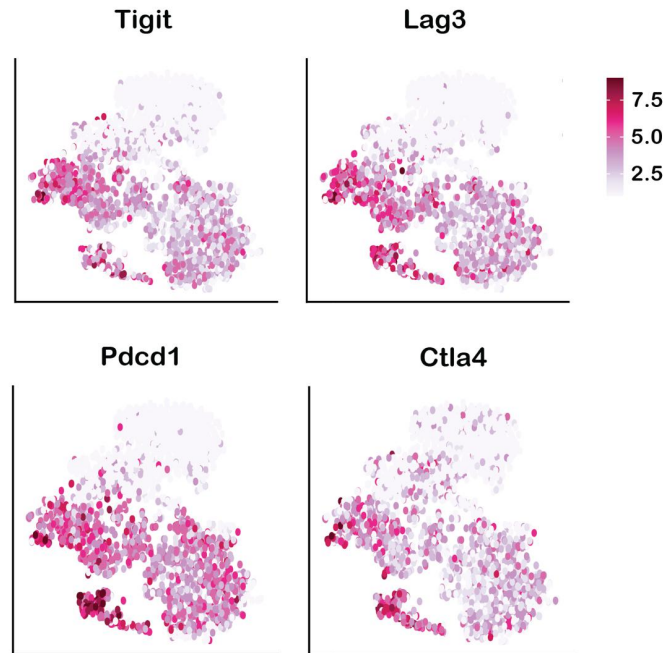


Figure 24 The expression of selected genes across the t-SNE plot. The color keys indicate the gene expression values for exhausted markers and inhibitory receptors.

We also found increased percentages of CD8-C1-Xcl1, CD8-C2-Ccl5, and CD8-C4-Hmgb2 subsets in *Grm4^{-/-}* mice (Figure 23F and Figure 23G). CD8-C1-Xcl1 (stem-like) subsets may also maintain cytotoxic function with increases in the capacity of proliferation, and the expression of *Gzmc* and *Gzmb* (Figure 23H). Expression of *Gzma* is selectively accumulated in CD8-C2-Ccl5 subsets (tissue-resident memory) (Figure 23H). These results indicate that tissue-resident memory CD8⁺ T cells can also maintain their cytotoxic effect. No significant changes were observed in CD8-C5-Cdca7 (memory) subsets between WT and *Grm4^{-/-}* mice (Figure 23F and Figure 23G). Taken together, *Grm4^{-/-}* also increased the stem-like, memory-like, and cycling CD8⁺ T cells in the TME, which also supports the anti-tumor immunity.

2.4.9 ScTCR profiling maps the subset connectivity by pseudotime state and clonal TCRs

The complete transcriptome data along with TCR information for a large number of T cells allowed us to gain insights into the functional states and relationship among these cells. We evaluated TCR repertoires among CD8⁺ T cell subsets. To gain insight into the clonal relationship among individual T cells, we projected top 10 clonally expanded TCR in WT and *Grm4*^{-/-} CD8⁺ T cells (Figure 25A). The presence of a clonally expanded cell population is typically associated with a history of T cell activation. We observed an overall increased clonal expansion in *Grm4*^{-/-} in comparison to WT mice (Figure 25B), indicative of an enhanced responses of T cells to tumor antigens [132, 133]. Especially, there were more clonally expanded TCRs in the clusters of CD8-C1-Xcl1, CD8-C6-Prf1, and CD8-C7-Itgb1 in *Grm4*^{-/-} mice compared to WT control, consistent with the notion that large and expanded T-cell clones have activated phenotypes [134]. Our data are consistent with the observations of Gutierrez et al. that naïve or central memory CD8⁺ T cells show minimal clonal expansion, while effector CD8⁺ T cells, proliferating CD8⁺ T cells, and terminal effector CD8⁺ T cells show higher levels of expansion [135]. Interestingly, contrary to what was seen in *Grm4*^{-/-} mice, more clonally expanded TCR was selectively concentrated within the CD8-C3-Tigit in WT mice (Figure 25A and Figure 25C). This might be due to that CD8-C3-Tigit is a group of effector cells that entered the exhausted status at the early developmental stage.

Similar TCR analysis painted a different picture for the origins of tumor-infiltrating CD8⁺ T cells in *Grm4*^{-/-} vs WT TME. There are large numbers of shared T cell clones among CD8⁺ T cells in either WT or *Grm4*^{-/-}, suggesting that CD8⁺ T cells of different clusters were not completely independent but might undergo state transitions (Figure 25D). These findings were

also independently validated by clonal analysis based on those identical TCRs from common ancestors but falling into different cell clusters (Figure 25E). We projected two representative projections of shared clone types in WT and *Grm4*^{-/-}. The vast majority of shared clone types in WT are accumulated in the CD8-C3-Tigit. However, shared clones were more evenly distributed in the *Grm4*^{-/-} CD8⁺ T cells and barely found in the exhausted state, which infers that the state changes that occurs in the *Grm4*^{-/-} mice is majorly on effector CD8⁺ T cells.

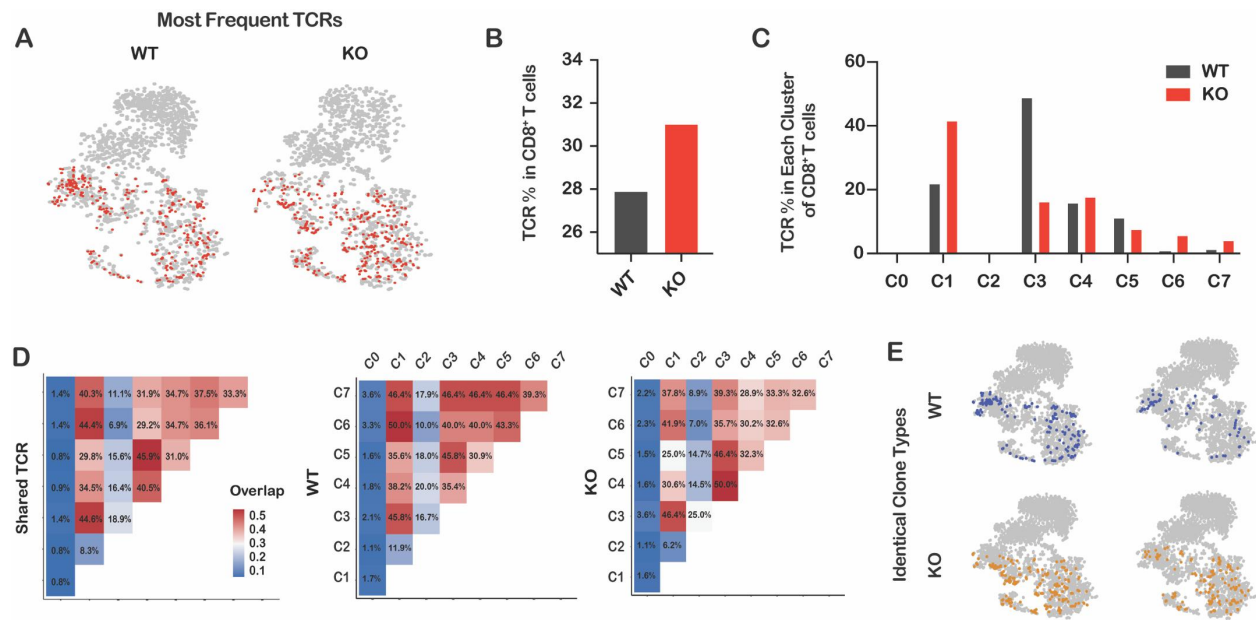


Figure 25 High-Throughput Single-Cell TCR-Seq of Tumor-Infiltrating CD8⁺ T Cells Revealed Distinct Difference.

(A) Projection of the top 10 frequent TCR (red dots) to clusters of CD8⁺ T cells. (B-C) Quantification of total highly expanded TCR (B) and in each cluster (C). (D) The shared TCR among different clusters. (E) Projection of identical clone types (two representative clone types either in WT or *Grm4*^{-/-} are shown).

We then applied the Monocle 3 algorithm [136] to analyze CD8⁺ T cells in pseudo-time to indicate their developmental trajectories in WT and *Grm4*^{-/-} CD8⁺ T cells respectively (Figure 26A- B). Such pseudo-time analysis is a measure of progress through biological progresses based

on transcriptional similarities. Eight clusters formed into a relative process in pseudo-time that began with the CD8-C0-Sell (naïve CD8⁺ T cells). CD8-C2-Ccl15 appeared to be an intermediate state based on such trajectory analysis in both WT and *Grm4*^{-/-} mice. In general, both WT and *Grm4*^{-/-} CD8⁺ T cells ended with C7-CD8-Itgb1 (the highest activated cluster) or CD8-C3-Tigit (exhausted CD8⁺ T cells), demonstrating the two directions for T cell state transition, which is consistent with previous studies [137]. In the WT CD8⁺ T cells, there are some overlap with CD8-C3-Tigit through the biological progress to C7-CD8-Itgb1 (Figure 26A), which might represent the tumor-induced T cell exhaustion in melanoma TME [138]. However, CD8-C3-Tigit is in an independent branched structure after *Grm4*^{-/-} as well as CD8-C6-Prf1 (Figure 26B), suggesting that *Grm4*^{-/-} has a global impact on the biological progresses of CD8⁺ T developmental trajectories and can bypass the pre-exhausted status.

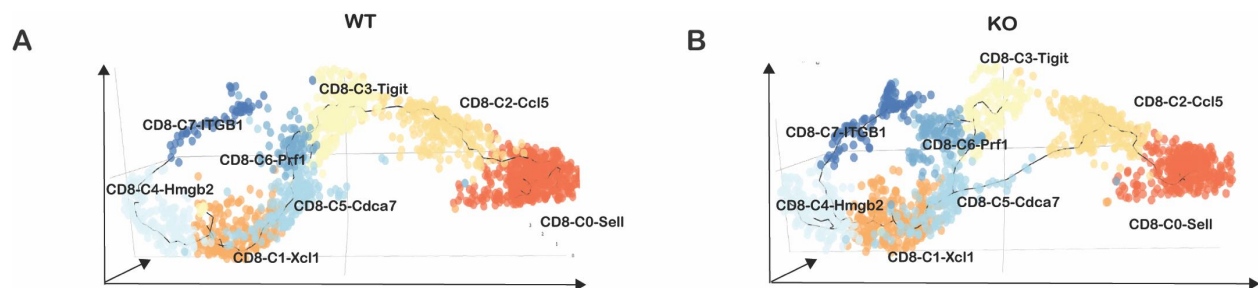


Figure 26 The ordering of CD8⁺ T cells along pseudotime in a three-dimensional state-space defined by Monocle 3.

Cell orders are inferred from the expression of most dispersed genes across CD8⁺ T cell populations sans MAIT.

Each point corresponds to a single cell, and each color represents a CD8⁺ T cell subcluster.

In our early study, we also observed an increased recruitment of tumor infiltrating CD4⁺ T cells and their activated phenotype, which shall indirectly contribute to the anti-tumor immunity. We performed scRNA-seq for isolated CD4⁺ T cells as well (Figure 27) and identified five CD4⁺ T cell clusters (Figure 27A). Cells from the largest cluster, CD4-C0-Itgb1, expressed Th1 marker genes like *Cxcr3*, *Ifng*, and *Ccl5* (Figure 27B). In addition, we found that C4-C1-Ccr7 had higher expression of naïve/stem T cell marker genes like *Ccr7* and *Sell* (Figure 27B). Overall, there were fewer naïve CD4⁺ T cells and more CD4-C0-Itgb1 (Figure 27C- D). It is noted that *Cd44*, *Ifng*, and *MKi67* were selectively accumulated in CD4-C0-Itgb1, indicating that *Grm4*^{-/-} also selectively increased Th1 cells (Figure 27E). However, these changes are less dramatic in comparison to CD8⁺ T cells. Overall, there were fewer genes affected as well as smaller changes in the levels of gene expression in the single-cell RNA-Seq of CD4⁺ T cells (Figure 27F), which is different from a more dramatic changes in Th response in *Grm4*^{-/-} mice in an EAE model [33]. This suggests a complex and context-dependent role of GRM4 in immune modulation.

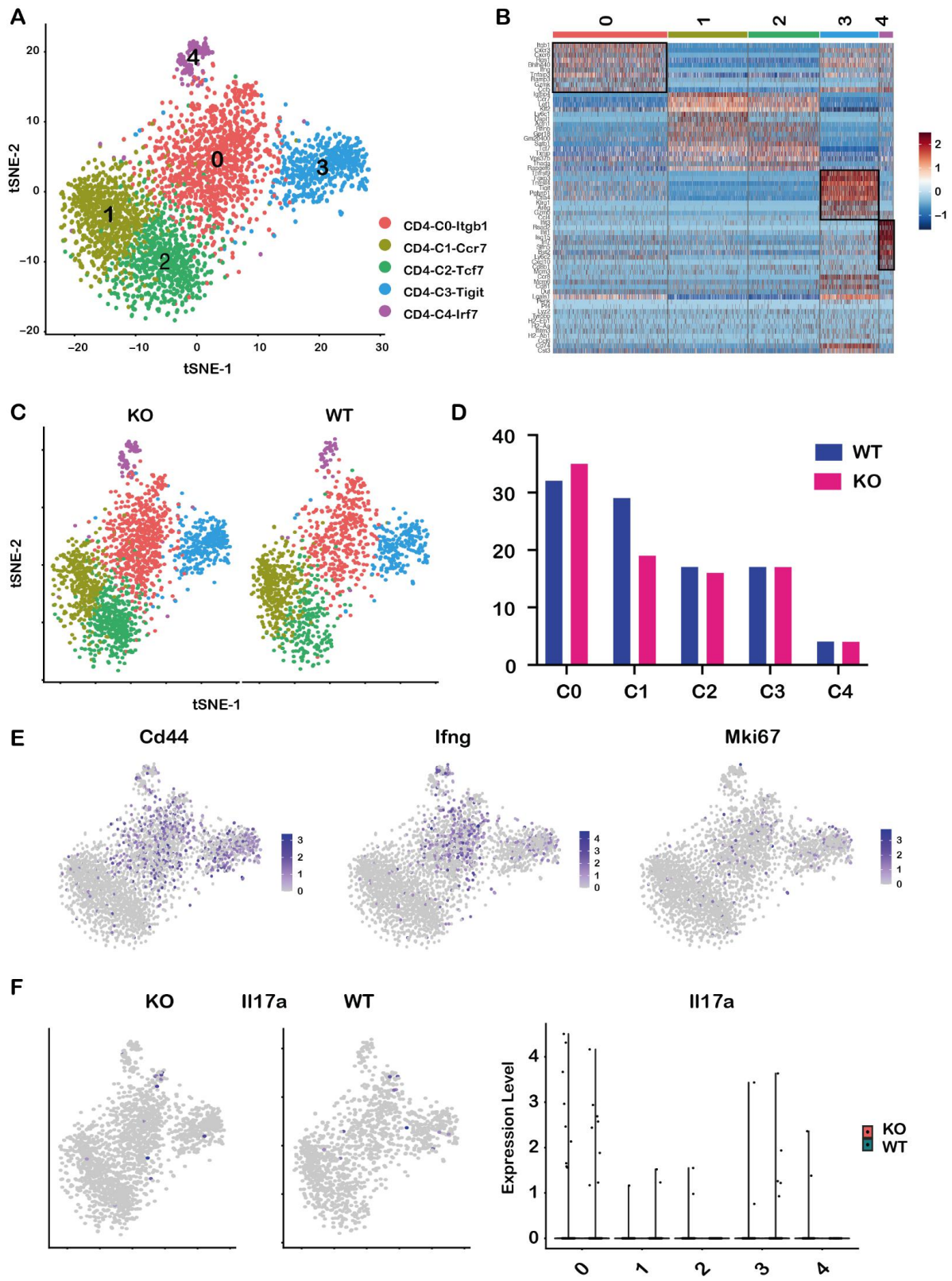


Figure 27 High-Throughput Single-Cell RNA-Seq of Tumor-Infiltrating CD4⁺ T Cells

(A) The 5 clusters defined from the t-SNE of the total CD4⁺ T cells from both WT and *Grm4*^{-/-} mice. (B) Heatmap of the top differentially expressed genes within the eight clusters. (C) Projection of CD4⁺ T cells from WT and *Grm4*^{-/-} mice separately. (D) Percentages of WT and *Grm4*^{-/-} CD4⁺ T cells among total CD4⁺ T cells. (E) The expression of selected genes across the t-SNE plot. The color keys indicate the gene expression values for *Cd44*, *Ifng*, and *Mki67*. (F) The projection and violin plot of *Il17a* in CD4⁺ T cells either isolated from WT or *Grm4*^{-/-} mice in each cluster.

2.4.10 GRM4/cAMP/CREB signaling modulates the function of NK and CD8⁺ T cells

To test whether CD8⁺ T cells can be directly modulated by GRM4, we sought to model antigen stimulation *in vitro*. CD8⁺ T cells were isolated from the spleen and lymph node of *Grm4*^{-/-} and WT naïve mice and activated with plate-bound anti-CD3 plus anti-CD28 (Figure 49), followed by culturing in the presence of IL-2-containing RPMI medium for 5 days [139].

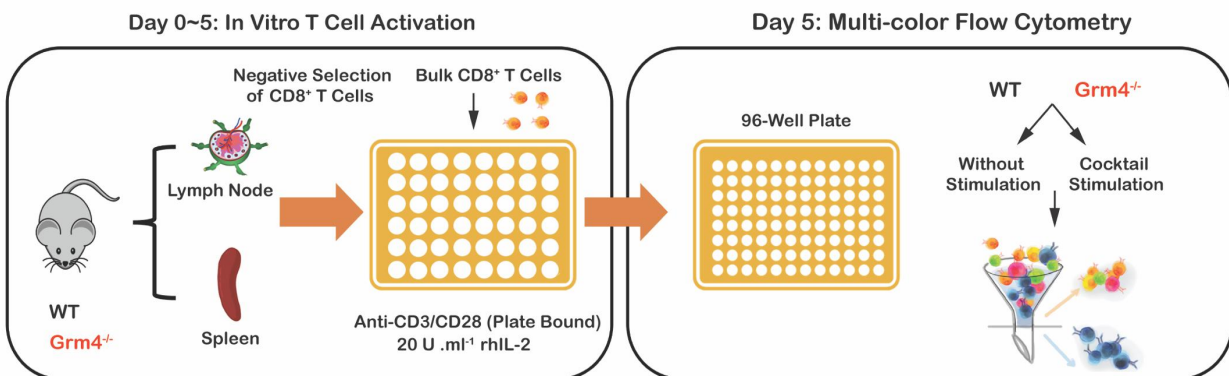


Figure 28 The experimental scheme for isolation, *in vitro* culture, and *in vitro* stimulation of CD8⁺ T cells, and the subsequent flow cytometry analysis.

Then, the medium of cultured CD8⁺ T cells was replaced with stimulation cocktail and the IFN- γ production was measured by flow cytometry. *Grm4*^{-/-} CD8⁺ T cells produced significantly more IFN- γ compared to the WT CD8⁺ T cells (Figure 48A). In addition, we adoptively transferred *Grm4*-deficient CD8⁺ T cells into the RAG-1 deficient mice that lack mature T cells and B cells, prior to B16 inoculation [140]. This led to reduced tumor growth compared with mice receiving CD8⁺ T cells isolated from WT mice (Figure 48B), indicative of a cell-intrinsic role of GRM4 in regulating the antitumor activity of CD8⁺ T cells.

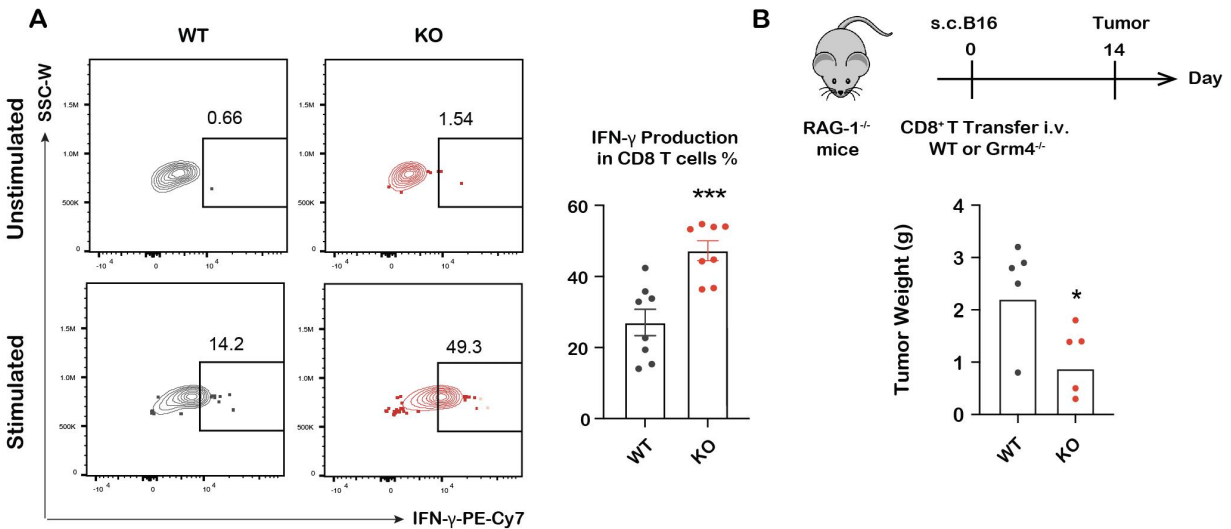


Figure 29 The Enhanced Anti-tumor Activity and IFN- γ Production of Stimulated *Grm4*^{-/-} CD8⁺ T Cells.

(A) The representative flow cytometric plots and the quantitative data showing the IFN- γ production in CD8⁺ T cells isolated with from WT or *Grm4*^{-/-} mice. (B) The growth of s.c. B16 tumors in *RAG-1*^{-/-} mice receiving CD8⁺ T cells isolated either from WT (n=5) or *Grm4*^{-/-} mice (n=5).

We then similarly cultured isolated NK cells in the presence of IL-2 for 7 days (Figure 30A). Again, *Grm4*^{-/-} NK cells produced significantly more IFN- γ compared to the WT NK cells

(Figure 30B). These data suggest that GRM4 is capable of directly modulating the function of NK and CD8⁺ T cells and knockout of *Grm4* led to enhanced function of NK and CD8⁺ T cells.

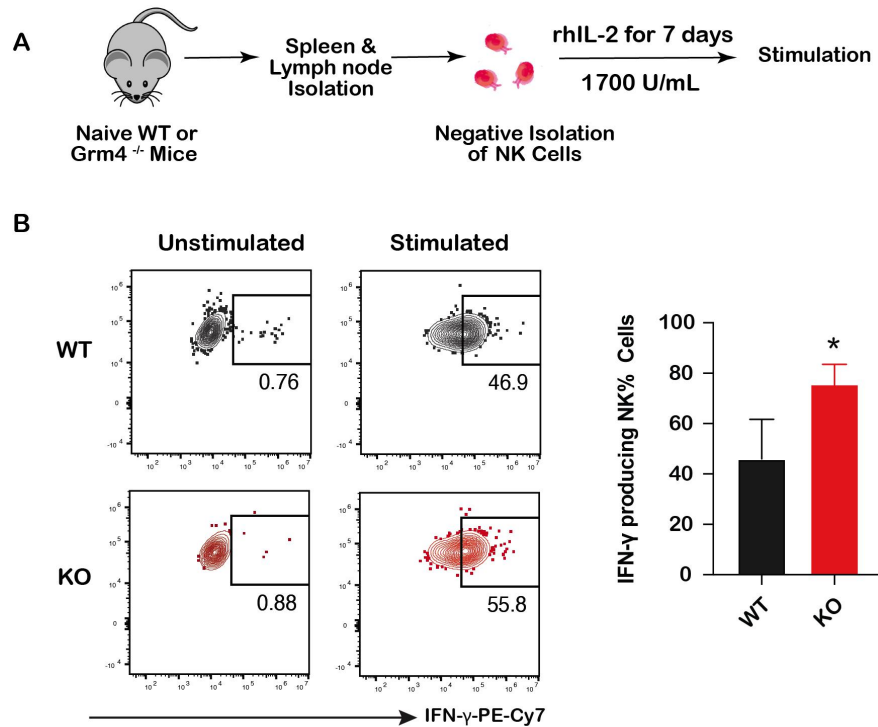


Figure 30 NK Cells Contributed to the *Grm4*^{-/-}-mediated Anti-tumor Effect and Enhanced IFN-γ Production.

(A) Experimental scheme for *in vitro* stimulation of NK cells. (B) Representative flow cytometric plots and the quantitative data showing the IFN-γ production in NK cells.

The mechanism for the enhanced function of NK and CD8⁺ T cells after *Grm4*^{-/-} is unclear. GRM4 has been shown to negatively regulate intracellular cAMP levels in a Gi protein-dependent fashion in presynaptic nerve terminals and microglia as well as in DCs [33, 141]. Indeed, RNA-seq results demonstrated significantly upregulated cAMP signaling pathway after *Grm4*^{-/-} in the isolated CD45⁺ (Figure 31).

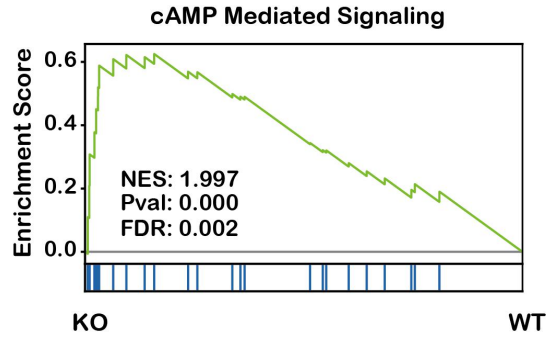


Figure 31 GSEA plot of upregulated cAMP signaling pathway in isolated *Grm4*^{-/-} CD45⁺ cells in comparison to WT.

As an initial step to gain the mechanistic insights into how GRM4 regulates cAMP signaling, we measured the cAMP concentration in naïve CD8⁺ T cells isolated from the spleens and lymph node of *Grm4*^{-/-} and WT mice. There was an increasing trend in the basal levels of cAMP in *Grm4*^{-/-} CD8⁺ T cells compared to WT cells. However, in the presence of forskolin (an activator of adenylyl cyclase), the intracellular concentration of cAMP was significantly higher in *Grm4*^{-/-} CD8⁺ T cells than that in WT CD8⁺ T cells (Figure 32A), suggesting a role of GRM4 in controlling the intracellular cAMP concentration.

The cAMP response element binding protein (CREB) is one of the transcriptional factors that positively regulate the expression of IFN- γ [142, 143]. (Figure 32B and Figure 32C) shows that the levels of phosphorylated CREB (pCreb) in *Grm4*^{-/-} CD8⁺ T cells were significantly increased. Along with these changes, we also observed a significant increase in the expression level of IFNGR1 (Figure 32D), which is very important for the initiation of IFN- γ signaling.

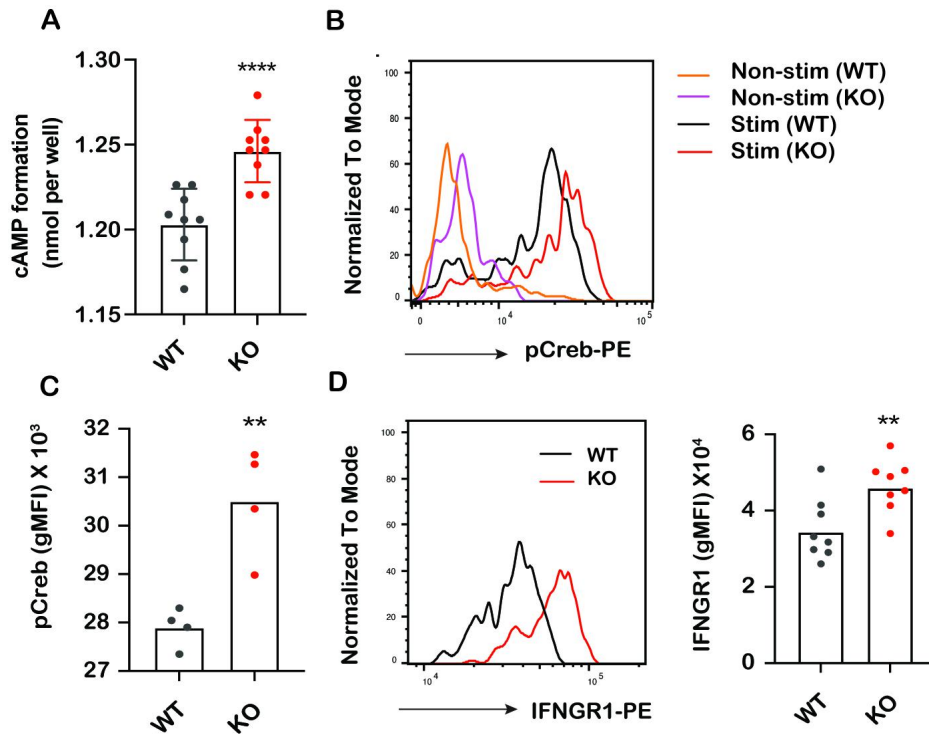


Figure 32 The Enhanced Anti-tumor Activity and IFN- γ Production of Stimulated *Grm4*^{-/-} CD8⁺ T Cells Was Correlated with Activation of cAMP-CREB-Immune Pathway

Interestingly, scRNA-Seq revealed enhanced PKA/CREB signaling in *Grm4*^{-/-} CD8⁺ T cells (Figure 33A). In addition, the expression of *Creb1* (encoding CREB) is positively correlated with those of *Ifng* (encoding IFN- γ) and *Ifngr1* in either WT or *Grm4*^{-/-} tumor infiltrating CD8⁺ T cells (Figure 33B). It is worthwhile to mention that a better correlation was seen in *Grm4*^{-/-} CD8⁺ T cells. Taken together, we propose that GRM4/cAMP/CREB pathway may play a role in the direct activation of CD8⁺ T cells (Figure 33C).

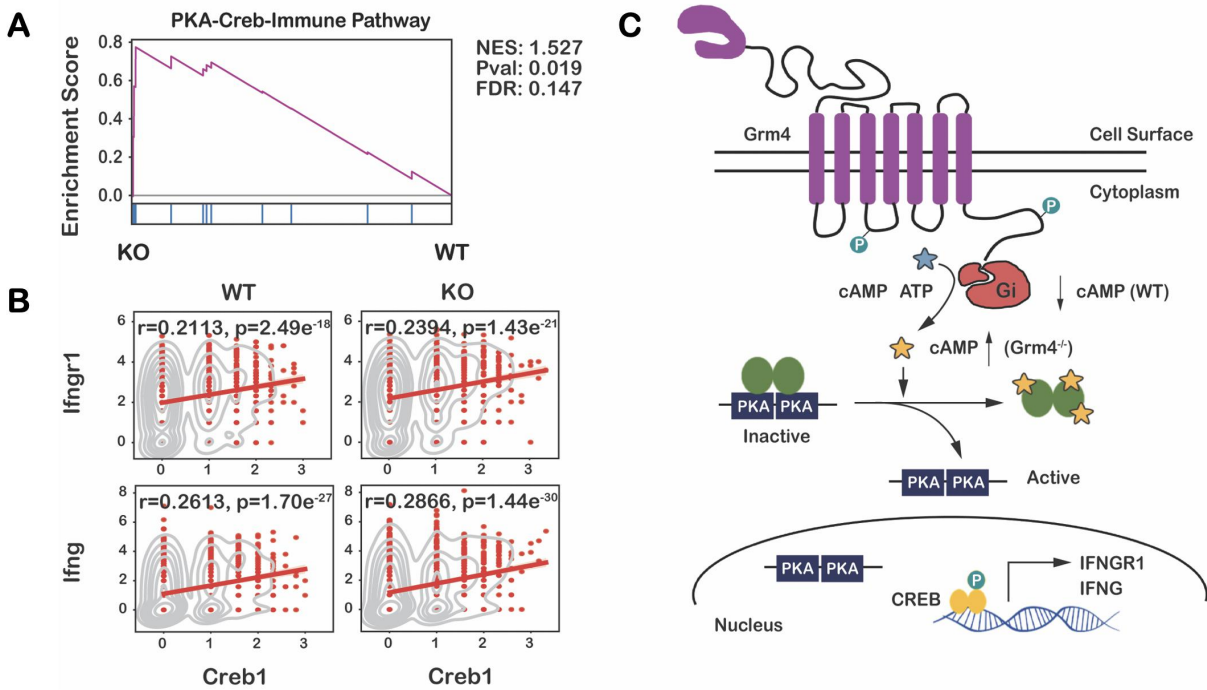


Figure 33 The Enhanced Anti-tumor Activity of Stimulated *Grm4*^{-/-} CD8⁺ T Cells Was Correlated with Activation of cAMP-CREB-Immune Pathway.

(A) GSEA plots of upregulated cAMP-CREB pathway from single RNA-Seq results of CD8⁺ T cells isolated from *Grm4*^{-/-} mice in comparison to WT mice. (B) Correlation of *Creb1* with *Ifngr1* and *Ifng* in either WT or *Grm4* KO tumor-infiltrating CD8⁺ T cells. (C) Proposed mechanism of GRM4-mediated cAMP-CREB Pathway.

2.4.11 Pharmacological inhibition of GRM4 significantly delays tumor growth

Our data so far have clearly demonstrated that genetic knockout of *Grm4* led to an immune-active TME, which plays an important role in inhibiting the growth of transplanted tumors. We then went to study whether similar outcome could be achieved via pharmacological inhibition using MSOP, a GRM4 antagonist [144]. C57BL/6 mice bearing B16, MC38 or 3LL tumors (~50 mm³) received daily i.v. injection of MSOP (10 mg/kg) for 10 days and tumor growth was monitored once every three days (Figure 34A). MSOP treatment led to significant

inhibition of tumor growth in male mice for all three tumor models (Figure 34B-D, Figure 35E-G). In addition, the inhibitory effect of MSOP on B16 tumor was abolished in *Grm4*^{-/-} mice (Figure 34E and Figure 35H), suggesting that the MSOP-mediated tumor growth inhibition is dependent on targeting of GRM4.

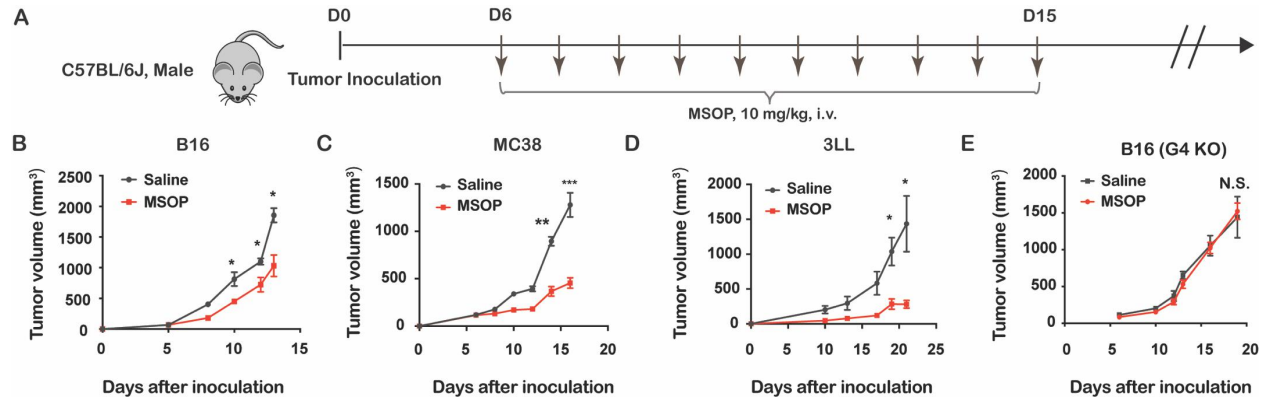


Figure 34 Pharmacological Inhibition of GRM4 with MSOP Significantly Delayed Tumor Growth

(A-E) The *in vivo* antitumor activity of MSOP was tested in 3 cancer types (B16, MC38, and 3LL). MSOP was given to WT (B-D) and *Grm4*^{-/-} mice (E) i.v. daily for 10 days at a dosage of 10 mg/kg starting from day 6 and the tumor growth was followed every two days.

Similar to what was observed in the genetic model, there was no significant difference in the growth of B16 or 3LL tumor between MSOP treatment group and control group (saline) in female mice (Figure 35A-D).

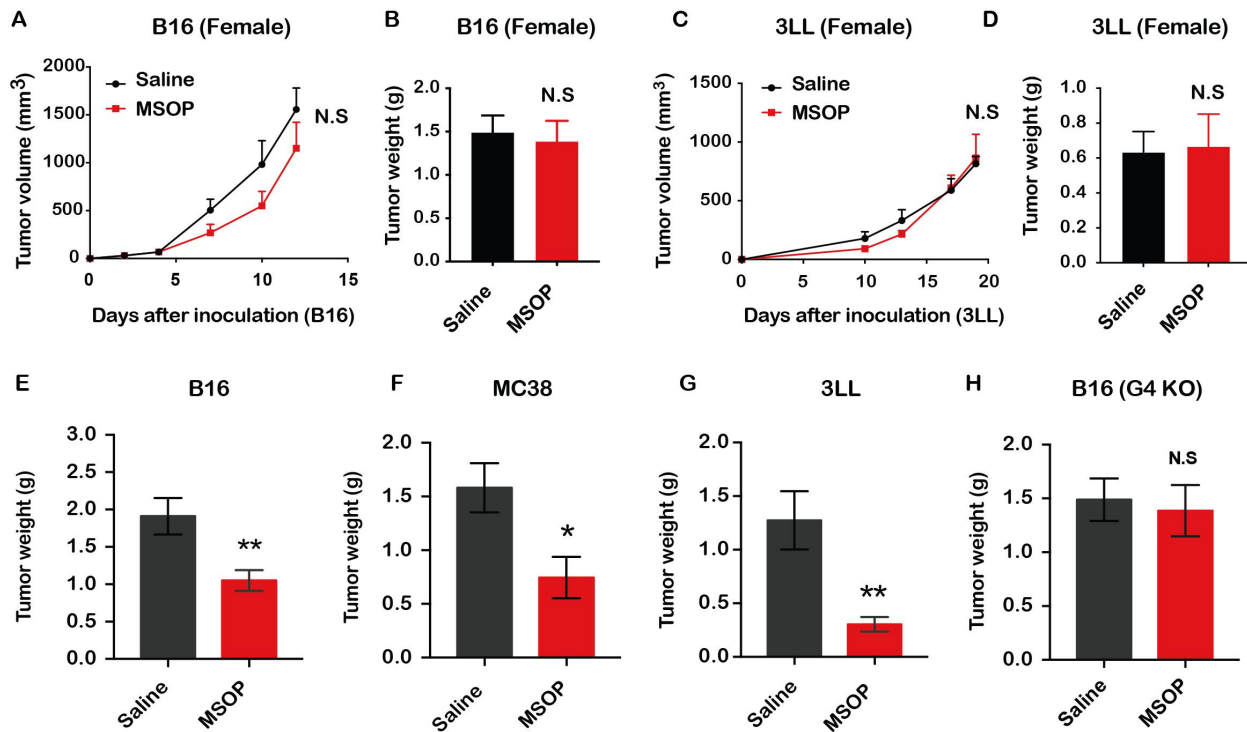


Figure 35 Pharmacological Inhibition of GRM4 with MSOP Does not Delay Tumor Growth in Female Mice.

(A-D) The *in vivo* antitumor activity of MSOP was tested in two cancer types (B16 and 3LL) in female mice. The tumor growth was followed every two days and tumor weight was measured at the endpoint. (E-H) The *in vivo* antitumor activity of MSOP was tested in three cancer types (B16, MC38, and 3LL) in male mice (n=5~8). MSOP was given to WT (E-G) and *Grm4*^{-/-} (H) mice i.v. daily for 10 days at a dosage of 10 mg/kg starting from Day 6 and the tumor weight was measured at the endpoint.

Pharmacological inhibition of GRM1 has been shown to cause inhibition of tumor cell proliferation both *in vitro* and *in vivo* [145]. To evaluate whether targeting of GRM4 by MSOP has a direct impact on cancer cells, cultured B16, MC38 or 3LL tumor cells were treated with various concentrations of MSOP and the cytotoxicity was examined by MTT assay. Riluzole, a GRM1 antagonist, was used as a positive control. In consistent with previous studies [46, 145], riluzole inhibited the proliferation of B16 melanoma cells in a concentration dependent manner (Figure 36A and Figure 36D). However, MSOP did not show obvious inhibitory effect at all

concentrations used, even at a concentration as high as 500 μM . Similar results were observed in two other murine cancer cell lines MC38 (Figure 36B and Figure 36E) and 3LL (Figure 36C and Figure 36F). Lack of effect on the proliferation of the three cancer cell lines was also shown with MAP-4, another GRM4 antagonist [48]. These data, together with the data from the genetic model suggest that MSOP inhibits the tumor growth through modulating the antitumor immunity rather a direct inhibitory effect on tumor cells.

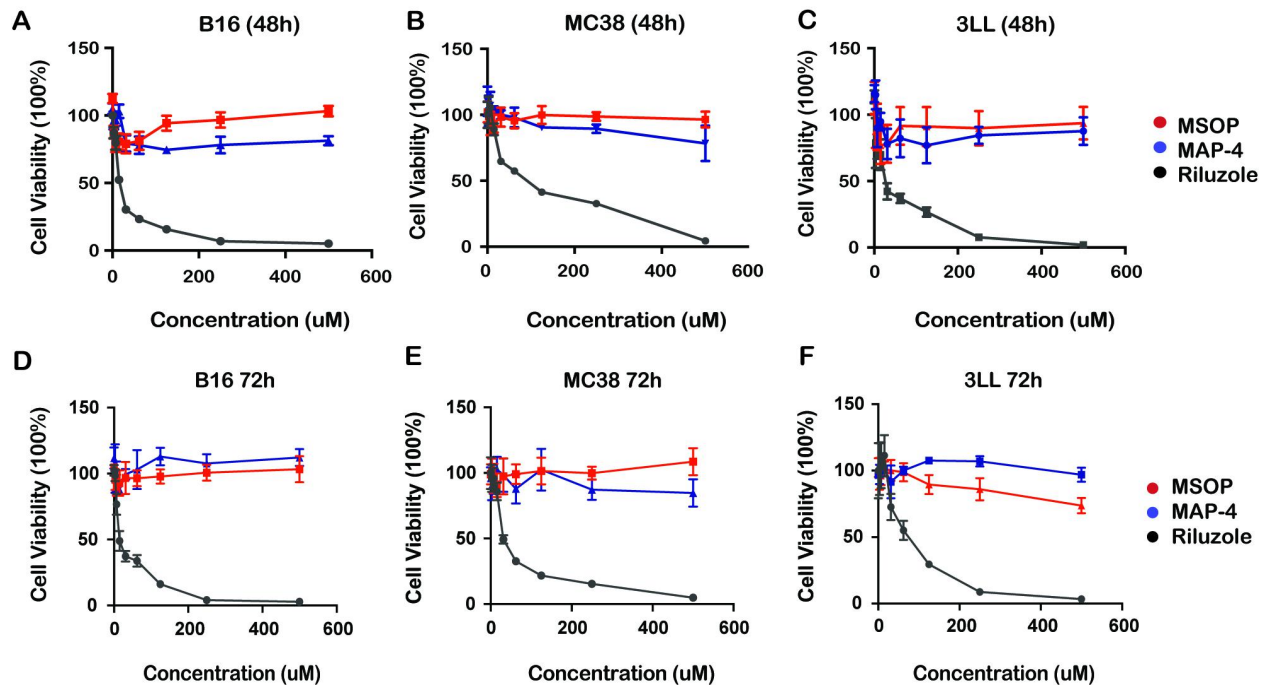


Figure 36 MTT Assay of Riluzole (GRM1 antagonist), MSOP, and MAP-4 (GRM4 antagonist) Against Cultured B16, MC38, and 3LL Cancer Cells.

Cytotoxicity of riluzole (GRM1 antagonist), MSOP, and MAP-4 (GRM4 antagonist) against cultured B16, MC38, and 3LL cancer cells. Cells were treated for 48 and 72 hours and cytotoxicity was determined by MTT assay (n=5).

Figure 37A shows that the numbers of tumor infiltrating CD45⁺ cells were significantly increased following MSOP treatment in B16 tumor model. In particular, MSOP treatment led to significant increases in the numbers of NK cells, CD4⁺ T cells and CD8⁺ T cells (Figure 37B). To define the immune effector molecules involved in the MSOP-mediated antitumor activity, we conducted a preliminary study to examine the therapeutic effect of MSOP in *IFN- γ* ^{-/-} mice. As shown in Figure 37C, the inhibitory effect of MSOP on tumor growth was significantly attenuated in *IFN- γ* ^{-/-} mice compared to WT mice, suggesting that IFN- γ is critically involved in the MSOP-mediated antitumor immunity.

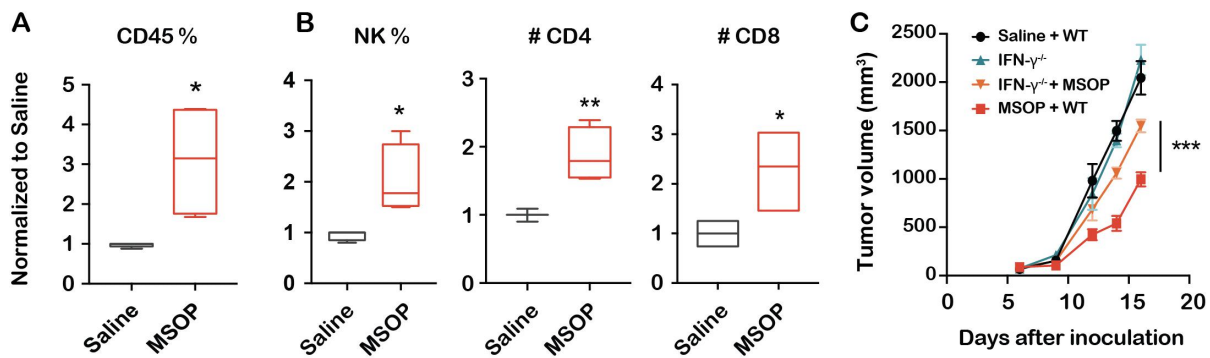


Figure 37 MSOP Mediated Anti-tumor Immunity is Dependent on IFN- γ .

(A-B) Flow cytometry analysis and quantification of the tumor infiltrating lymphocytes after MSOP treatments (n=3). MSOP was i.v. injected daily for 5 days. (C) The antitumor activity of MSOP in WT and *IFN- γ* ^{-/-} mice (n = 5).

We also observed upregulated expression of PD-1 in NK and CD8⁺ T cells in the TME and increased number of FoxP3⁺ CD4⁺ T cells in spleen (Figure 38A- Figure 38B).

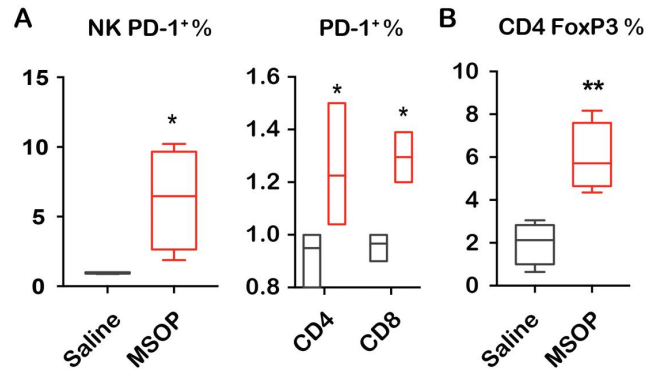


Figure 38 Flow Cytometry Analysis and the Quantification of PD-1⁺ NK, CD4⁺ T, and CD8⁺ T cells, and Treg cells after MSOP treatments.

We then went to investigate whether MSOP could synergize with ICB to improve the therapeutic efficacy (Figure 39A). (Figure 39B- Figure 39D) show that anti-PD-1 or anti-CTLA-4 monotherapy had only moderate effect on B16 tumor, which was consistent with literature [146, 147]. In contrast, combination of MSOP with either anti-PD-1 (Figure 39B and Figure 39D) or anti-CTLA-4 (Figure 39C and Figure 39D) led to drastic inhibition of tumor growth. Overall, our data with pharmacological inhibition of GRM4 are consistent with the data from the genetic knockout model, further establishing a role of GRM4 in immune cells in modulating the antitumor immunity. It also suggests a new therapy based on the use of GRM4 antagonist, alone or in combination with ICB.

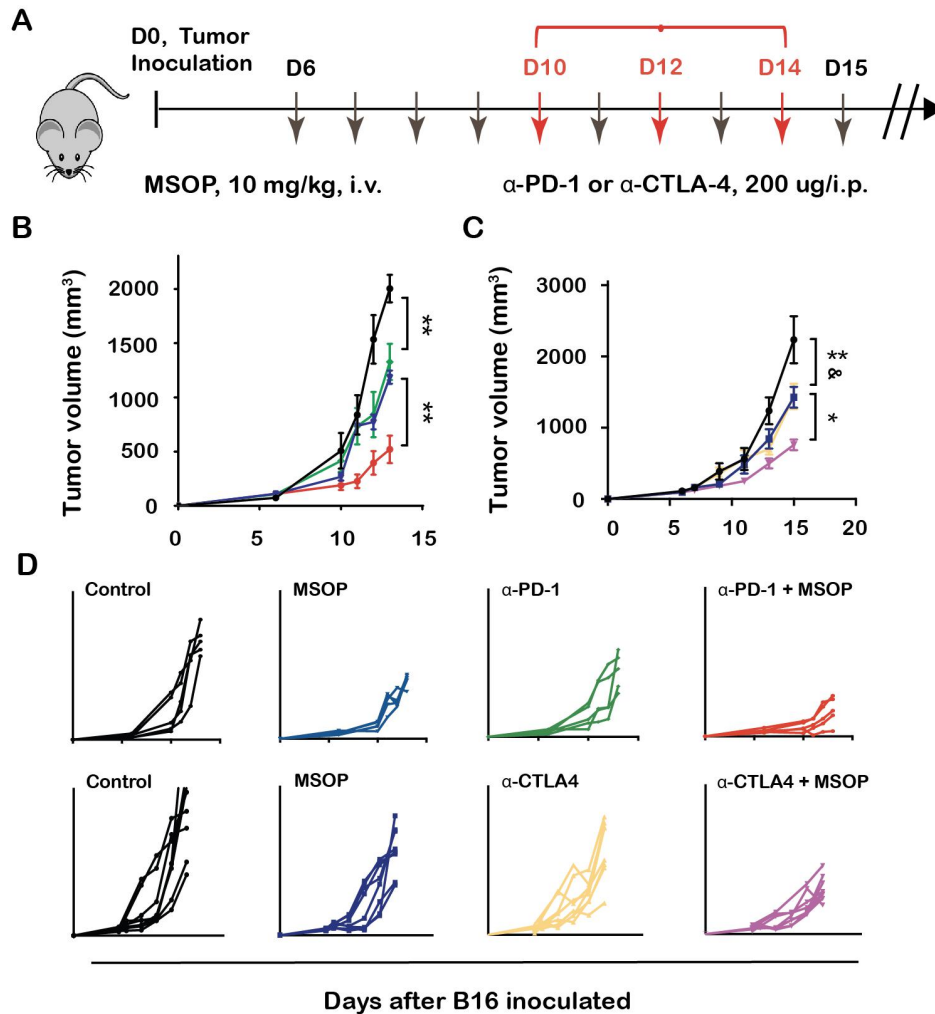


Figure 39 MSOP Synergize with Immune Checkpoint Inhibitors.

(A) The treatment regimen for the combination of MSOP with either anti-PD1 (B) or anti-CTLA4 (C) antibody in B16-bearing mice. C57BL/6J mice bearing established tumors were treated with MSOP at 10 mg/kg for 4 days, and then anti-PD-1, anti-CTLA-4, or IgG isotype control three times once every 2 days. Both average tumor growth and individual tumor growth trajectories were presented (D).

2.4.12 MSOP calcium phosphate nanoparticles significantly improve the anti-tumor effect

Despite the demonstrated antitumor activity of MSOP, frequent dosing is needed due to its rapid elimination following systemic administration. As a highly polar compound, oral dosing is not effective due to its limited bioavailability [148]. Systemic delivery of MSOP using nanoparticles (NPs) can not only increase its half-life in blood but also facilitate enhanced delivery to tumors. In addition, the non-specific uptake of NPs by reticuloendothelial system (RES) shall benefit the delivery to immune cells-enriched spleen. As MSOP bears a phosphate group (ionic group), calcium phosphate NPs represent a simple and highly effective system to improve its *in vivo* delivery.

(Figure 40A-Figure 40B, Figure 41A) shows the scheme for the preparation of MSOP NPs. Mixing of calcium chloride with MSOP led to the formation of MSOP nanocrystals with slightly excess negative charges that facilitates the next step of coating of a lipid layer through interaction with positively charged DOPA. Further incorporation of additional lipids including DOPC and DSPE-PEG led to the formation of MSOP NPs.

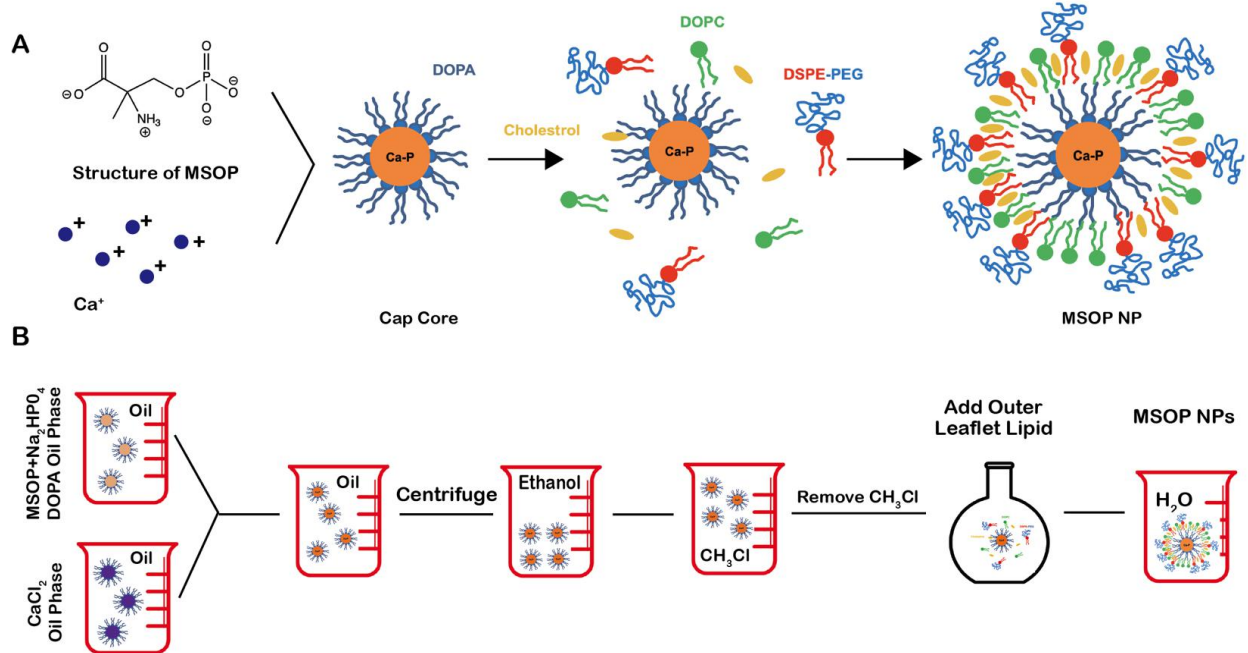


Figure 40 Design and Fabrication of MSOP-loaded Cap Nanoparticles.

(A) Schematic presentation of the design and fabrication of MSOP-loaded Cap nanoparticles (NPs). (B) Illustration of the steps involved in the preparation of MSOP NPs.

The MSOP NPs were homogenous and spherical in shape, as shown in the TEM micrograph (Figure 41B). The average size of the MSOP NPs was ~150 nm (Figure 41C) and the surface zeta potential was ~-2.8 mV (Figure 41C).

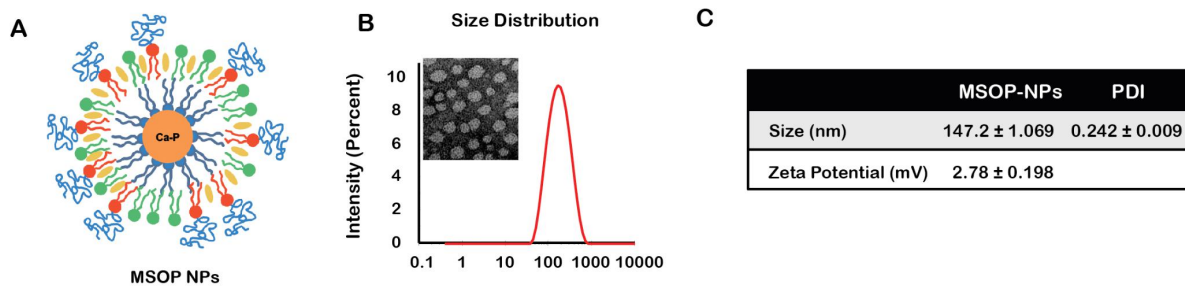


Figure 41 Characterization of MSOP Cap NPs.

(A) Structure of MSOP Cap NPs. (B-C) Representative TEM image, size, and zeta potential of MSOP Cap NPs.

(Figure 42A- Figure 42B) shows that i.v. injection of MSOP NPs three times once every three days led to a significant inhibition of tumor growth in a B16 tumor model. In contrast, injection of free MSOP following the same treatment regimen was not effective.

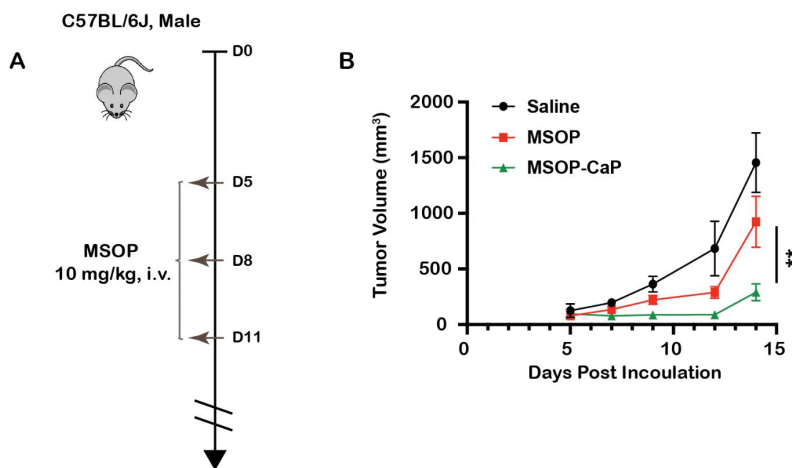


Figure 42 In Vivo Efficacy of MSOP Cap NPs.

Treatment schedule and average tumor growth curves of B16-bearing male mice treated with free MSOP and MSOP NPs, respectively (n = 5). Data shown are representative of two independent experiments. Graphs shown represent data summarized as means \pm S.E.M and were analyzed by unpaired two-tailed unpaired Student's T-test. Two-way ANOVA was used to determine statistical significance for time points when all mice were viable for tumor measurement (n = 5-8 per group). *p < 0.05, **p < 0.01, ***p < 0.001, ****p < 0.0001.

The mice were well tolerated at the dose used without any obvious changes in body weights (Figure 43).

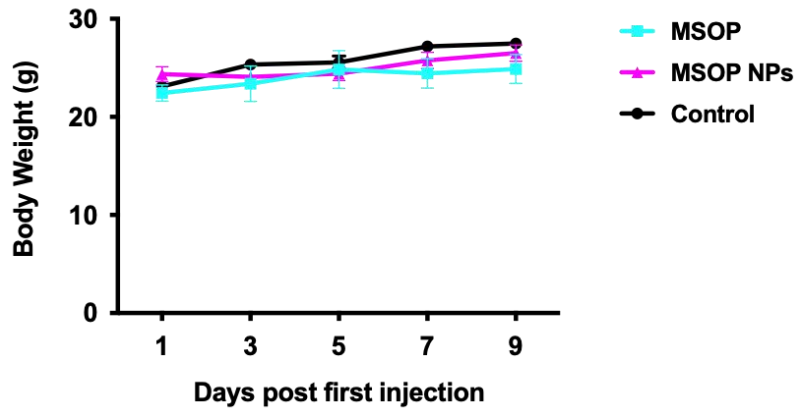


Figure 43 Changes in Body Weights after MSOP-NP Treatments.

B16 tumor-bearing mice were treated with free MSOP or MSOP NPs as described in **Figure 42B** and their body weights were followed once every two days.

In addition, treatments with MSOP NPs had no effect on bone marrow, liver, and kidney functions as evident from little changes in RBC and WBC counts in peripheral blood, and serum levels of transaminases and creatinine (Figure 44A-F). These preliminary data clearly demonstrate the benefit of i.v. delivery of MSOP using NPs.

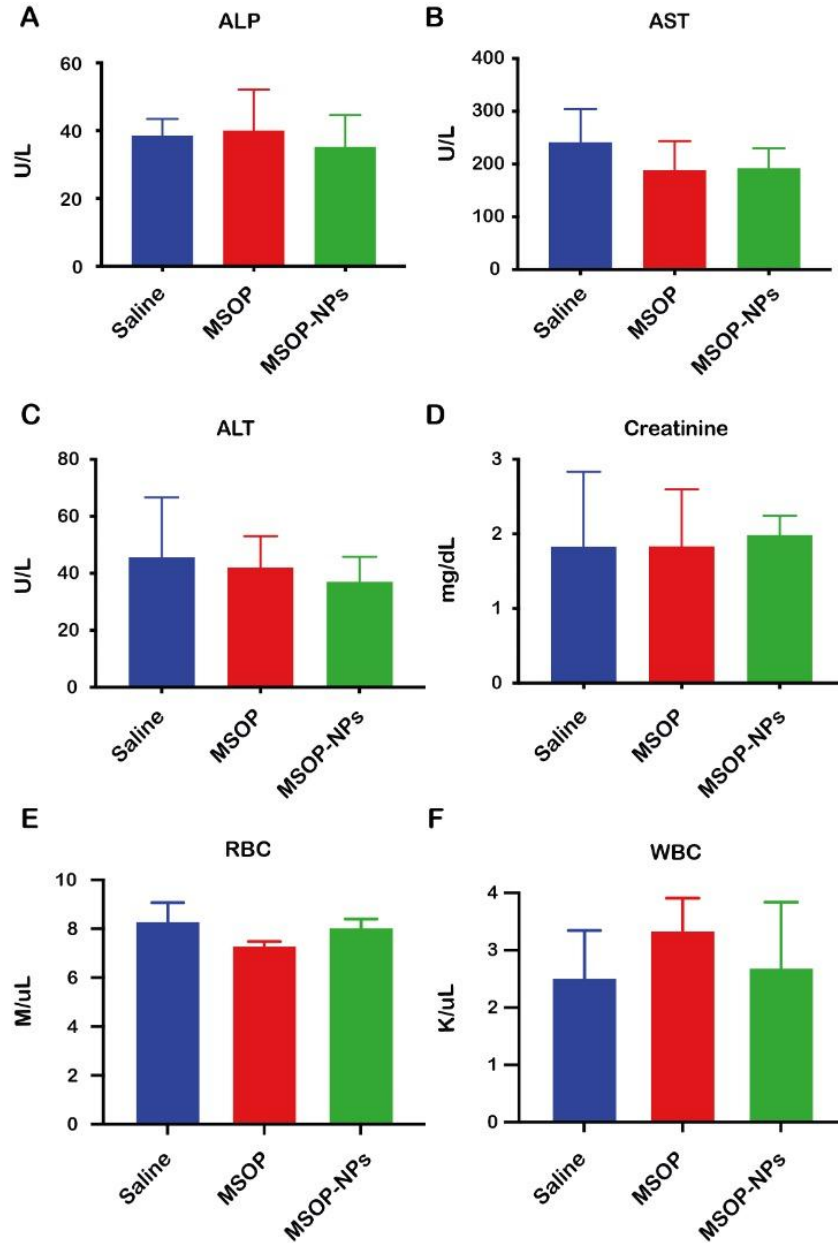


Figure 44 Safety Profiles of MSOP-NPs.

B16 tumor-bearing mice were treated with free MSOP or MSOP NPs as described in **Figure 8T**. Changes in serum levels of ALP (A), AST (B), ALT (C), and creatinine (E), and red blood cells (RBC) and white blood cells (WBC) in peripheral blood were examined at the completion of the experiment.

Figure 45 shows that incorporation of MSOP into the NPs was not associated with any increase in cytotoxicity towards either tumor cells or splenocytes. These preliminary data clearly demonstrate that i.v. delivery of MSOP using NPs is safe, and enhances the antitumor activity largely through improved delivery to target tissues/cells.

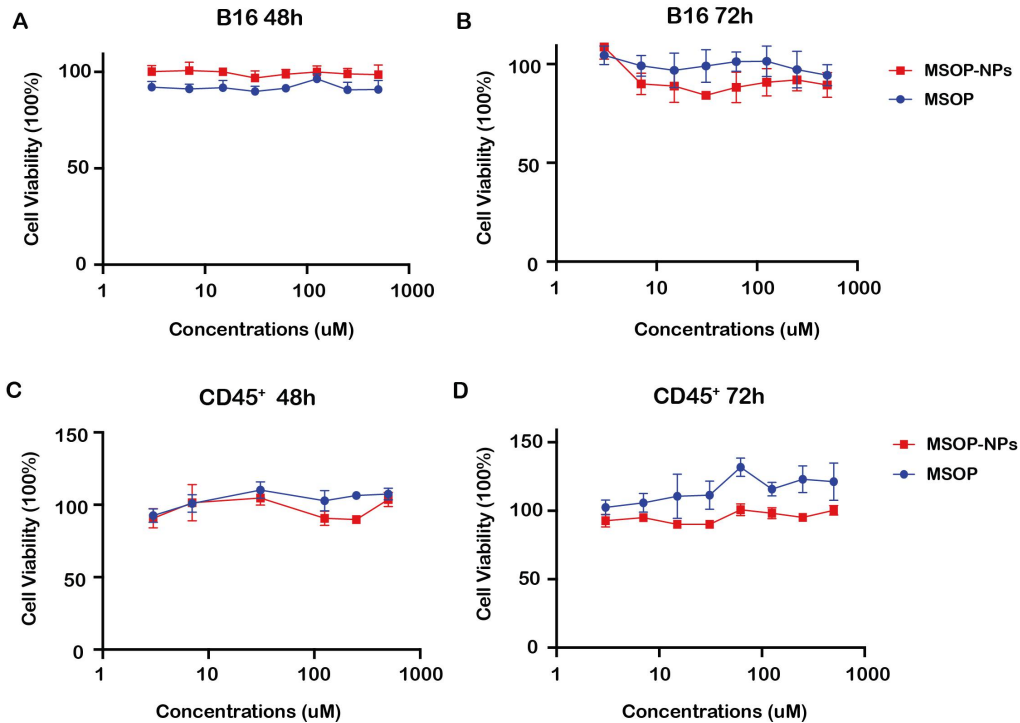


Figure 45 *In Vitro* Cytotoxicity of MSOP and MSOP NPs.

Cultured B16 cancer cells (A & B) and isolated mouse CD45+ splenocytes (C & D) were treated for 48 (A & C) and 72 (B & D) hours, respectively, and cytotoxicity was determined by MTT assay (n=3-6). MTT data were presented as means \pm SD and analyzed by unpaired Student's T test and two-way ANOVA in Prism. *p < 0.05, **p < 0.01, ***p < 0.001, ****p < 0.0001, ns (non-significant).

2.4.13 NK^{high}-GRM4^{low} and CD8^{high}-GRM4^{low} signatures predict improved patient survival

Our data so far have clearly pointed GRM4 as a negative regulator of antitumor immunity and a potential therapeutic target to improve cancer immunotherapy. Considering an inhibitory role of GRM4 in regulating the recruitment and activation of both NK and CD8⁺ T cells, we sought to analyze whether a signature of NK^{high}-GRM4^{low} and/or CD8^{high}-GRM4^{low} in human tumor samples would be of clinical significance in predicting the prognosis of cancer patients.

Three independent cancer patient cohorts were analyzed, including (i) 103 primary skin cutaneous melanoma (SKCM) patients from The Cancer Genome Atlas (TCGA) datasets, (ii) 34 acral melanoma patients [84], and (iii) 110 metastatic melanoma patients [85]. In addition to analyzing the overall correlation between NK-GRM4 (or CD8-GRM4) signatures and patient survival, the impact of gender on the correlation in each cohort was also examined. The data were presented as comparing patient survival between patients with NK (or CD8)^{high}-GRM4^{low} versus NK (or CD8)^{low}-GRM4^{high} signatures (See Methods) (Figure 46 and Figure 47). The results clearly indicate that patients with NK^{high}-GRM4^{low} signature show a trend of better survival in two independent datasets. Similarly, CD8^{high}-GRM4^{low} signature was also significantly correlated with the better patient survival in three independent datasets (Figure 46 and Figure 47). These data suggest that the NK^{high}-GRM4^{low} and/or CD8^{high}-GRM4^{low} signatures may serve as biomarkers for predicting the prognosis of melanoma patients. Interestingly, similar to what was found in mouse study, the correlation of NK (or CD8)-GRM4 expression signature with clinical prognosis was of higher predictive values in male patients compared to female patients (Figure 46 and Figure 47). More studies with larger sample size are needed to further define the clinical significance of these biomarkers.

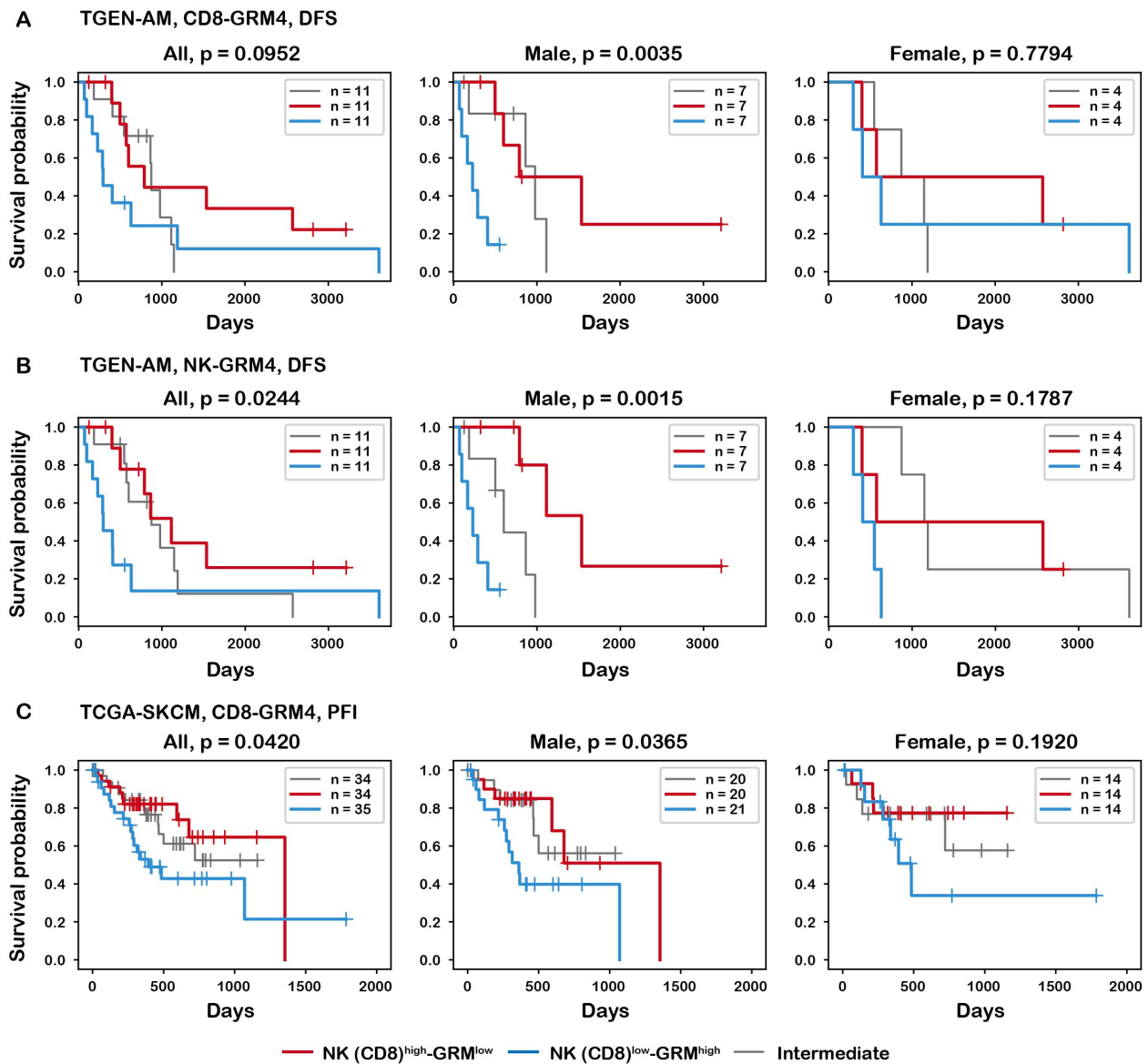
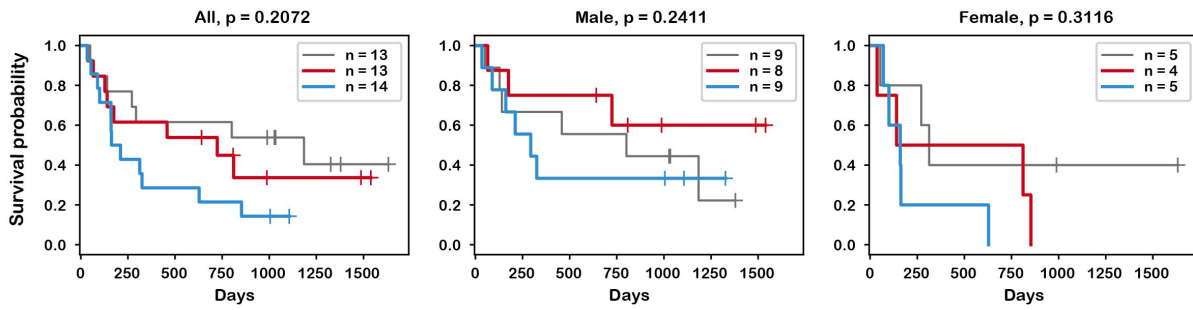


Figure 46 NK (CD8)^{high}-GRM4^{low} Signature is Associated with Improved Patient Survival in Male Melanoma Patients.

Melanoma patients were grouped based on NK (CD8)-GRM4 signature. If gender information was included, patients were first separated based on gender, and then grouped based on the NK (CD8)-GRM4 signature. Statistical significance for patient survival between NK (CD8)^{high}-GRM4^{low} and NK (CD8)^{low}-GRM4^{high} groups was calculated by Log-rank (Mantel-Cox) test. (A-B) TGEN-AM indicates an Acral Melanoma dataset from the Translational Genomics Research Institute (see Methods). DFS: disease-free survival; (C) TCGA-SKCM indicates an SKCM data set from The Cancer Genome Atlas (TCGA); PFI: progression-free interval.

DFCI, CD8-GRM4, OS



DFCI, NK-GRM4, OS

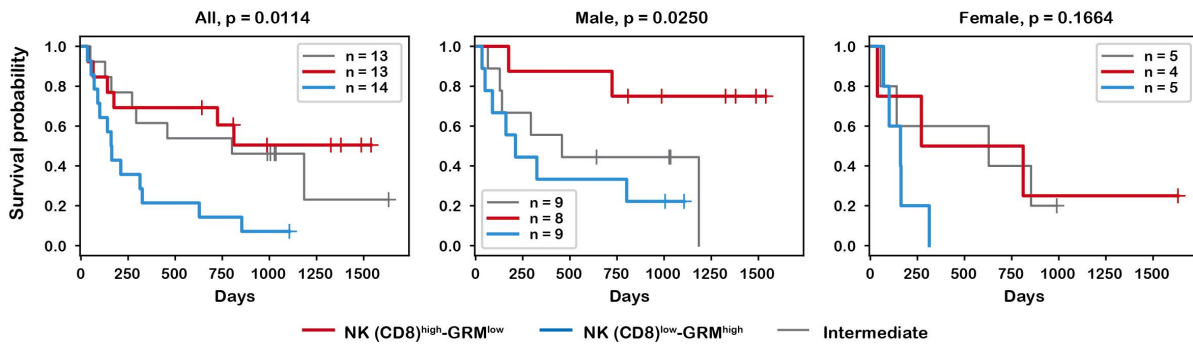


Figure 47 NK (CD8)^{high}-GRM4^{low} is Associated with Improved Patient Survival in Male Melanoma Patients.

Melanoma Patients were grouped based on NK (CD8)-GRM4 signature level. If gender information was included, patients were first separated based on gender, and then grouped based on the NK (CD8)-GRM4 signature. Statistical significance for patients' survival between NK (CD8)^{high}-GRM4^{low} and NK (CD8)^{low}-GRM4^{high} was calculated by Log-rank (Mantel-Cox) test. DFCI indicate a metastatic melanoma dataset from the Dana-Farber Cancer Institute (see Methods). OS: overall survival.

2.5 Discussion

We have shown for the first time in this study that GRM4 in immune cells plays an important role in negatively modulating the antitumor immunity. Global *Grm4* knockout or pharmacological inhibition of GRM4 led to significant improvement in tumor immune microenvironment and significant inhibition of tumor growth in several syngeneic tumor models.

The information on the role of GRM4 in cancer so far is limited and controversial. A number of studies suggest a negative correlation between the expression of GRM4 in tumor tissues and the patients' prognosis in several types of cancer, including colorectal cancer, pediatric CNS tumors, rhabdomyosarcoma, and multiple myeloma [47, 149]. However, GRM4 agonists are also shown to inhibit the proliferation of human breast and bladder cancer cells [49, 75]. These studies focus on the direct effect of GRM4 agonists on cancer cells and only limited antitumor activity is shown in a human tumor xenograft model [49]. A recent study from Kansara et al shows that *Grm4* gene-targeted mice have accelerated tumor development in an irradiation-induced osteosarcoma mouse model [53]. It was hypothesized that increased production of IL-23 from *Grm4*^{-/-} myeloid cells plays a role based on the protective effect of *IL-23*^{-/-} in the animal model and a negative correlation of IL23 expression with the prognosis of osteosarcoma patients. In addition, they have further shown that PHCCC, a GRM4 agonist significantly inhibits the growth of transplanted osteosarcoma cells (OS18) in *Grm4*^{+/+} mice (10). However, the direct impact of GRM4 agonist on the proliferation of OS18 cells is not known and it is unclear whether the inhibitory effect of PHCCC on OS18 tumor is maintained in *Grm4*^{-/-} mice. So far, there is hardly any information of how genetic knockout or pharmacological

inhibition of GRM4 affects the innate and adaptive immunity in the context of established tumor models.

Using *Grm4*^{-/-} mice and the control *Grm4*^{+/+} littermates, we first showed that genetic knockout of *Grm4* led to significant inhibition of tumor growth in three syngeneic tumor models (B16, 3LL, and MC38). Pharmacological inhibition of GRM4 with MSOP led to similar results in the three tumor models in *Grm4*^{+/+} mice. In addition, the tumor inhibitory effect of MSOP was abolished in *Grm4*^{-/-} mice, suggesting a role for GRM4 in MSOP-mediated antitumor activity. These data strongly suggest that the tumor growth inhibition following GRM4 disruption may be largely mediated via an immune mechanism rather than direct effect on tumor cells.

Genetic knockout of *Grm4* in B16 tumor model led to significant changes in gene expression profile and GSEA of the tumor bulk RNA-Seq data revealed significant downregulation of several tumor-promoting signaling pathways. In addition, significant enrichment of numerous immune-related pathways was found in B16 tumor grown in *Grm4*^{-/-} mice: 10 out of the top 15 upregulated pathways revealed in RNA-Seq were immune-related. It is interesting to note that both NK cells and CD8⁺ T cells in tumor tissues were significantly increased in *Grm4*^{-/-} mice and these immune cells are of highly active and proliferative phenotype. ScRNA-Seq suggests that *Grm4*^{-/-} prevented CD8⁺ T cells from entering into an exhausted state and preferentially increased the proliferative and activated functionality in the sub-cluster of CD8-C7-Itgb1 that is highly active in producing IFN- γ . ScTCR profiling suggests that CD8⁺ T cells of different clusters are not completely independent but might undergo extensive state transitions. The most significant differences in clonal expansion of CD8⁺ T cells

between WT and *Grm4*^{-/-} mice were seen in the clusters of CD8-C1-Xcl1, CD8-C6-Prf1, and CD8-C7-Itgb1. There were more frequent TCRs in the clusters of CD8-C1-Xcl1, CD8-C6-Prf1, and CD8-C7-Itgb1 in *Grm4*^{-/-} mice compared to WT control. Interestingly, significant clonal expansion was also seen in WT mice but was selectively concentrated within the subcluster of CD8-C3-Tigit. The underlying mechanism is unknown at present but clearly knockout of *Grm4* redirects the transition of expanded CD8⁺ T cells to the subclusters of CD8-C6-Prf1 and CD8-C7-Itgb1.

Both NK and CD8⁺ T cells are critically involved in the antitumor activity in *Grm4*^{-/-} mice as neutralizing antibody for each subpopulation drastically attenuated the tumor inhibitory effect. The NK cells may be associated with the tumor growth suppression at early phase after tumor inoculation while the cellular immunity plays an important role in controlling the tumor growth at a late stage. Similar changes in immune subpopulations were observed in B16-bearing *Grm4*^{+/+} mice treated with MSOP, further establishing a role of GRM4 in modulating antitumor immunity.

The role of GRM4 in immune modulation was first reported by Fallarino et al in an EAE model. They hypothesized that disruption of GRM4 in DCs led to differentiation of naïve CD4⁺ T cells into Th17 cells through increased production of IL23 and IL6 in DCs, which contributed to the initiation and progression of EAE [33]. Similar to the study by Fallarino et al and the work by Kansara et al in an osteosarcoma model, we also saw increased expression of IL-23 in *Grm4*^{-/-} mice in our B16 model. However, only small changes were found in the expression levels of IL-17 from both bulk and single-cell RNA-Seq in our study. In fact, the overall changes in tumor-

infiltrating *Grm4*^{-/-} CD4⁺ T cells were much less dramatic compared to those in *Grm4*^{-/-} CD8⁺ T cells. Interestingly, naïve NK or CD8⁺ T cells isolated from *Grm4*^{-/-} mice are more active as shown by the increased production of IFN- γ and higher level of antitumor activity in an adoptive T cell transfer study. Therefore, while a role of the impact of *Grm4*^{-/-} on DCs and CD4 cells cannot be ruled out in *Grm4*^{-/-}-mediated antitumor activity, our data strongly suggest that *Grm4*^{-/-} can directly activate CD8⁺ T cells, and possibly NK cells as well.

Mechanistically, GRM4 has been shown to negatively regulate intracellular cAMP levels in a Gi protein-dependent fashion in presynaptic nerve terminals and microglia as well as in DCs [33, 141]. cAMP has long been known to exert suppressive effects on the immune system. Accordingly, bacterial toxins and chemical agents that cause a sustained elevation of cAMP are immuno-suppressive [150]. However, recent studies have highlighted a positive role of cAMP in immune cell function [87, 143, 151, 152]. The differential effects of cAMP on cellular functions can be accounted for by a number of factors such as different cell types, the amount of cAMP produced, and the cAMP target genes involved. Our data showed that the basal level of intracellular cAMP was slightly increased in *Grm4*^{-/-} CD8⁺ T cells but became significantly higher in the presence of forskolin. Along with these changes, we observed increased levels of pCREB and IFNGR1 in *Grm4*^{-/-} CD8⁺ T cells. ScRNA-Seq revealed enhanced PKA/CREB immune signaling in *Grm4*^{-/-} CD8⁺ T cells as well as a strong correlation of *Creb1* expression with those of *Ifng* and *Ifngr1*. Taken together our data suggest a likely role of GRM4/cAMP/CREB pathway in direct activation of CD8⁺ T cells in *Grm4*^{-/-} mice. In addition to cAMP/CREB, other signaling pathways also are regulated by GRM4 [153, 154]. Whether and how each pathway is modulated by GRM4 could be affected by the cell type, structure, and

concentration of the ligand involved. More studies are needed to better define the underlying mechanism for GRM4-mediated antitumor immunity.

The immune-active TME following *Grm4* knockout was also associated with induction of adaptive immune resistance characterized by upregulation of PD-1 and CTLA-4 signaling. Upregulation of PD-1 and CTLA-4 was similarly observed following MSOP treatment. The induction of adaptive immune resistance is likely attributed, at least partially, to the enhanced IFN- γ response, which was further confirmed by scRNA-seq results. The elevated expression of transcripts encoding PD-1 (*Pdcd1*) and CTLA-4 (*Ctla4*), the corresponding T cell inhibitory receptors, were observed in effector CD8⁺ subsets particularly in the cluster of CD8-C7-Itgb1 (IFN- γ -producing subpopulation) instead of CD8-C3-Tigit (exhausted). Nonetheless, this suggests an opportunity of further improving the antitumor activity through combining the inhibition of GRM4 signaling with anti-PD-1 or CTLA-4-based ICB. Indeed, treatment with anti-PD-1 or CTLA-4 antibody led to more drastic inhibition of the growth of B16 tumor in *Grm4*^{-/-} mice. More importantly, the improvement in antitumor response was similarly achieved in *Grm4*^{+/+} mice through combination of a pharmacological inhibitor (MSOP) with anti-PD-1 or CTLA-4 monoclonal antibody, suggesting a potential of translation into clinic.

One drawback of MSOP is its short half-life in blood which necessitates frequent dosing and limits its translation into clinic. Nanoparticles are known to improve the half-life of the formulated drugs in blood and enhance their delivery to tumors [155]. One common concern over nanoparticles is the non-selective uptake by RES. However, this “undesired feature” may work favorably for *in vivo* application of MSOP through enhanced delivery to immune cells-

enriched organs such as spleen. Lipid-coated calcium-phosphate (LCP) nanoparticle has been developed as a versatile platform for delivery of various therapeutics including gene, protein/peptide, and chemotherapeutic agents due to its simplicity and biocompatibility [77]. LCP is particularly suitable for delivery of MSOP due to the presence of a phosphate group, which facilitates the formation of a CP core. Our preliminary data showed that this approach is both simple and effective in improving the *in vivo* therapeutic efficacy of MSOP.

The studies on the clinical relevance of GRM4 in cancer patients is limited so far and conflicting results have been reported. Considering our appealing data that are suggestive of a role of immune cells-derived GRM4 in anticancer immunity, we investigated whether a signature of NK^{high}-GRM4^{low} and/or CD8^{high}-GRM4^{low} would be of clinical significance in predicting the prognosis of melanoma patients. Indeed, analysis of three independent datasets shows a positive correlation of the NK^{high}-GRM4^{low} and/or CD8^{high}-GRM4^{low} signature with a better prognosis of cancer patients. More studies with larger sample sizes are needed to further define the clinical value of these signatures as biomarkers in cancer care.

One surprising observation in this study is that the significant tumor growth inhibition with both genetic and pharmacological perturbation of *Grm4* was only seen in male mice and not in female mice. In addition, the correlation of the signature of NK^{high}-GRM4^{low} and/or CD8^{high}-GRM4^{low} with cancer patient survival was of better predictive values in male patients than in female patients, despite the relatively small sample sizes of the 3 cohorts analyzed. The underlying mechanism is unclear at present. Differences in the levels of GRM4 expression in immune cells between males and females do not appear to play a major role although more

studies are needed to further establish this notion. Nonetheless, unlike what was seen in male mice, knockout of *Grm4* resulted in minimal changes in the numbers of IFN- γ producing tumor-infiltrating CD8⁺ cells in female B16 tumor-bearing mice, suggesting that the differences in immune response likely play a role. Sex has been shown to have a major impact on both innate and adaptive immunity as well as numerous immune pathways [156]. More studies are needed to understand how sex differences affect the GRM4-mediated antitumor immunity. Our data also suggest caution in considering the gender factor in future studies on the immunomodulating function of GRM4.

In summary, we have unveiled a novel role of immune cell-derived GRM4 in regulating antitumor response. Inhibition of GRM4 signaling led to transformation of TME into a more immunogenic phenotype that is associated with significant inhibition of tumor growth. Combination of a pharmacological inhibitor (e.g., MSOP) with ICB using anti-PD-1 or anti-CTLA-4 led to a further improvement in antitumor activity. We have also demonstrated that the therapeutic potential of GRM4 inhibitor can be further enhanced via improved delivery using NPs. Our data suggest that targeting of GRM4, alone or in combination with ICB, may represent a new therapeutic strategy to improve cancer immunotherapy.

3.0 Dual Functional Immunostimulatory Polymeric Prodrug Carrier with Pendent Indoximod for Enhanced Cancer Immunotherapy

3.1 Abstract

Immunotherapy based on checkpoint blockade has been regarded as one of the most promising approaches towards many types of cancers. However, low response rate hinders its application due to insufficient tumor immunogenicity and immunosuppressive tumor microenvironment. To achieve an overall enhanced therapeutic outcome, we developed a dual-functional immuno-stimulatory polymeric prodrug carrier modified with pendent indoximod, an indoleamine 2,3-dioxygenase (IDO) inhibitor that can be used to reverse immune suppression, for co-delivery of Doxorubicin (Dox), a hydrophobic anticancer agent that can promote immunogenic cell death (ICD) and elicit antitumor immunity. The resultant carrier denoted as POEG-b-PVBIND, consisting of poly (oligo (ethylene glycol) methacrylate) (POEG) hydrophilic blocks and indoximod conjugated hydrophobic blocks, is rationally designed to improve immunotherapy by synergistically modulating the tumor microenvironment (TME). Our data showed that Dox-triggered ICD promoted intra-tumoral infiltration of CD8⁺ T cells and IFN- γ production by CD8⁺ T cells. Meanwhile, cleaved indoximod significantly increased CD8⁺ T cell infiltration while reducing the immunosuppressive T regulatory cells (Tregs). More importantly, Dox/POEG-b-PVBIND micelles led to significantly improved tumor regression in an orthotopic murine breast cancer model compared to both Dox-loaded POEG-b-PVB micelles (a control inert carrier) and POEG-b-PVBIND micelles alone, confirming combination effect of indoximod and Dox in improving the overall antitumor activity.

3.2 Introduction

Immunotherapy has been regarded as one of the most promising approaches towards many types of cancers, especially with the success of Yevoy[®] and Opdivo[®] that target CTLA-4 and PD-1, respectively[13-16]. Indoleamine 2,3-dioxygenase (IDO) has emerged as another important immuno-oncology target for next groups of immune-based drugs due to its important role in driving the immune suppressive TME through tryptophan depletion and kynurenine accumulation [60, 157]. Five mechanistically distinct IDO inhibitors were under development over the past few years[66]. But low clinical response rates hinder their application. Combination with chemotherapy is one of the validated strategies to significantly improve anti-tumor response compared to each single agent alone[158-160]. The mechanism of action (MOA) behind this successful combination is largely due to an overall enhanced immune response, since IDO inhibitors could potentially amplify the immune response induced by the chemo-therapeutic agents that can trigger the immunogenic cell death (ICD)[161-164]. However, highly efficient combination therapy was limited by poor solubility, different pharmacokinetic profiles, poor tumor biodistribution and systemic toxicities of these combined agents[165].

Polymers with customizable structures have been widely exploited as ideal delivery carriers for combination therapy. Specifically, polymeric micelles have shown great clinical potential due to their capability of co-encapsulating poorly soluble drugs and efficiently delivering them into tumor areas via EPR effect[165]. Prodrug polymers can also be designed to serve as dual-functional micelle carriers to co-deliver other hydrophobic drugs for combination effect[166, 167]. Significantly enhanced antitumor effect was achieved recently based on a PEG_{2k}-modified prodrug of NLG-919 for co-delivery of paclitaxel, an ICD-inducing agent, and

NLG919, a selective IDO1 inhibitor. More importantly, therapeutic advantages were also observed in comparison with combination of Abraxane and i.v. delivery of NLG919 via an inert nanocarrier as well as combination of Abraxane and oral delivery of NLG919, indicating highly efficient immuno-chemotherapy based on this strategy[168]. However, a major limitation for the NLG-919-paclitaxel system is the low loading capacity of NLG919, because each molecule of nanocarrier carries only one molecule of NLG919.

There are two isoforms of the IDO enzymes, IDO1 and IDO2[67]. In addition, tryptophan-2,3-dioxygenase (TDO) is also involved in tryptophan metabolism[169]. Among them, IDO1 has been most extensively studied because IDO1 is overexpressed in many types of tumor cells as well as certain immune cells in tumor tissues[170]. Surprisingly, selective IDO1 inhibitors such as NLG-919 failed in clinical trials. It is unclear whether delivery is an issue or other issues are involved in the unexpected failure. Indoximod (IND) was another well-studied IDO inhibitor. Recent studies have demonstrated that IND not only acted in inhibiting the IDO activity but also drove antitumor immune responses independently from IDO/TDO. In the presence of IND, the activity of IDO in dendritic cells (DCs) is inhibited. Meanwhile, IND promotes T cell activation and proliferation and reprograms Treg cells into T helper cells in an IDO/TDO independent manner[171]. Additionally, IND can prevent the recruitment of myeloid-derived suppressor cells (MDSCs) in the tumor site[66, 171-174]. Therefore, IND is able to exert multiple immunomodulatory effects in tumors[60, 67, 70, 171, 172, 175, 176]. Therapeutic benefits were also demonstrated in the clinic with IND in combination with other treatments such as chemotherapy or anti-PD-1 antibody[177-182].

Despite the demonstrated potential, the pharmaceutical utility of IND is limited by its poor water solubility and low bioavailability and various IND derivatives of improved solubility and PK profile have been developed[183]. One such prodrug, NLG-802, is currently being tested in clinic in patients with advanced solid tumors[73, 74]. Another strategy to improve the therapeutic efficacy focuses on the development of a nanocarrier to enhance delivery of IND to tumors. Several IND-based nanomedicines have been reported including an oral nanocrystal formulation for lung cancer[183], an intratumorally injectable liposome for co-delivery of IND and hydrophilic drugs for pancreatic cancer[184], and an intratumorally injectable IND hydrogel in combination with PD1 antibody for treating melanoma[185]. However, few reports have been published on systemic co-delivery of IND and hydrophobic chemotherapeutic agents. In addition, it is difficult to achieve an optimal release of IND and chemodrug in *a temporal and spatial manner*[186].

Based on our success and limitation of NLG919-based prodrug carrier, we designed and synthesized an IND-based prodrug polymer, POEG-b-PVBIND, which could self-assemble to form micelles and serve as a dual-functional carrier to deliver Dox, a DNA-damaging agent that can promote ICD (Figure 48). POEG-b-PVBIND consists of hydrophilic segments of poly (oligo (ethylene glycol) methacrylate) (POEG) and hydrophobic segments of vinylbenzyl chloride with a number of IND molecules covalently attached. These two segments were polymerized in a tunable manner via reversible addition fragmentation chain transfer (RAFT) polymerization for optimal codelivery of IND and DOX. We hypothesize that the physically loaded Dox will be rapidly released from the nanocarrier at the tumor site, leading to ICD of tumor cells and the induction of antitumor immunity. Meanwhile, the covalently conjugated IND will be slowly

released, helping to sustain an active immune microenvironment for an extended period of time. Using a 4T1.2 murine breast cancer model, we demonstrated that intravenous administration of POEG-b-PVBIND micelles alone was effective in enhancing immune responses and exhibited antitumor activity in vivo. More importantly, delivery of Dox via POEG-b-PVBIND micelles led to potent and sustained antitumor effect, with improved tumor immune microenvironment.

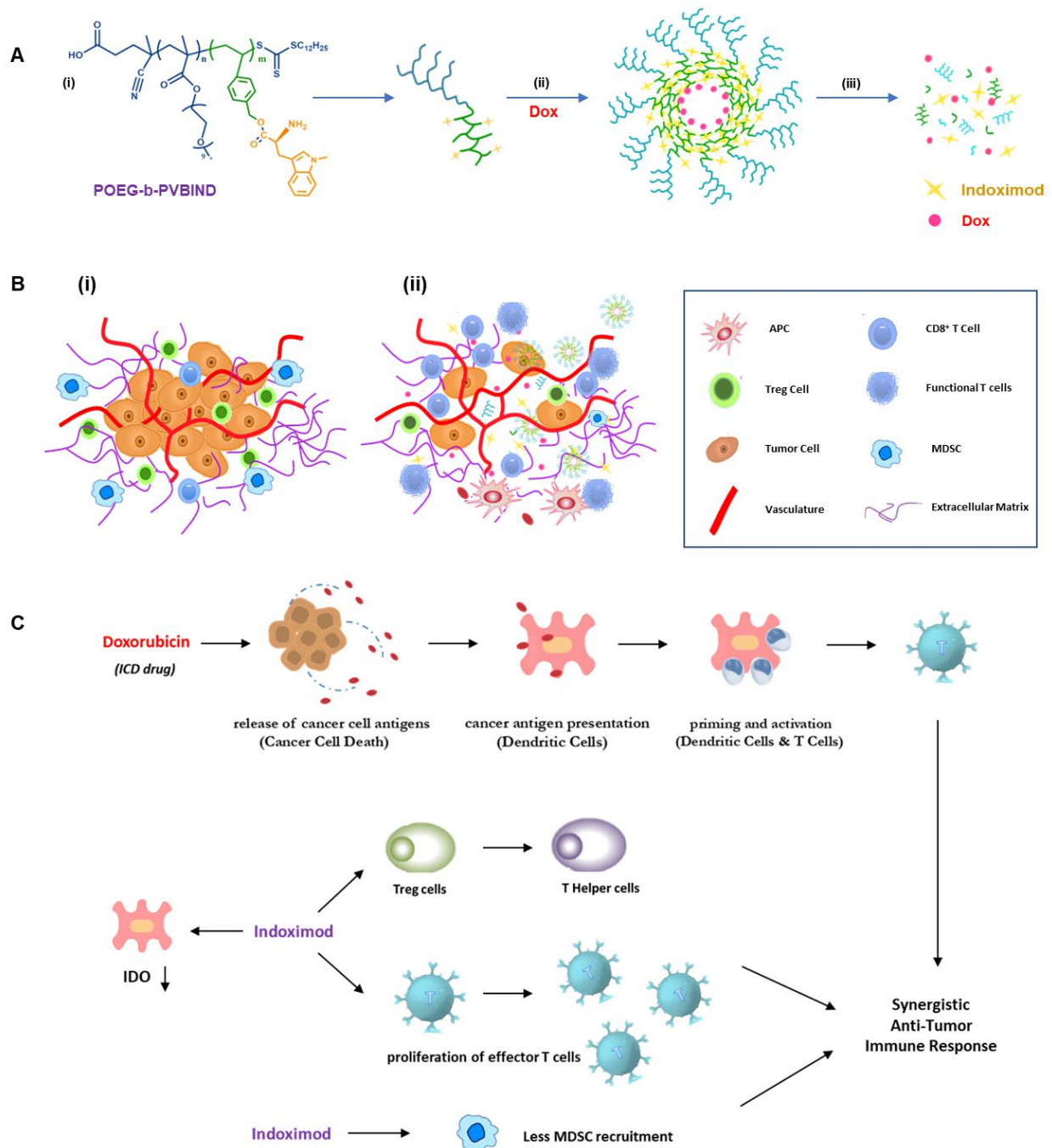


Figure 48 IND-based polymeric micelles for immuno-chemotherapy.

(A) illustration of encapsulation and release of IND and Dox from POEG-b-PVBIND/Dox micelles: (i) structure of POEG-b-PVBIND; (ii) self-assembly of Dox-loaded IND-based micelles; and (iii) dissociation of POEG-b-PVBIND/Dox micelles within tumor microenvironment; (B) Schematic diagram of POEG-b-PVBIND/Dox micelles

to elicit anti-tumor immunity for improved chemo-immunotherapy: (i) initial immune-suppressive tumor microenvironment; (ii) immuno-active tumor microenvironment after treatment of POEG-b-PVBIND/Dox micelles; (C) Rationale of IND and Dox for synergistic immuno-chemotherapy.

3.3 Materials and Method

3.3.1 Materials

Indoximod (IND) was purchased from Sigma-Aldrich (MO, USA). Doxorubicin hydrochloride (DOX·HCl) was obtained from LC Laboratories (MA, USA). Vinylbenzyl chloride, potassium carbonate (K_2CO_3), azobisisobutyronitrile (AIBN), petroleum ether (PE), sodium hydroxide (NaOH), 2-hydroxyethyl methacrylate, di-tert-butyl dicarbonate, 1,4-dioxane, dimethylformamide (DMF), dimethyl sulfoxide (DMSO), tetrahydrofuran (THF), triethylamine (TEA), 4-cyano-4-[(dodecylsulfanylthiocarbonyl) sulfanyl] pentanoic acid, poly(ethylene glycol) methyl ether methacrylate (OEGMA, $M_n=500$), and 1,1'-dioctadecyl-3,3,3',3'-tetramethylindotricarbocyanine iodide (DiR) were purchased from Fisher Scientific (Pittsburgh, PA).

3.3.2 Cell lines and tumor models

4T1.2 (murine breast cancer cell line) cells were obtained from ATCC (Manassas, VA) and cultured in Dulbecco's Modified Eagle's Medium (DMEM) supplemented with 10% fetal

bovine serum (FBS) and 1% penicillin-streptomycin at 37 °C in a humidified environment with 5% CO₂[187].

The female BALB/c mice (4-5 weeks) of 18-20 g were purchased from Charles River (Davis, CA, USA). All animal protocols were approved by Institutional Animal Care and Use Committee at the University of Pittsburgh, and all animal studies were performed according to the guidelines approved by the Ethics Committee of University of Pittsburgh. All the mice were housed under pathogen free conditions. Orthotopic 4T1 breast tumors were generated by injecting 5×10^5 cells into the mammary fat pad (left) of female BALB/c mice at the age of 6-8 weeks.

3.3.3 Synthesis of Boc-Protected Indoximod

IND (200mg, 0.909mmol, 1.0 eq), NaOH (86mg, 2.15mmol, 2.36 eq) and di-tert-butyl dicarbonate (470mg, 2.15mmol, 2.36eq) were dissolved in a mixed solvent of THF (9ml) and H₂O (9.8ml). The mixture was stirred at room temperature for 48h. THF was evaporated under reduced pressure, and the remaining aqueous layer was acidified with 1N HCl to pH=3. IND-Boc was extracted by ethylacetate three times, and the organic layer was collected and concentrated to give the product as a yellow solid (264mg, 0.825mmol, 90% yield) [188].

3.3.4 Synthesis of POEG-MacroCTA

POEG MacroCTA was synthesized and purified following a published protocol^[166]. Briefly, OEGMA 500 (3.05g, 6.10mmol, 20.5 eq), 4-Cyano-4-[(dodecylsulfanylthiocarbonyl)sulfanyl] pentanoic acid (120mg, 0.297 mmol, 1.0 eq), AIBN (8mg, 0.048mmol) and 5ml anhydrous THF were mixed in a Schlenk tube. The mixture was then purged with nitrogen so as to remove the oxygen dissolved in the reaction solvent by using a freeze-pump-thawing method. Then, the tube was immersed in an oil bath at 85°C for 130 mins under nitrogen protection. After polymerization, the reaction was first quenched in a liquid nitrogen bath. Next, the POEG MacroCTA was purified by precipitation and extraction using cold diethyl ether three times. Finally, POEG MacroCTA was obtained in the form of yellow liquid oil (2.3977g, 91% yield), followed by vacuum drying. The conversion rate was 86% as determined by ¹H NMR spectroscopy of POEG MacroCTA before purification, which was equivalent to 17 POEG units.

3.3.5 Synthesis of POEG-b-PVB and POEG-b-PVBIND Polymers

POEG MacroCTA (213mg, 0.025mmol, 1.0 eq), vinylbenzyl chloride (70mg, 0.45mmol, 18.0 eq), AIBN (2mg, 0.0122mmol), and 2.5ml anhydrous 1,4-Dioxane were added into a Schlenk tube. The mixture was de-oxygenated three times using a free-pump-thaw method. Then the tube was immersed in an oil bath at 90°C for 5.5 hours. At the completion of reaction, the mixture was precipitated in petroleum ether three times. The POEG-b-PVB polymer was finally obtained after vacuum drying.

To obtain POEG-b-PVBIND polymer, the as-synthesized POEG-b-PVB polymer (200mg, 0.018mmol, 1.0 eq), Boc-Protected IND (250mg, 0.78mmol, 43.3 eq), and K₂CO₃ (181mg, 1.31mmol, 72.7 eq) were dissolved in 5.5ml DMF for further reaction. One molecule of POEG-b-PVB polymer has ten benzyl chloride units (Figure 1A) and the input of benzyl chloride was 0.18 mmol. The input of Boc-Protected IND was calculated to be 0.78 mmol. Therefore, the reaction ratio of IND/benzyl chloride was 4.3:1. After stirring at 80°C overnight, 5ml cool water was added into reaction mixture and the mixture was then dialyzed (3500 Da MW cutoff) against DMSO for one day and deionized water for another two days. The final product POEG-b-PVBIND-Boc was obtained after lyophilization. The POEG-b-PVBIND-Boc polymer was deprotected in a mixture solution of DCM/TFA (6/5, v/v) at ambient temperature. After 75 min, the reaction mixture was precipitated in diethyl ether. The crude product was dissolved in the mixed solvents of DCM/ethanol and was then precipitated by ether again. The deprotected POEG-b-PVBIND polymer was dried in vacuum to afford the product in a sticky and brown oil form.

3.3.6 Micelle Preparation and Characterization

To obtain Dox free base solution, 10mg Dox hydrochloride and 15uL TEA were added into 1 ml DMSO for overnight reaction[166, 189-191]. The POEG-b-PVBIND blank micelles and Dox-loaded POEG-b-PVBIND micelles were prepared through a dialysis method. In brief, 25 mg POEG-b-PVBIND polymer was dissolved in 400 μ L DMSO. Dox free base/DMSO stock solution (70 μ L) at a concentration of 10mg/ml was added into this polymer solution (DOX/polymer:1/35, w/w). After a 60s mixing, the mixture was placed into a dialysis bag (3500 Da MW cutoff) and dialyzed against 1 \times PBS buffer overnight so as to remove organic solvent and free Dox. Blank micelles were prepared in a similar method without adding Dox solution.

The size distribution and zeta potential of Dox-loaded POEG-b-PVBIND micelles and POEG-b-PVBIND micelles were examined by a Zeta Nanosizer (Malvern) after a 0.45 μ m filtration. All the sizes of micelles were presented using diameter. The morphology of micelles was confirmed by transmission electron microscopy (TEM) using a negative staining method.

The Dox concentration was detected by a Waters 2475 Fluorescence Detector (excitation 490 nm/emission 600 nm). The Dox Loading Efficiency (DLE) and Dox Loading Capacity (DLC) were calculated as the following equations:

$$\text{DLE (\%)} = (\text{Weight of Loaded Drug} / \text{Weight of Input Drug}) \times 100$$

$$\text{DLC (\%)} = (\text{Weight of Drug Loaded} / \text{Weight of Polymer} + \text{Weight of input Drug}) \times 100$$

3.3.7 Critical Micelle Concentration (CMC) and Storage Stability

The CMC value of POEG-b-PVBIND micelles was determined using Nile red as a fluorescence probe. In brief, equal aliquots of Nile red DCM solution (photo-sensitive) were added to test tubes and DCM solvent was evaporated by air flow followed by further drying by vacuum pump. A series of concentrations of POEG-b-PVBIND micelles ranging from 0.5 mg/ml to 1.0×10^{-4} mg/ml, were then added into those test tubes for overnight incubation in a dark place. The final concentration of Nile red was kept at 6.0×10^{-7} mol/L after dilution. The fluorescence was determined by a Waters 2475 Fluorescence Detector (excitation 550 nm/emission 520/720 nm). The CMC value was determined as the cross-point when extrapolating the intensity at low and high concentration regions. The colloidal stability of POEG-b-PVBIND and POEG-b-PVBIND/Dox was evaluated by following the changes in particle sizes and drug content during storage at 4 °C.

3.3.8 In Vitro Cytotoxicity of POEG-b-PVBIND micelles

The in vitro cytotoxicity of free Dox, POEG-b-PVBIND alone, POEG-b-PVBIND/Dox, and POEG-b-PVB/Dox against 4T1.2 was evaluated and compared by MTT assay. 4T1.2 at 2500 cells/well were seeded in a 96-well plate. After 12 hours of incubation, cell culture medium was removed and a series of concentrations of free Dox, POEG-b-PVBIND, POEG-b-PVBIND/Dox and POEG-b-PVB/Dox were added to the cells. After 48h incubation, the medium was replaced with 100 μ L 1X MTT solution for four-hour incubation. Then, the medium was completely removed and MTT crystals were solubilized by 100 μ L DMSO in each well. Absorbance was

determined by a micro-plate reader at wavelength of 550nm. Untreated cells were used as a positive control. Cell viability was calculated as $((OD_{\text{treated}} - OD_{\text{blank}}) \times 100\%)$.

3.3.9 In Vitro Drug Release

To study the stability and release profile of POEG-b-PVBIND/Dox under physiological conditions, in vitro release rate of Dox from POEG-b-PVBIND/Dox at pH 7.4 was evaluated using a dialysis method. PBS buffer solution (0.1 M) containing 0.5% (w/v) Tween 80 was prepared so as to solubilize Dox base. Briefly, 300 μL of POEG-b-PVBIND/Dox and Dox Hydrochloride containing 0.15 mg Dox were placed into dialysis bags (MWCO 3.5 kDa), immersed into 50 mL capped tubes and dialyzed against 40mL PBS. This experiment was performed in a 37 °C incubation shaker at a speed of 100 rpm. At each predetermined time intervals, an aliquot (2 mL, 37°C) was drawn from the dialysate and was replenished with the same amount of fresh medium. The released Dox from those micelles was measured by fluorescence spectrometry. A standard curve was generated with Dox of the following concentrations: 1.25ug/ml, 0.9375ug/ml, 0.625ug/ml, 0.46875ug/ml, 0.3125ug/ml, 0.234375ug/ml, 0.15625ug/ml, 0.1171875ug/ml, and 0.078125ug/ml. $R^2 (\approx 1)$ indicates that the regression predictions perfectly fit the data within these gradient concentrations (Figure 49).

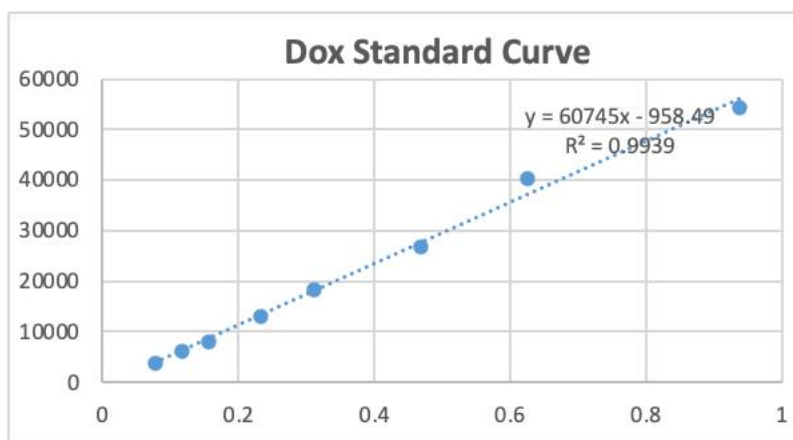


Figure 49 Calibration for quantification of Dox by fluorescence spectrometry.

The release of IND from POEG-b-PVBIND was also examined at different times in presence of porcine liver esterase (10 mM, Sigma-Aldrich, USA). The released IND was derivatized with 6-aminoquinolyl-n-hydroxysuccinimidyl carbamate and measured by UPLC-QTOFMS. [192]

3.3.10 In Vivo Distribution Profile

To investigate the distribution profile of POEG-b-PVBIND micelles in vivo, 1×10^7 4T1.2 cells were inoculated in the mammary gland of BALB/c mice. Ten days later, the mice bearing 4T1.2 tumors of $\sim 200 \text{ mm}^3$ were intravenously injected with free 1,1'-Dioctadecyl-3,3,3',3'-Tetramethylindotricarbocyanine Iodide (DiR) or DiR-loaded POEG-b-PVBIND at a DiR dose 5.0 mg/kg. The mice were euthanized at 2h, 4h, 12h, 24h, and 36h post-injection. Near-infrared fluorescence imaging in vivo was carried out with an IVIS imaging system. The tumors and major organs were then collected for ex vivo imaging.

To further investigate Dox delivery efficiency of POEG-b-PVBIND micelles, groups of five BALB/c mice bearing 4T1.2 tumors of $\sim 200 \text{ mm}^3$ were i.v. administered with free Dox, POEG-b-PVB/Dox and POEG-b-PVBIND/Dox at a dose of 5 mg Dox per kg. Mice were sacrificed 24 hours after injection and tumor tissues were collected[193]. Tumor frozen sections were obtained and then the fluorescence images were collected by CLSM (Ziss 710).

3.3.11 Anti-tumor Efficacy Study

Twenty-five female BALB/c mice (4-5 weeks) were used in this experiment and each mouse was s.c inoculated with 4T1.2 cells (2×10^5 cells/mouse)[194]. Mice were randomly divided into five groups (n=5) after tumor sizes reached around 30 mm^3 . Free Dox, POEG-b-PVBIND micelles, POEG-b-PVBIND/Dox and POEG-b-PVB/Dox were intravenously injected into each group at a Dox dose of 5mg/kg on days 0, 3 and 6, respectively. Tumor volumes were measured and calculated every three days based on the formula: $(L \times W^2)/2$ (L = Longest diameter; W = Shortest diameter)[195]. Data were presented as relative tumor volume (tumor volume at a given time point / initial tumor volume before 1st injection).

After completion of this therapeutic efficacy study on day 19, mice were sacrificed and tumor tissues and major organs were collected. The excised tumors were weighted separately and the inhibition ratio (IR) was calculated as $IR (\%) = [(W_c - W_t) / W_c] \times 100$. The W_c and W_t represent tumor weights for control group and each treatment group, respectively.

To further evaluate the anti-tumor efficacy of POEG-b-PVBIND/Dox and POEG-b-PVBIND micelles, tumors in each group were fixed in PBS solution containing 10% paraformaldehyde and sectioned into 4 μm slices. Tumor sections were stained with hematoxylin and eosin (H&E) for histopathological evaluation using a Zeiss Axiostar plus Microscope. Immunohistochemical analysis (IHC) of Ki67 protein was carried out using the labeled streptavidin-biotin method. Ki67 expression was quantified by calculating the number of Ki-67 positive cells/total number of cells in five randomly selected areas.

3.3.12 Quantification of Tumor-Infiltrating Lymphocytes

Tumor-infiltrating lymphocytes with various treatments were analyzed by flow cytometry. Female BALB/c mice bearing 4T1.2 tumor ($\sim 30 \text{ mm}^3$) were treated with free Dox, POEG-b-PVBIND, POEG-b-PVBIND/Dox micelles and POEG-b-PVB/Dox once every 3 days at a DOX dose of 5 mg/kg. Tumors were harvested and dipped into 1mL RPMI medium on ice one day following the last treatment. The tissues were cut into small pieces with scissors and 300-500ul Lysas Enzyme and 2ul DNase were added. Following a 30 min incubation, tumor pieces were further grinded into suspension with cover glass and were filtered using 100um Nylon Mash. Single cell suspensions were prepared and multi-parameter staining was used to identify the immune cell populations as follows: (i) CD8⁺T cells (CD45⁺ CD8⁺) and CD4⁺ T cells (CD45⁺ CD4⁺); (ii) Tregs (CD45⁺ CD4⁺ Foxp3⁺); (iii) Macrophage M1 type (CD11b⁺, F4/80⁺, CD206⁻) and Macrophage M2 type (CD45⁺ CD11b⁺, F4/80⁺, CD206⁺); and (iv) MDSC (CD45⁺, CD11b⁺, Gr-1⁺).

3.3.13 Safety Evaluation

To examine the potential toxicity of different treatments, weight changes throughout the in vivo experiments were monitored. In addition, serum and major organs were collected at the completion of the therapy experiment[196]. The organs were fixed with 4% (v/v) paraformaldehyde in PBS (pH 7.4), embedded in paraffin, and sectioned into 4 μ m slices[195]. Each section was processed for H&E staining and observed under a Zeiss Axiostar plus Microscope[197]. In addition, several biological markers for liver/kidney function were examined from the serum samples including alanine transaminase (ALT), aspartate transaminase (AST), alkaline phosphatase (ALP), blood urea nitrogen (BUN) and serum creatinine (SCr).

3.3.14 Statistical Analysis

Statistical analysis was performed with two-tailed unpaired Student's t-test between two groups. One-way analysis of variance (ANOVA) was performed for multiple groups, followed by Newman-Keuls test if $p < 0.05$. In all analysis, $p < 0.05$ was considered statistically significant and $p < 0.01$ was considered highly statistically significant.

3.4 Results and Discussion

3.4.1 Synthesis and Characterization of POEG-b-PVBIND Polymer

IND is a hydrophobic drug; however, it is difficult to be physically encapsulated into micelles[198, 199]. Conjugating IND with PEG to generate a “PEGylated prodrug” increased solubility of IND by forming micellar solution. However, each prodrug molecule can only carry one molecule of IND[200] and this prodrug is incapable of serving as a carrier for codelivery of other therapeutic agents. This has prompted us to design and synthesize an IND-based polymer with multiple units of IND moieties. We initially developed an IND-based polymer with a linear ethylene glycol vinyl ether linker that can carry 10 units of INDs (Figure 50). However, this carrier has limited capacity in formulating other hydrophobic agents. Aromatic groups were then introduced into this system to increase loading capacity of co-delivered agents through π - π interaction[201, 202]. To our best knowledge, this is the first IND-based nanocarrier that carries a number of INDs and, at the same time, is capable of codelivery of other hydrophobic agents (Table 5).

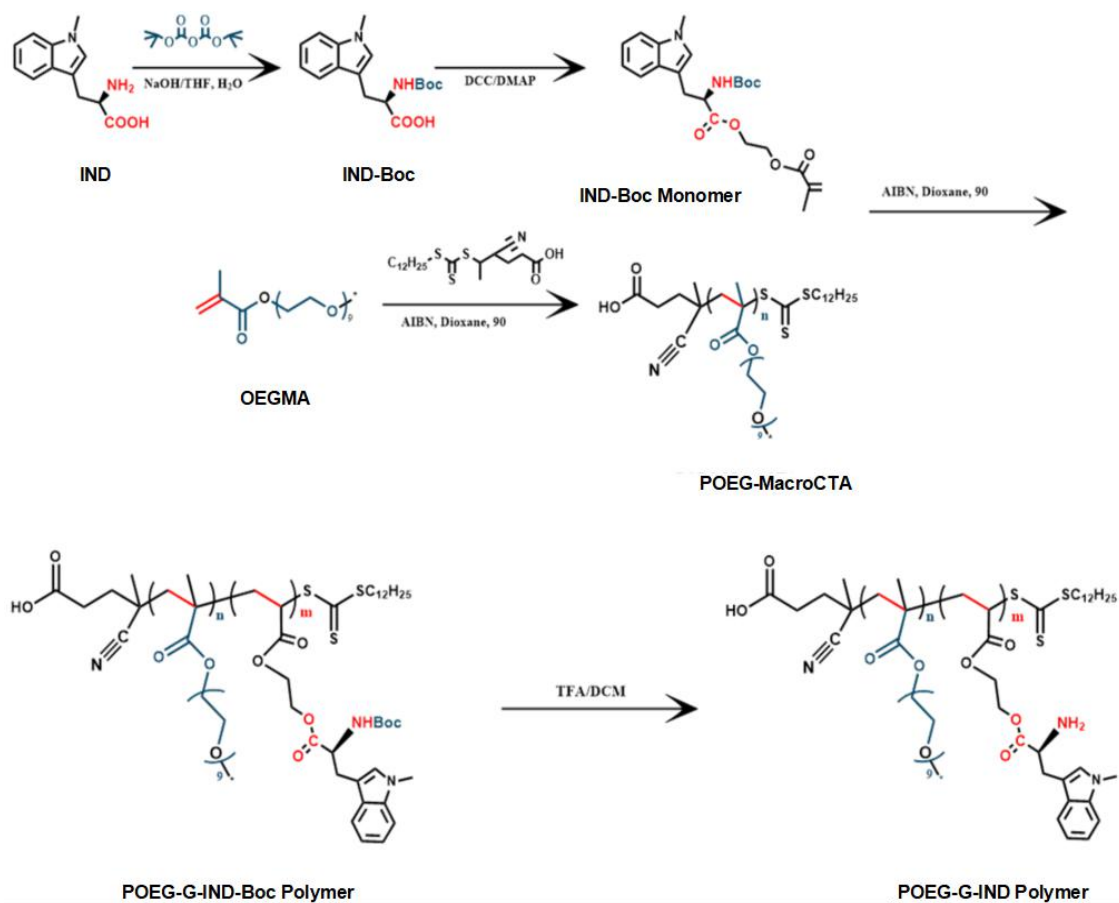


Figure 50 Synthesis scheme of POEG-G-IND polymer via RAFT polymerization.

Table 5 Biophysical characteristics of anticancer drug-loaded POEG-b-PVBIND micelles

Micelles	Mass ratio (mg:mg)	Particle Size ^a (nm)	DLC ^b (%)
POEG-b-PVBIND/Sunitinib	30:1	76.44	5.3
POEG-b-PVBIND/Daunorubicin	30:1	64.46	6.4

^a Measured by dynamic light scattering particle sizer.

^b DLC= DOX loading capacity.

The POEG-b-PVBIND polymer was obtained via several steps, as shown in Figure 51.

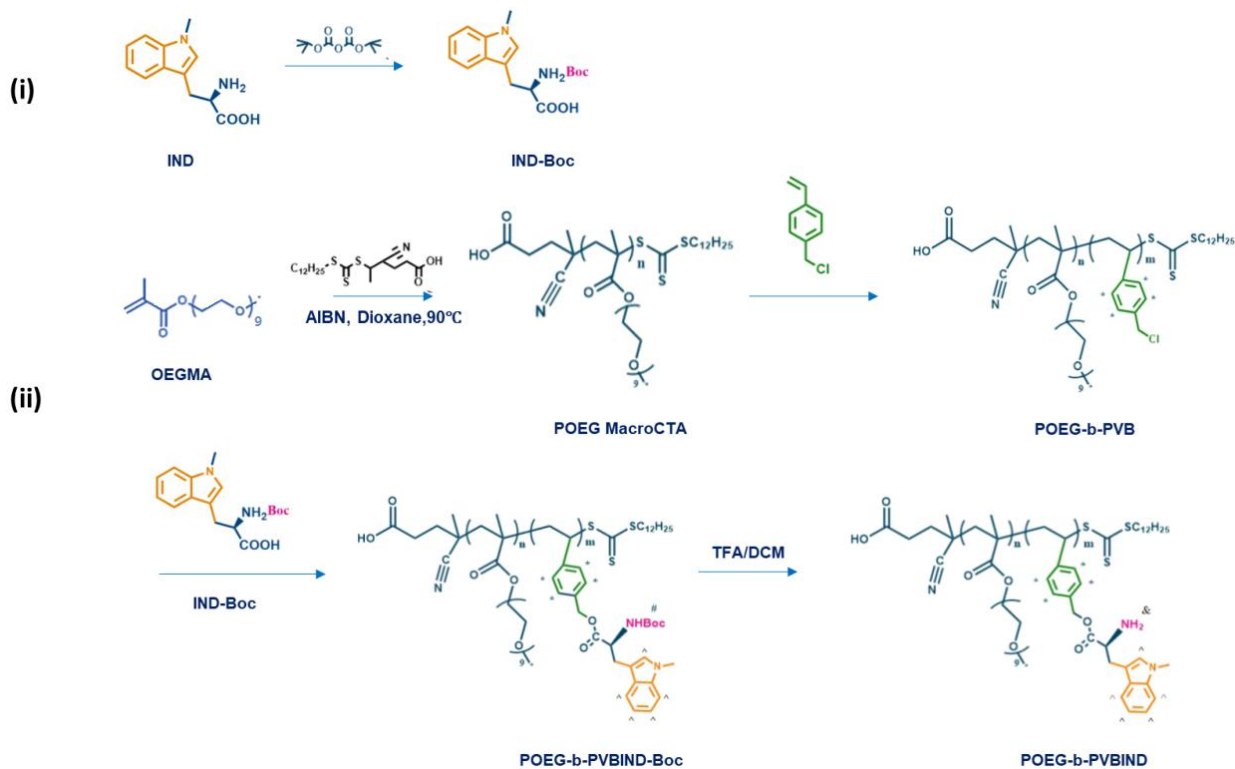


Figure 51 Synthesis of POEG-b-PVBIND polymer via RAFT polymerization and post-modification.

First, POEG macroCTA was synthesized by reversible addition-fragmentation transfer (RAFT) polymerization and the number of POEG units was calculated to be 17 (Figure 52 and Figure 53).

^1H NMR spectrum of POEG MacroCTA before purification (Figure 52) and after purification (Figure 53).

POEG macroCTA was then used to initiate the polymerization of vinylbenzyl chloride, yielding the amphiphilic POEG-b-PVB backbone. The number of repeated vinylbenzyl chloride units in the POEG-b-PVB backbone was calculated to be 10 based on the relative intensity ratio of the peaks at 6.0ppm-7.60ppm (**d**) and 3.35ppm (**a**) as shown in Figure 54.

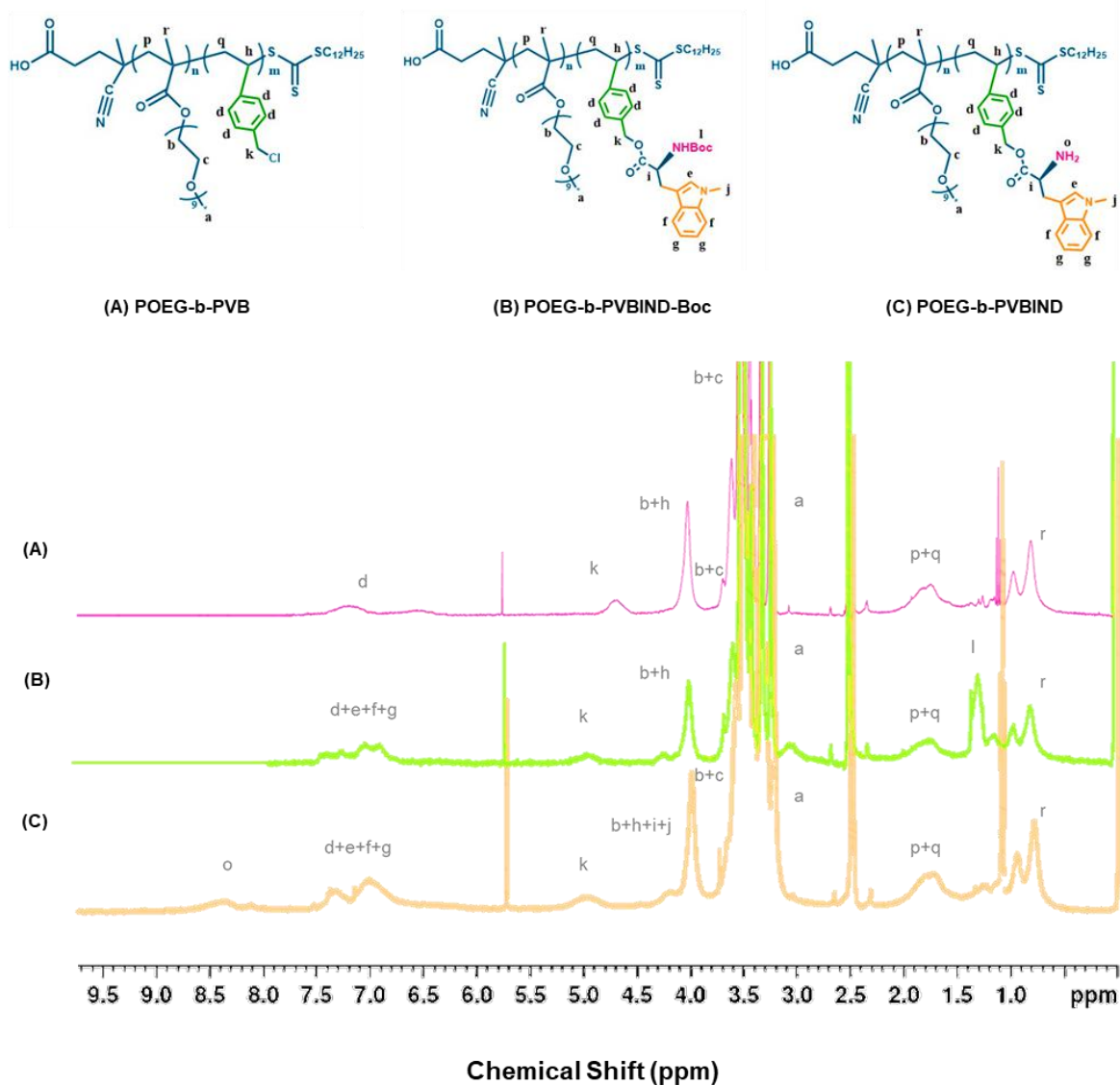


Figure 54 ¹H NMR spectrum of (A) POEG-b-PVB, (B) POEG-b-PVBIND-Boc, and (C) POEG-b-PVBIND polymers in DMSO.

The Boc-protected IND was synthesized (Figure 55) and conjugated to the POEG-b-PVB to afford POEG-b-PVBIND-Boc polymer.

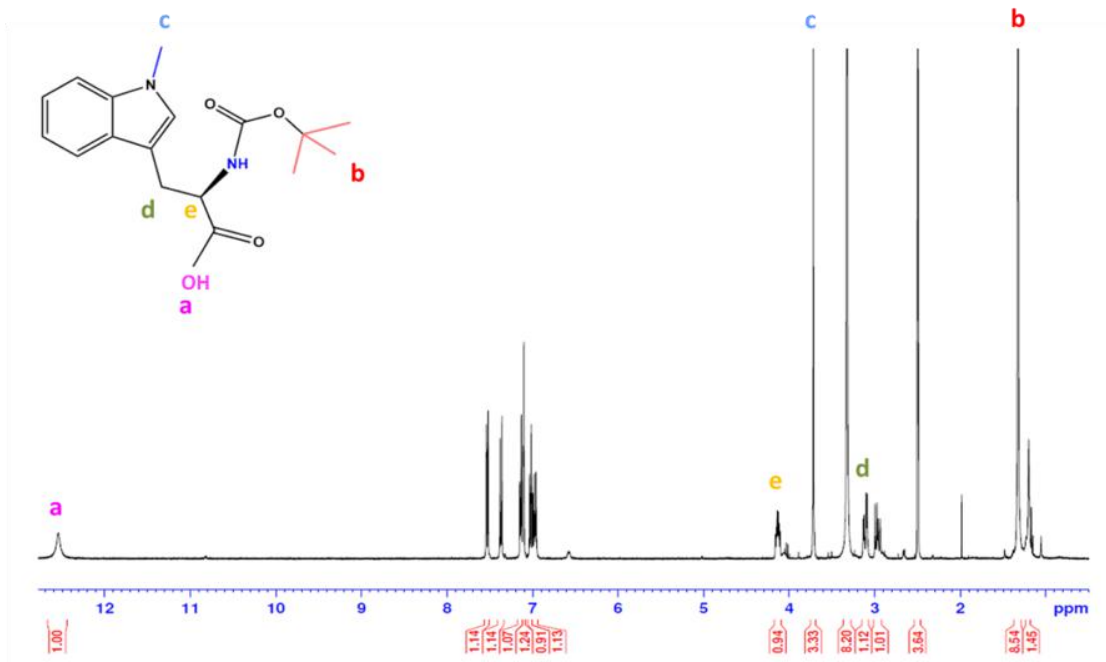


Figure 55 ¹H NMR Spectrum of Boc-Protected IND.

¹H NMR of IND-Boc (400Hz, DMSO): 12.54 (s, 1H), 7.30-7.40 (d, 1H), 7.50-7.60 (d, 1H), 7.10-7.20 (brm, 2H), 6.85-7.10 (brm, 2H), 4.10-4.20 (brm, 1H), 3.72 (s, 3H), 3.00-3.10 (brm, 1H), 2.80-3.00 (brm, 1H), 1.45-1.20 (brm, 9H).

The Boc-groups of the as-synthesized POEG-b-PVBIND-Boc polymer were deprotected in TFA/DCM solution to afford the POEG-b-PVBIND polymer. The chemical structures of POEG-b-PVB, POEG-b-PVBIND-Boc and POEG-b-PVBIND polymers were confirmed by ¹H NMR (Figure 54). The peaks at 3.35ppm (**a**) and 3.70ppm (**b**, **c**) were attributed to the hydrophilic POEG block of the polymer. The successful conjugation of IND-Boc to the polymer backbone was confirmed by the appearance of IND peaks at 6.30ppm-7.60ppm (**e**, **f**, **g**) and the Boc peak at 1.45 ppm (**h**) as shown in Figure 54B. After deprotection, amine-bearing POEG-b-

PVBIND polymer was obtained and de-protection of Boc group was confirmed by the disappearance of the peak at 1.45 ppm (Figure 54C). The number of IND per molecule of polymer was calculated to be 8. This indicated that the final ratio of benzyl chloride/IND after reaction was 5/4, suggesting that almost all the chloride groups in the polymer backbone were functionalized with IND. Also, IND loading content in the POEG-b-PVBIND polymeric prodrug carrier was calculated to be approximately 14.8% (w/w).

3.4.2 Physicochemical Characterization of POEG-b-PVBIND and Dox-Loaded Micelles

POEG-b-PVBIND polymer is an amphiphilic molecule. The outermost nontoxic PEGylation reduces adsorption of the serum proteins by the nanoparticles in physiological environment and increases the solubility of IND by forming micelles in aqueous solution. The hydrophobic anti-tumor agent Dox can be entrapped into the core of POEG-b-PVBIND micelles through π - π stacking and hydrophobic interaction among Dox, aromatic linker and IND. The POEG-b-PVBIND micelles and POEG-b-PVBIND/Dox micelles were prepared through a dialysis method. As shown in **Table 6** and Figure 56A, the prodrug polymer readily formed small-sized particles with an average hydrodynamic diameter of 17.90 ± 0.45 nm and a polydispersity index of 0.0246 ± 0.005 . The zeta potential was -1.23 ± 1.25 mv. Loading of Dox into the POEG-b-PVBIND micelles resulted in an increase in the particle size with an average hydrodynamic diameter of 50.83 ± 1.25 nm and a polydispersity index of 0.015 ± 0.007 . The Dox Loading Efficiency (DLE) and Dox Loading Capacity (DLC) were 72.1% and 8.4%, respectively. Loading of Dox had no impact on the zeta potential of the particles (-2.34 ± 2.48). Transmission electron microscopy (TEM) confirmed the homogeneously distributed spherical particles of

POEG-b-PVBIND micelles and POEG-b-PVBIND/Dox micelles with no aggregation (Figure 56B). Based on their biophysical properties, our newly developed polymeric micelles are expected to efficiently and selectively accumulate in the solid tumor through EPR effect[203].

Table 6 Biophysical Characterizations of blank and Dox-loaded POEG-b-PVBIND micelles.

Micelles	Size (nm) ^a	Zeta Potential (mv) ^a	PDI ^a	DLE (%) ^b	DLC (%) ^c	Stability ^d
POEG-b-PVBIND	17.90 ± 0.45	-1.23 ± 1.25	0.0246 ± 0.005	---	--	>60 days
POEG-b-PVBIND/Dox	50.83 ± 1.25	-2.34 ± 2.48	0.015 ± 0.007	72.1	8.4	28 days

^a Measured by dynamic light scattering particle sizer.

^b DLE = DOX loading efficiency.

^c DLC = DOX loading capacity.

^d T = 4 °C.

To examine the stability of POEG-b-PVBIND micelles upon dilution in blood stream, an important parameter for systemic delivery of particles to tumors, the critical micelle concentration (CMC) of POEG-b-PVBIND was determined using Nile red as a fluorescence probe. POEG-b-PVBIND micelles showed a low CMC of 0.00244 mg/ml, suggesting that they could maintain their stability after i.v. injection (Figure 56C). The colloidal stability of the micelles was further evaluated under 4 °C via following changes in sizes over time. POEG-b-PVBIND micelles alone could be stored at 4 °C for at least 60 days and Dox-loaded POEG-b-PVBIND micelle solution could be stored for at least 28 days without significant change in drug content and particle size, indicating their favorable stability in vitro[204] (**Table 6**).

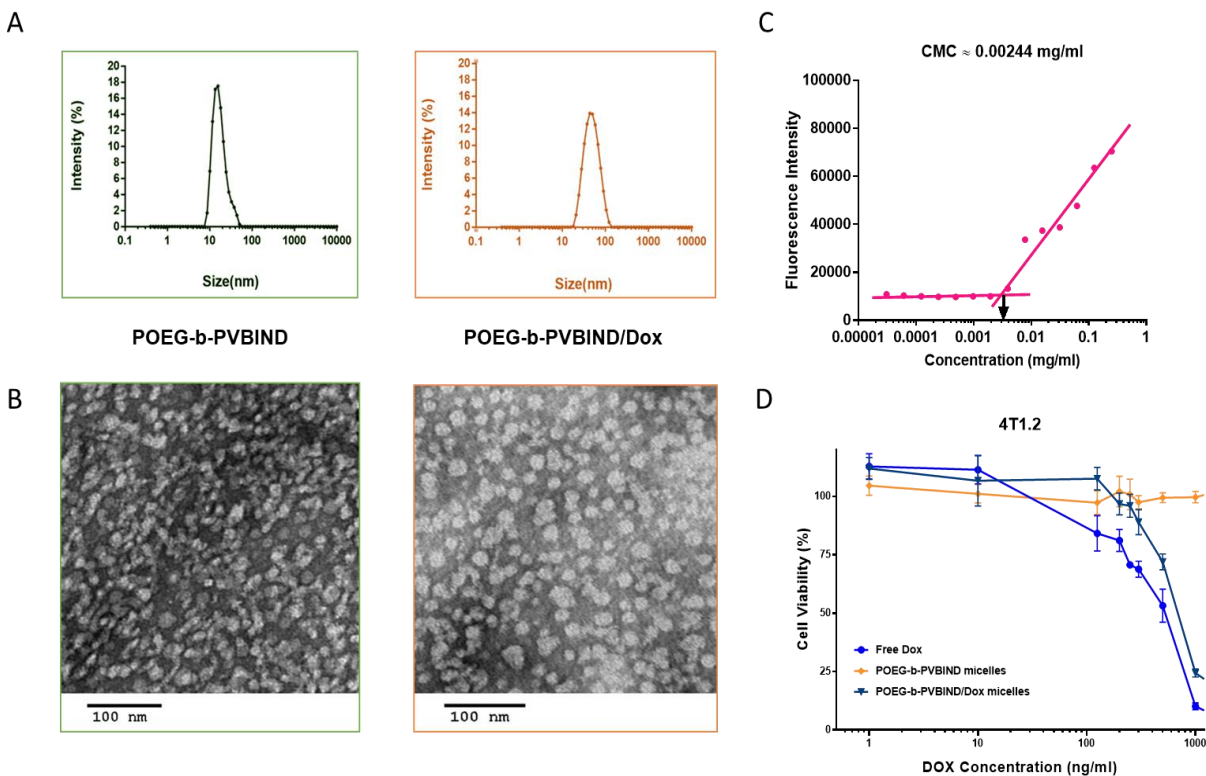


Figure 56 *In vitro* biophysical and biological characterizations of IND-based polymeric micelles.

(A) Size distribution and (B) TEM image of POEG-b-PVBIND micelles and POEG-b-PVBIND/Dox (carrier: drug, 35:1, w/w). Scale bar, 100nm; (C) Measurement of CMC of POEG-b-PVBIND micelles. (D) Cytotoxicity of POEG-b-PVBIND micelle, free Dox, and POEG-b-PVBIND/Dox against a mouse breast cancer cell line (4T1.2). Cells were treated for 72h and cytotoxicity was determined by MTT assay. Data are presented as means \pm SD (n =5).

The kinetic profile of Dox release from POEG-b-PVBIND/Dox was also tested. Free Dox was rapidly diffused across the dialysis bag with greater than 80% being diffused out of dialysis bag within 5h. In contrast, only 21% of Dox was detected outside the dialysis bag within 24h, indicating a good stability of POEG-b-PVBIND/Dox without burst drug release under physiological environment (Figure 57).

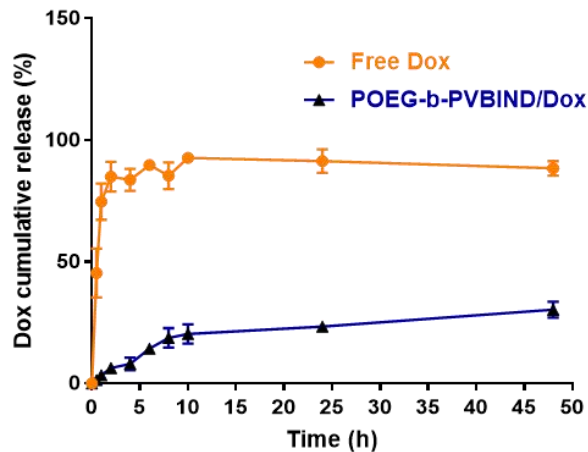


Figure 57 DOX release profiles of DOX-loaded POEG-b-PVBIND micelles

DOX release profiles of DOX-loaded POEG-b-PVBIND micelles with free DOX as the control. PBS containing 0.5% (w/v) Tween 80 was used as the release medium. Data are presented as means \pm SD (n=3).

The release of IND from POEG-b-PVBIND in PBS followed a much slower kinetics and less than 5% of released IND was detected over 24h. However, the release of IND was accelerated following exposure to esterases (Figure 58). Nonetheless, only 15% of IND was released after 24 h, suggesting that IND was slowly released over a prolonged period of time following delivery to the tumors.

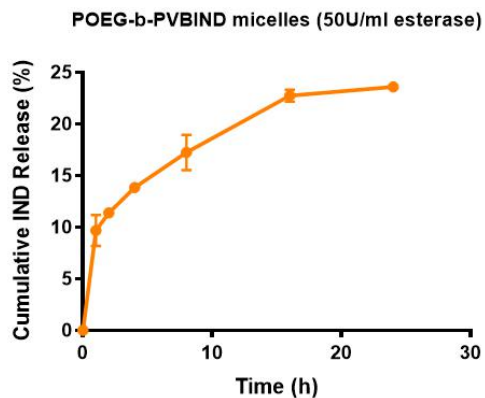


Figure 58 Release profile of IND from POEG-b-PVBIND in presence of esterase.

The release of IND from POEG-b-PVBIND in PBS in presence of esterase was analyzed to evaluate the release rate of IND (0, 1, 2, 4, 8, 16, 24 hours). The released IND was derivatized with 6-aminoquinolyl-n-hydroxysuccinimidyl carbamate and measured by UPLC-QTOFMS5 analysis.

The cytotoxicity of free Dox, POEG-b-PVBIND micelles and POEG-b-PVBIND/Dox micelles against 4T1.2 cells was determined by MTT assay (Figure 56D). POEG-b-PVBIND micelles alone were not effective in inhibiting the proliferation of 4T1.2 tumor cells at our test concentrations while free Dox and Dox-loaded POEG-b-PVBIND micelles inhibited 4T1.2 cell proliferation in a concentration-dependent manner. Dox-loaded POEG-b-PVBIND micelles were less effective than free Dox, which is likely due to incomplete release of Dox over a short period of treatment as supported by the data from the release study (Figure 56C).

3.4.3 *In Vivo* Distribution of POEG-b-PVBIND Micelles

The tumor targeting efficiency of POEG-b-PVBIND micelles was investigated in a 4T1.2-bearing mouse model using DiR as a fluorescence probe[205]. First, the DiR-loaded

POEG-b-PVBIND micelles were prepared and intravenously injected into the mice for in vivo imaging. The DiR-loaded POEG-b-PVBIND micelles were comparable to Dox-loaded POEG-b-PVBIND micelles in size (53.01 vs. 50.83 nm) (Figure 59). Figure 61A and Figure 61B showed that enhanced distribution of DiR-loaded POEG-b-PVBIND micelles was clearly observed at 12h and the fluorescence intensity continued to increase up to 36h post-injection. In contrast, free DiR was widely distributed in the mice with no obviously enhanced accumulation at the tumor sites at all time points examined.

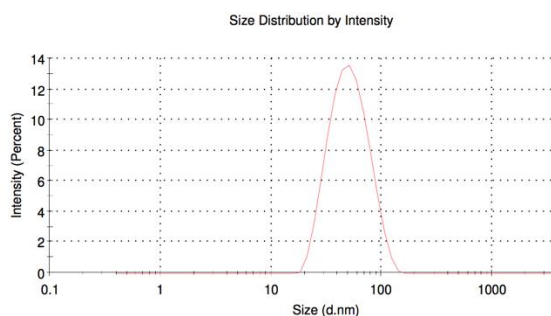


Figure 59 Characterization of DiR-loaded POEG-b-PVB micelles.

The size of DiR-loaded POEG-b-PVB micelles was characterized by DLS, with an average hydrodynamic diameter of 53.01 nm and a polydispersity index of 0.301. The zeta potential was 2.36 mV.

The accumulation of fluorescence in tumors and other major organs (heart, lung, liver, spleen and kidneys) was further examined by *ex vivo* imaging at 24 h post-injection. As shown in Figure 61C & Figure 61D, the signals in normal organs were significantly higher or comparable to those in tumor tissues for free DiR. Particularly, high accumulation of free DiR was observed in the lung. As a quaternary ammonium salt, DiR carries a positive charge at the N atom under physiological pH. The effective accumulation in the lung is likely due to the interaction of the quaternary amine motif of DiR with the negatively charged cell membrane in

the lung. Amine-containing basic compounds have been reported to be predominantly accumulated in the lung due to the effective binding to acidic phospholipids on the cell membrane, which is abundantly distributed in lung tissue[206-210]. In contrast, the signals of DiR-loaded POEG-b-PVBIND in tumor tissues were significantly higher than those in all normal organs examined, which was consistent with the data in Figure 61A. This indicates that the tumor-targeting ability of POEG-b-PVBIND micelles helps to reduce the distribution of their loaded agents in normal tissues, which shall help to reduce their toxicity in normal organs.

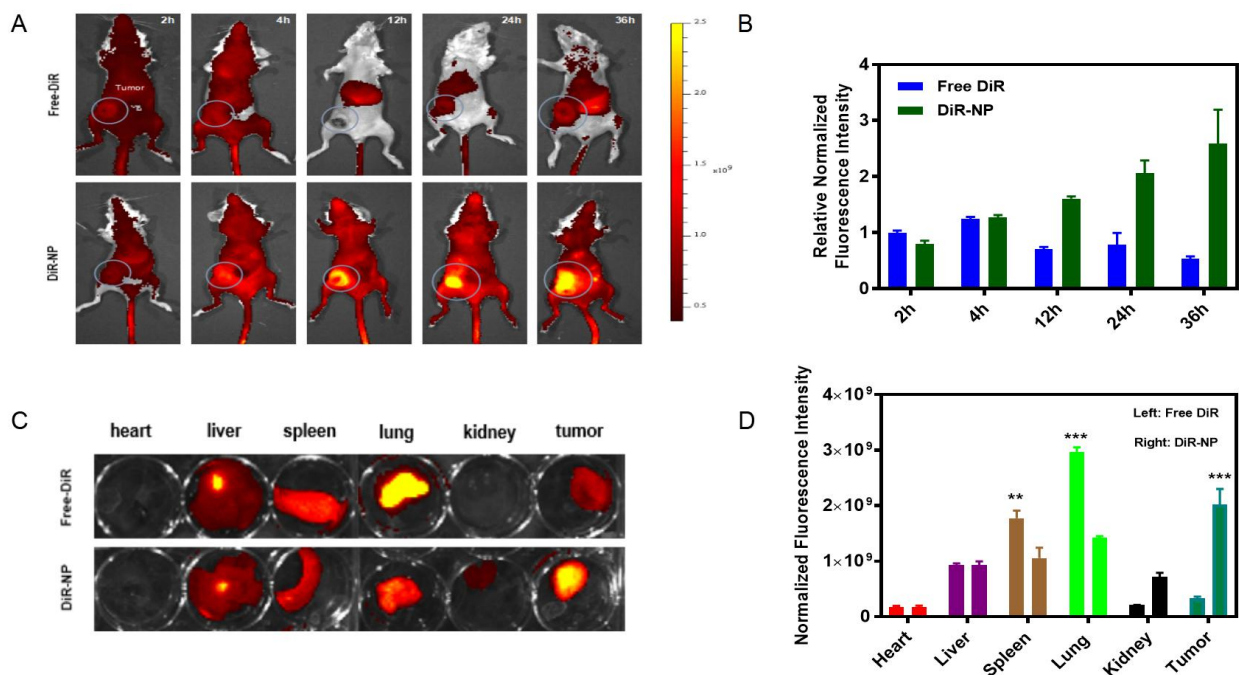


Figure 60 Tumor accumulation of NPs in a subcutaneous xenograft mouse model (4T1.2).

(A) Near-infrared images of mice at 2, 4, 12, 24, 36 h post-injection of free DiR and DiR-NP; (B) Fluorescence intensities of tumors at different time points (n=3, mean ± SD); (C) Ex vivo fluorescence imaging of major organs and tumors 24 hours following injection of free DiR and DiR-NP; and (D) Relative normalized fluorescence intensity of major organs and tumors after 24 hours (n=3, mean ± SD).

To examine whether POEG-b-PVBIND micelles can similarly deliver Dox to the tumors, the distribution of Dox in tumor tissues was examined by analyzing frozen tissue sections 24 h following injection of free Dox or Dox-loaded POEG-b-PVBIND micelles. As shown in Figure 62A and Figure 62B, much more signals of Dox were found in tumor tissues treated with Dox-loaded POEG-b-PVBIND micelles compared to free Dox. It is also apparent that POEG-b-PVBIND and POEG-b-PVB were comparable in selective delivery of Dox to tumor tissues.

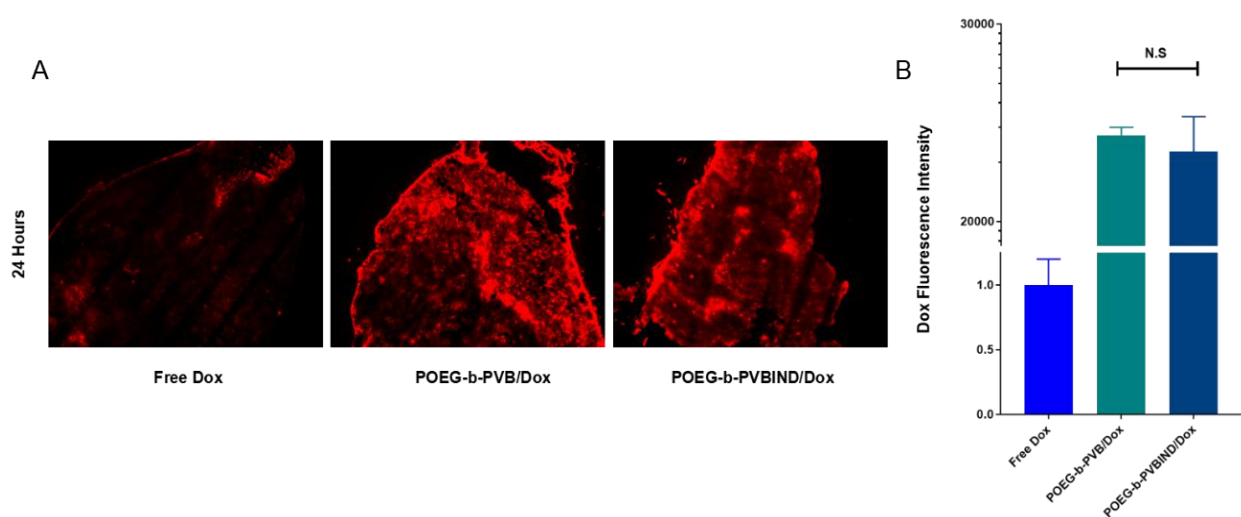


Figure 61 The distribution of Dox fluorescence in tumor tissues

(A) The distribution of Dox fluorescence in tumor tissues 24 hours following i.v. administration of free Dox, POEG-b-PVB/Dox or POEG-b-PVBIND/Dox after (Magnification $\times 40$, scale bar = 50 μm), the dose of Dox was 5 mg/kg; (B) Five randomly selected microscopic fields were quantitatively analyzed using image J, the results are displayed as mean \pm S.D. (error bars).

Taken together, the above data indicate that POEG-b-PVBIND micelles demonstrated effective passive targeting to tumors via EPR effect, which resulted in higher accumulation of Dox and IND in the tumor site. This might be attributed to the PEGylation on the surface of POEG-b-PVBIND micelles, which ensures a long circulation time for them to permeate into

tumor sites. Meanwhile, the small size (~50 nm) of POEG-b-PVBIND micelles might also contribute to the effective accumulation at the tumor site[211, 212].

3.4.4 *In Vivo* Therapeutic Efficacy

The antitumor efficacy of the IND prodrug-based nanocarrier was examined in an orthotopic syngeneic murine breast cancer model (4T1.2). BALB/c mice bearing tumors of 30 mm³ in size were i.v. administered with saline, free Dox, POEG-b-PVBIND micelles, POEG-b-PVBIND/Dox, and POEG-b-PVB/Dox at a Dox dose of 5mg/kg and an equivalent IND dose of 20mg/kg on days 0, 3 and 6, respectively (Figure 62A). POEG-b-PVBIND micelles alone showed significant antitumor activity compared to the control mice that received only the saline treatment (Figure 62B and Figure 62C), which might be attributed to the immune response activated by the released IND as shown later.

Free Dox only showed a modest effect in inhibiting the growth of 4T1.2 tumor. However, loading of Dox into POEG-b-PVBIND micelles led to a significant improvement in antitumor activity, much more effectively than either free Dox or POEG-b-PVBIND micelles alone. It is worth noting that POEG-b-PVBIND/Dox micelles were also more effective than POEG-b-PVB/Dox (Figure 62B and Figure 62C). This is unlikely due to a more effective delivery of DOX by the POEG-b-PVBIND/Dox formulation as both formulations showed similar particle sizes (50.83 vs. 49.63 nm) (Figure 63) and they are comparable in the efficiency of delivery as shown by similar levels of Dox fluorescence intensity in tumors following delivery via POEG-b-PVB micelles or POEG-b-PVBIND micelles (Figure 61A and Figure 61B). The observed

activity of the POEG-b-PVBIND/DOX was likely attributed to both direct effect of chemotherapy on cancer cells and enhanced immuno-microenvironment from DOX/IND. In particular, the enhanced delivery of both DOX and IND through the POEG-b-PVBIND-based nanocarrier plays an important role in the enhanced antitumor activity.

We further examined the tumor histology at the end of drug treatment. As shown in Figure 62D (upper), H&E-stained tumor sections in the saline-treated group showed typical high density of tumor cells with large nuclei. However, the tumor sections in other treatments showed areas of necrosis. In addition, altered morphology of cancer cells with shrunk nuclei and cell damage was observed as well. Among all the five treatment groups, POEG-b-PVBIND/Dox micelles exhibited the most significant intra-tumor tissue damage.

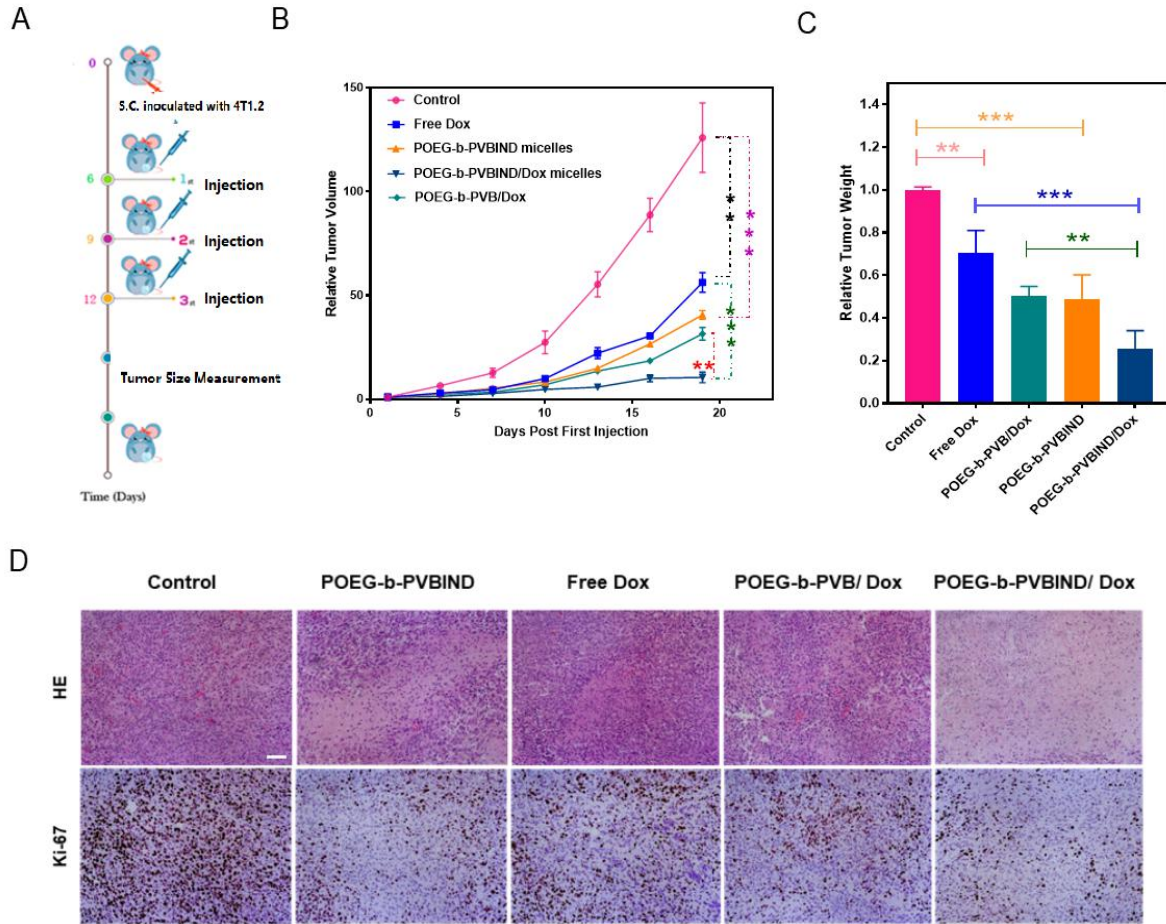


Figure 62 The evaluation of in vivo antitumor efficiency.

(A) Schematic representation of experimental design; (B) In vivo antitumor activity of various formulations in 4T1.2 tumor model. Dox does was 5mg/kg and IND does was 20mg/kg. Tumor sizes were plotted as relative tumor volumes; (C) Relative tumor weights at the end point (* $P < 0.05$; ** $P < 0.01$; *** $P < 0.005$, $n=5$); (D) Representative photomicrographs of tumors with H&E (upper) and Ki-67 immunohistochemical (bottom) staining (Magnification $\times 200$, scale bar = 50 μm).

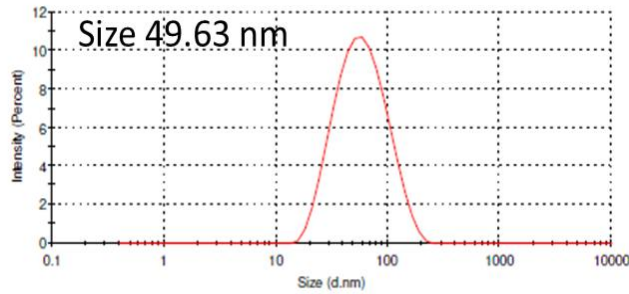


Figure 63 Size distribution of POEG-b-PVB micelles/Dox. (carrier: drug, 20:1, w/w)

We also performed immuno-histochemical (IHC) staining of Ki-67 protein to further evaluate the extent of tumor cell proliferation. As shown in Figure 62D (**bottom**) and Figure 64, POEG-b-PVBIND/Dox micelles-treated group exhibited the lowest level of Ki-67 expression, indicating significantly reduced tumor cell proliferation compared with other treatments. The results of histology and Ki-67 studies were consistent with those of tumor volume measurements.

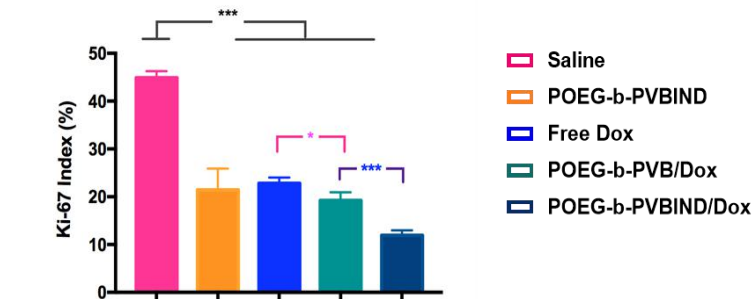


Figure 64 Expression of Ki-67 protein in tumor tissues following various treatments.

Five randomly selected microscopic fields were quantitatively analyzed using ImmunoRatio and the results are displayed as mean \pm S.D. (error bars).

3.4.5 Antitumor Immune Response *in Vivo*

To delineate a role of immune response in the POEG-b-PVBIND/DOX-mediated antitumor activity, the immune cell populations in the tumor tissues with various treatments were analyzed and compared by flow cytometry 10-days after various treatments. Figure 65A (i) shows that the total percentage of immune cells (CD45⁺) was significantly increased in the tumors treated with POEG-b-PVBIND alone or POEG-b-PVBIND/Dox. The number of immune cells was also increased in the group treated with Dox alone or POEG-b-PVB/DOX although it was not statistically significant (Figure 65B (i)).

Figure 65A and Figure 65B (ii) shows that the percentages of both CD4⁺ T and CD8⁺ T cells were significantly increased in the tumors treated with POEG-b-PVBIND micelles, alone or loaded with Dox. Treatment with free Dox or POEG-b-PVB/Dox micelles also led to a slight increase in the number of CD8⁺ T cells. In contrast, the numbers of Treg cells were significantly decreased by all of the treatments, particularly POEG-b-PVBIND micelles alone or POEG-b-PVBIND/Dox micelles (Figure 65A and Figure 65B (iii)). Accordingly, the ratios of CD8⁺ T cells/Treg cells were significantly increased in all of the treatments especially POEG-b-PVBIND micelles alone or POEG-b-PVBIND/Dox micelles (Figure 65B (iv)).

Figure 65C shows that free Dox was highly effective in increasing the number of functional CD8 cells (IFN- γ -producing CD8⁺ T cells). Similar effects were observed for Dox loaded in POEG-b-PVB or POEG-b-PVBIND/Dox micelles. Treatment with POEG-b-PVBIND

micelles alone led to a slight increase in the number of IFN- γ -producing CD8⁺ T cells; however, it is not statistically significant.

MDSCs are highly immunosuppressive and play an important role in inhibiting the antitumor immunity[213]. Figure 65D shows that the number of MDSCs was significantly reduced in the tumor following treatment with POEG-b-PVBIND micelles alone. Treatment with POEG-b-PVBIND/Dox micelles also led to a significant decrease in the percentages of MDSCs, but less dramatically compared to the treatment by POEG-b-PVBIND micelle alone.

Overall, our results were consistent with the notion that Dox is a potent ICD drug and can induce antitumor immunity in addition to a direct killing effect on tumor cells. Our data also clearly showed that the IND prodrug-based carrier was highly effective in promoting an immuno-active tumor microenvironment. The significantly improved antitumor activity of POEG-b-PVBIND/Dox compared to other treatments is likely due to both the tumoricidal effect of Dox and a strong antitumor immune response that is potentiated by the IND following release from the POEG-b-PVBIND micelles.

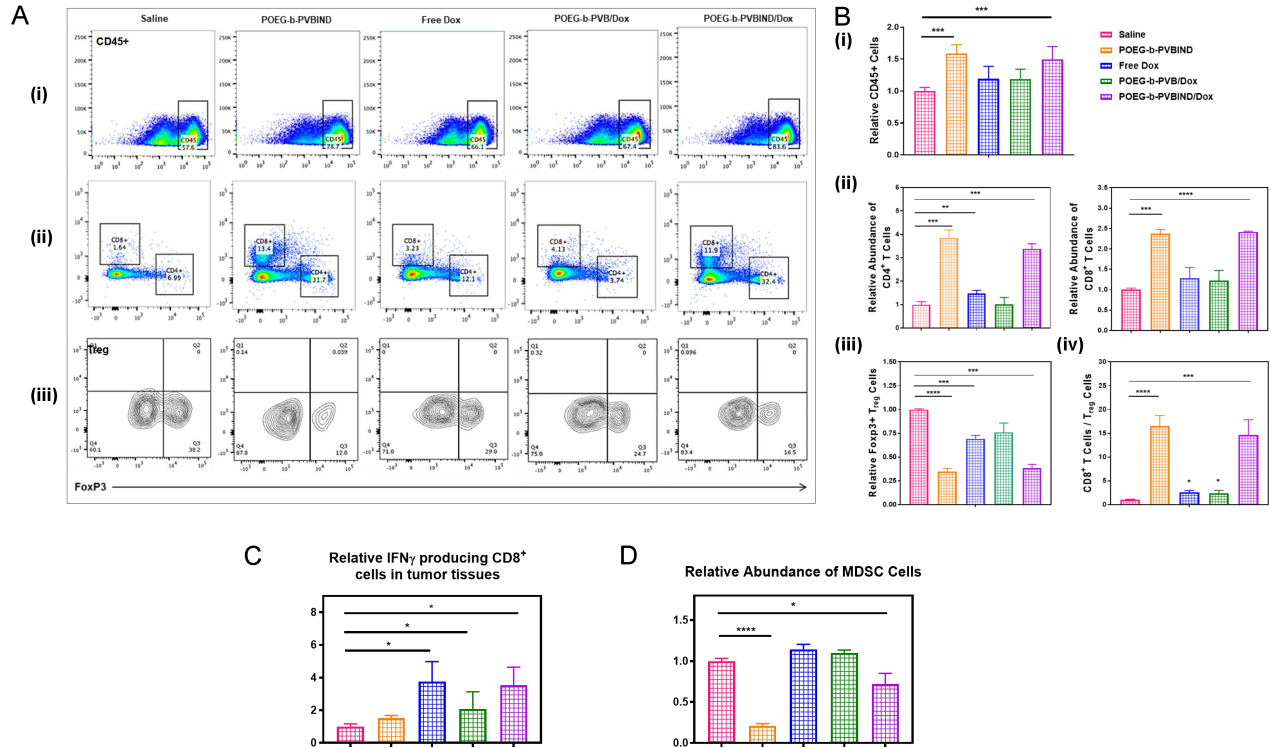


Figure 65 In vivo antitumor immune response after various treatments.

(A, B) Representative flow cytometric plots and percentages of CD4⁺ T cells (i) and CD8⁺ T cells (ii) within the CD45⁺ population (i); FoxP3⁺ T regulatory cells within CD4⁺ T cells (iii) in the tumor microenvironment; and ratios of CD8⁺ T cells vs. T regulatory cells (iv). Percentages of (C) IFN- γ -producing CD8⁺ T cells, and (D) Myeloid-derived suppressor cells (MDSCs) in the tumor tissues. Data depict mean \pm S.D., values were analyzed by two-tailed Student's t-test. (*P < 0.05; ** P < 0.01; *** P < 0.005)

3.4.6 Safety Evaluations

Figure 66A shows the changes in body weights of mice receiving different treatments throughout the therapy study. There were no significant differences in the body weights between control group and other treatment groups although mice receiving free Dox appeared to gain less weight. In addition, serum levels of aspartate transaminase (AST), alanine transaminase (ALT),

alkaline phosphatase (ALP), and creatinine (SCr) were all within the normal ranges, suggesting minimal impact of the different treatments on the hepatic and renal functions (Figure 66B and Figure 66C). Finally, no obvious changes in histology were found for all of the major organs examined including heart, liver, spleen, lung and kidney in mice receiving different treatments (Figure 66D). These data suggest the excellent safety of the POEG-b-PVBIND/Dox at a dose that demonstrated significant therapeutic efficacy.

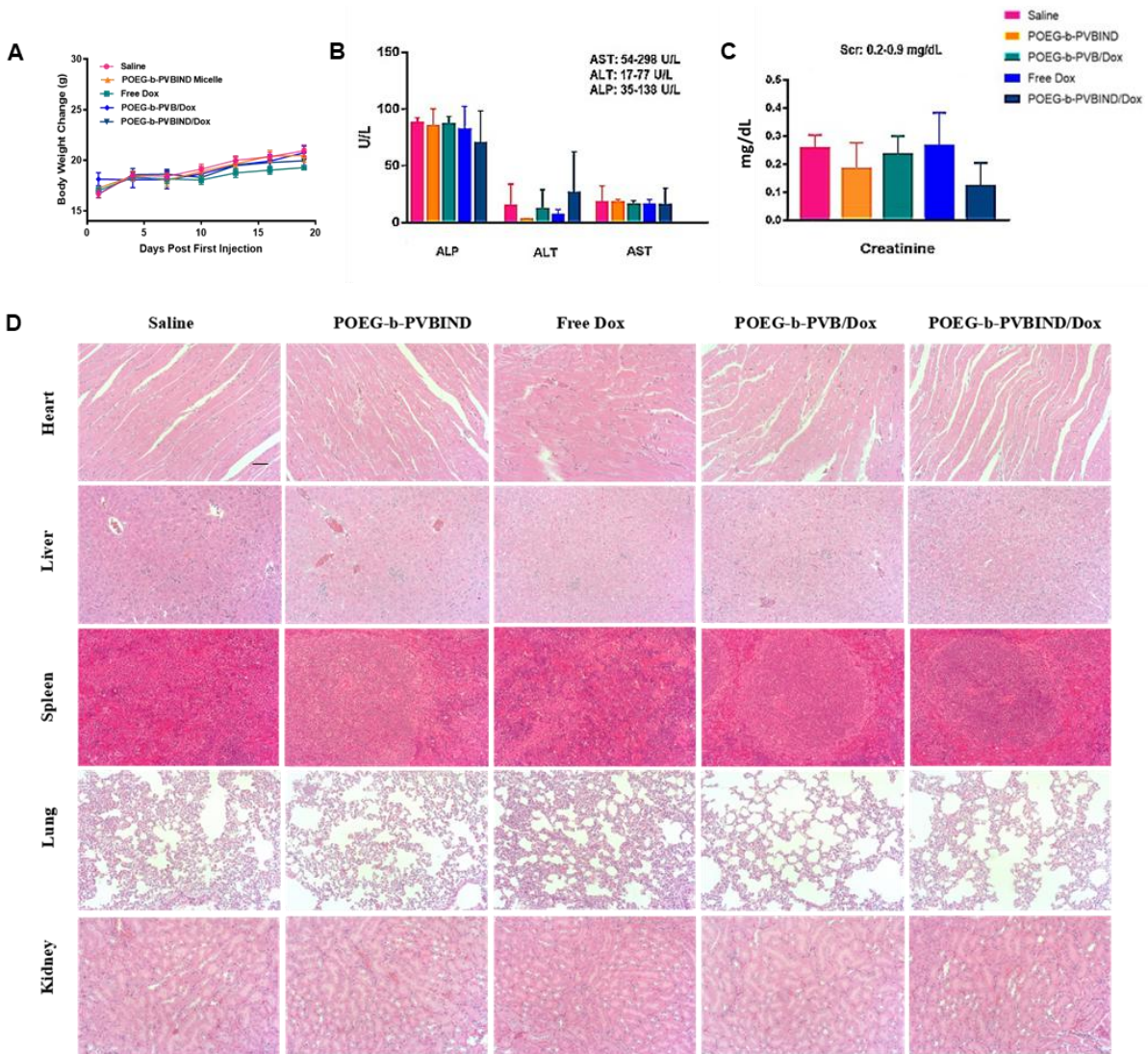


Figure 66 Safety evaluations.

(A) Body weight change (B) Liver and (C) Kidney function assays after various treatments. Results were expressed as the mean \pm S.D. (n=5); The normal ranges for all the biochemical parameters are shown in the upper right corner of panels (B) and (C); (D) Representative photomicrographs of heart, liver, spleen, lung and kidney with H&E staining (Magnification $\times 200$).

3.5 Conclusions

We have developed a new, IND prodrug-based micellar system, POEG-b-PVBIND that can achieve codelivery of IND and a hydrophobic chemotherapeutic agent such as Dox. Compared to our previous PEG-Fmoc-NLG919-based carrier, POEG-b-PVBIND allows incorporation of 8 units of immunostimulatory moieties instead of 1. POEG-b-PVBIND can realize controlled release of both conjugated drugs (IND) and encapsulated drugs (Dox). Dox was encapsulated in the hydrophobic core of micelles via hydrophobic interaction (intermolecular forces). IND was introduced into POEG-b-PVBIND micelles via a covalent bond (intramolecular forces). Intermolecular forces are weaker than intramolecular forces. Because of this, Dox has a much faster rate of release compared with that of IND. The relatively rapid release of Dox shall lead to the first round of anti-tumor response. In addition to direct effect on cancer cells, Dox also induces immune response due to enhanced antigen presentation following killing of tumor cells. Meanwhile, the slower release of active IND from the prodrug helps to sustain or enhance the magnitude of immune responses by reversing the suppressive immune microenvironment. The improved delivery together with the combination action between IND and DOX plays an important role in the enhanced overall antitumor activity.

4.0 Summary and Perspectives

The immunosuppressive TME represents one of the hallmarks of cancer and underlies the basis for immune evasion and acquired immunotherapy-resistance for cancer therapy. Significant clinical success has been made in cancer treatment through blocking the T cell checkpoints, such as CTLA-4 and PD-1. However, only a subset of patients benefit from such approaches. The reason of non-response is very complicated. On the one hand, additional immunosuppressive mechanisms exist in the TME. A better understanding of the mechanism that regulates the immunosuppressive TME plays a crucial role for developing more efficacious immunotherapies and combination strategies. On the other hand, the use of the free drug raises the issue of water-solubility, rapid blood elimination and metabolism. Improvement in drug bioavailability and/or codelivery of multiple drugs via a nanocarrier represents a promising strategy to improve the therapeutic outcome and patient compliance.

During my graduate study, I worked on identifying potential therapeutic targets and worked on several projects to develop multifunctional nanocarrier systems for the combinational co-delivery of anti-cancer agents for cancer immunotherapy. As described in Chapter II, we investigated the therapeutic potential of GRM4 in cancer immunotherapy. At the beginning, we found that male *Grm4^{-/-}* mice demonstrated markedly delayed tumor growth in the setting of different murine cancer model (B16, 3LL, and MC38). However, no significant difference was observed in tumor growth in the female littermates, which indicates the gender difference of GRM4 in the context of tumor. A signature of $\text{NK}^{\text{high}}\text{-GRM4}^{\text{low}}$ and/or $\text{CD8}^{\text{high}}\text{-GRM4}^{\text{low}}$ in human tumor samples is of clinical significance in predicting the prognosis of cancer patients

and gender difference has also been revalidated in the patient sample. These results highlight the clinical significance of studying the function role of GRM4 in cancer.

Pharmacological inhibition of GRM4 with MSOP led to similar results in the three tumor models in *Grm4*^{+/+} mice. In addition, the tumor inhibitory effect of MSOP was abolished in *Grm4*^{-/-} mice, suggesting a role of GRM4 in MSOP-mediated antitumor activity. The drawback of MSOP is its short half-life in blood which necessitates frequent dosing and limits its translation into clinic. Nanoparticles (NPs) are known to improve the half-life of the formulated drugs in blood and enhance their delivery to tumors. As MSOP bears a phosphate group (ionic group), calcium phosphate NPs represent a simple and highly effective system to improve its *in vivo* delivery. Our developed NPs demonstrated significant improved therapeutic efficacy in B16 murine tumor model compared with free MSOP. The toxicity of MSOP-NPs has also been well-characterized, which indicates the safety of our designed formulation. These data strongly suggest that GRM4 is a druggable target for clinical translation.

Mechanistically, genetic knockout of *Grm4* in B16 tumor model led to significant enrichment of numerous immune-related pathways in B16 tumor microenvironment. It is interesting to note that both NK cells and CD8⁺ T cells in tumor tissues were significantly increased in *Grm4*^{-/-} mice and these immune cells are of highly active and proliferative phenotype. Both NK and CD8⁺ T cells are critically involved in the antitumor activity in *Grm4*^{-/-} mice as neutralizing antibody for each subpopulation drastically attenuated the tumor inhibitory effect. The NK cells may be associated with the tumor growth suppression at early phase after

tumor inoculation while the cellular immunity plays an important role in controlling the tumor growth at a late stage.

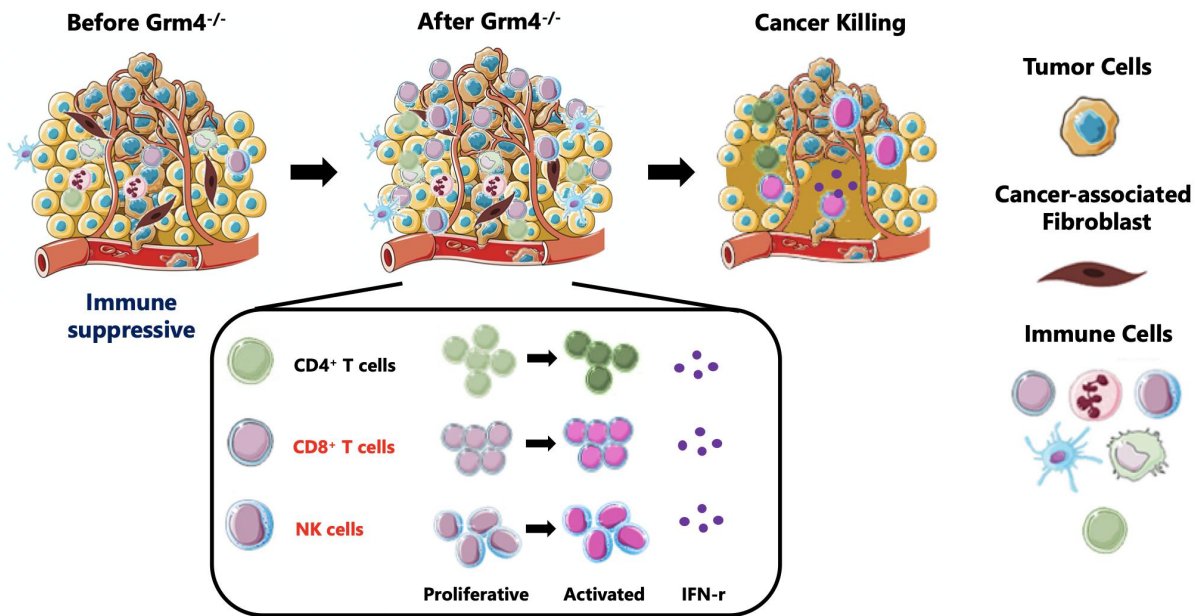


Figure 67 Summary of GRM4^{-/-} Mediated Anti-tumorImmunity.

Single-cell RNA-sequencing and T Cell Receptor (TCR) profiling further defined the clonal expansion and immune landscape changes in CD8⁺ T cells. Grm4^{-/-} intrinsically activated IFN- γ production in CD8⁺ T cells through cAMP/CREB-mediated pathway. ScRNA-Seq suggests that *Grm4^{-/-}* prevented CD8⁺ T cells from entering into an exhausted state and preferentially increased the proliferative and activated functionality in the sub-cluster of CD8-C7-Itgb1 that is highly active in producing IFN- γ . ScTCR profiling suggests that CD8⁺ T cells of different clusters are not completely independent but might undergo extensive state transitions. Similar changes in immune subpopulations were observed in B16-bearing *Grm4^{+/+}* mice treated with MSOP, further establishing a role of GRM4 in modulating antitumor immunity.

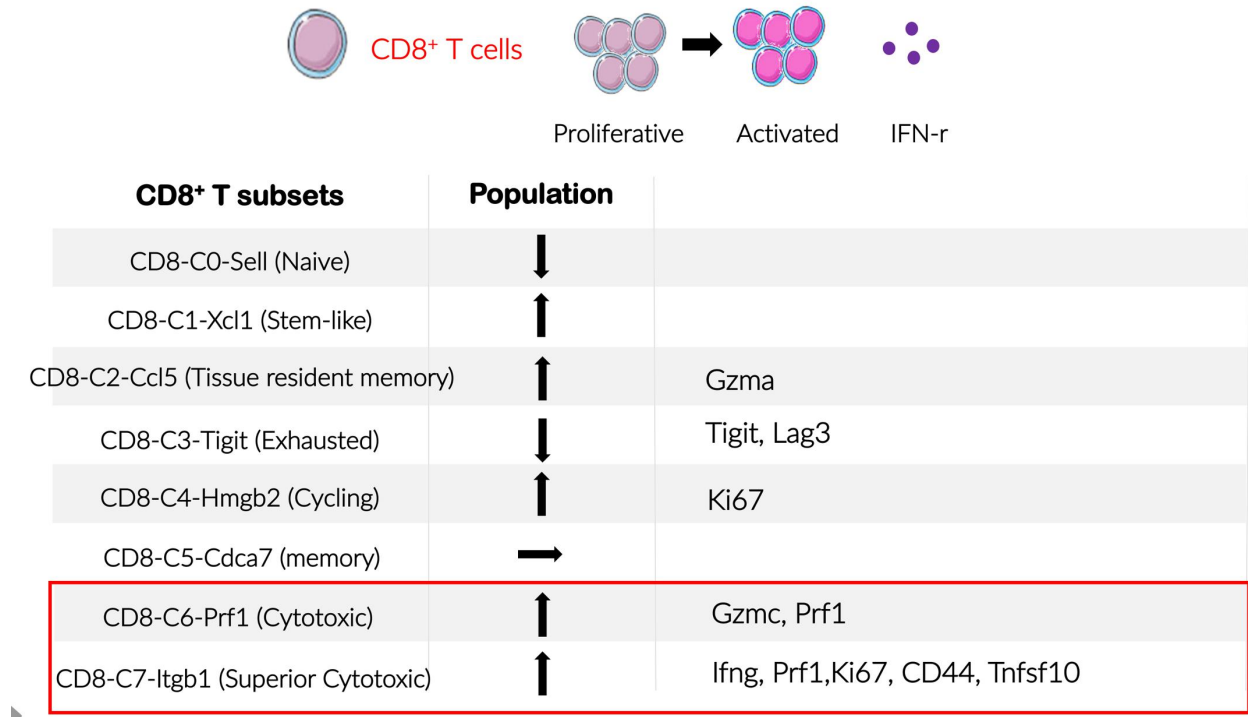


Figure 68 Summary of How GRM4^{-/-} Shape CD8⁺ T Landscape

The immune-active TME following *Grm4* knockout was also associated with induction of adaptive immune resistance characterized by upregulation of PD-1 and CTLA-4 signaling. Upregulation of PD-1 and CTLA-4 was similarly observed following MSOP treatment. The induction of adaptive immune resistance is likely attributed, at least partially, to the enhanced IFN- γ response, which was further confirmed by scRNA-seq results. This suggests an opportunity of further improving the antitumor activity through combining the inhibition of GRM4 signaling with anti-PD-1 or CTLA-4-based ICB. Indeed, treatment with anti-PD-1 or CTLA-4 antibody led to more drastic inhibition of the growth of B16 tumor in *Grm4*^{-/-} mice. More importantly, the improvement in antitumor response was similarly achieved in *Grm4*^{+/+}

mice through combination of a pharmacological inhibitor (MSOP) with anti-PD-1 or CTLA-4 monoclonal antibody, suggesting a potential combination regimen in clinical translation.

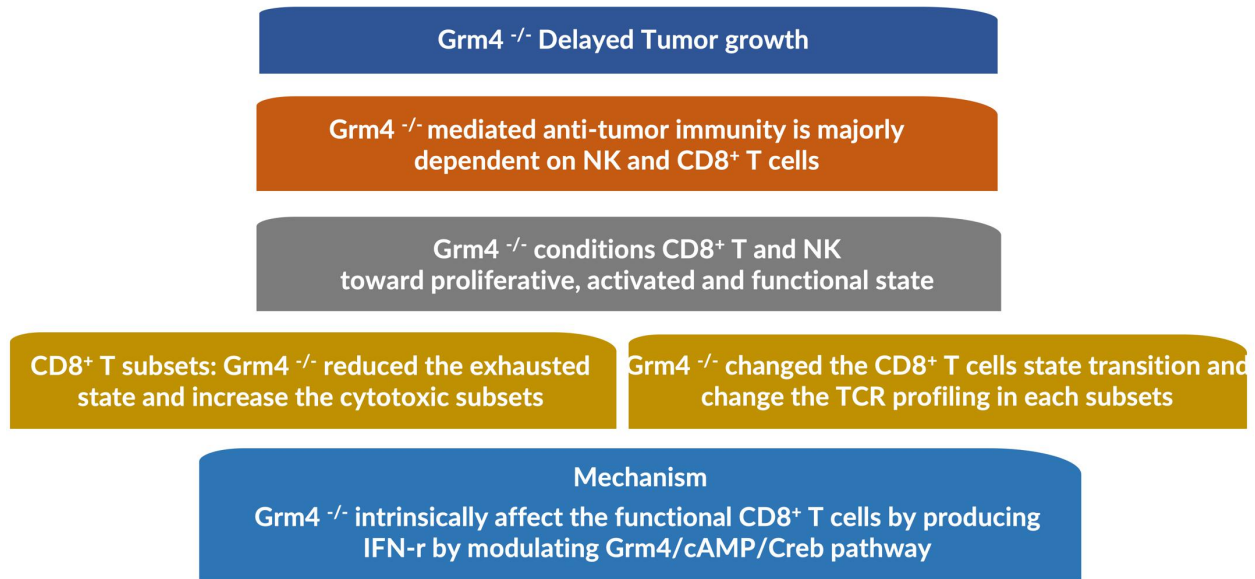


Figure 69 Overall Summary of Chapter II

In summary, in this dissertation study, we identified GRM4 as a novel therapeutic and druggable target for cancer immunotherapy. Clinical studies are urgently needed for the clinical evaluation of the effectiveness of MSOP-NPs for melanoma male patients. Due to the limited time, the complex functions of GRM4 in different gender remains unclear. More studies are needed to further define the roles of immune cells- derived Grm4 and its potential as a novel therapeutic target for cancer immunotherapy in female mice.

Despite the MSOP NPs improved the efficacy of cancer immunotherapy, this system cannot serve as a tool for convenient combination therapy. Therefore, we developed multi-functional prodrug carrier for effective combination therapy as described in chapter III. We

developed a dual-functional immuno-stimulatory polymeric prodrug carrier modified with pendent indoximod, an indoleamine 2,3-dioxygenase (IDO) inhibitor that can be used to reverse immune suppression, for co-delivery of Doxorubicin (Dox), a hydrophobic anticancer agent that can promote immunogenic cell death (ICD) and elicit antitumor immunity. The resulted carrier denoted as POEG-b-PVBIND led to significantly improved tumor regression in an orthotopic murine breast cancer model compared to both Dox-loaded POEG-b-PVB micelles (a control inert carrier) and POEG-b-PVBIND micelles alone, confirming combination effect of indoximod and Dox in improving the overall antitumor activity. On the basis of this design strategy, we aims to develop novel MSOP based polymeric prodrug system for co-delivery of other therapeutic drugs so as to achieve enhanced cancer immunotherapy. More studies will be done to characterized the novel system and combination strategies.

Bibliography

1. Mellman, I., G. Coukos, and G. Dranoff, *Cancer immunotherapy comes of age*. Nature, 2011. **480**(7378): p. 480-489.
2. McCarthy, E.F., *The toxins of William B. Coley and the treatment of bone and soft-tissue sarcomas*. The Iowa orthopaedic journal, 2006. **26**: p. 154.
3. Nam, J., et al., *Cancer nanomedicine for combination cancer immunotherapy*. Nature Reviews Materials, 2019. **4**(6): p. 398-414.
4. Storni, T., et al., *Immunity in response to particulate antigen-delivery systems*. Advanced drug delivery reviews, 2005. **57**(3): p. 333-355.
5. De Koker, S., et al., *Designing polymeric particles for antigen delivery*. Chemical Society Reviews, 2011. **40**(1): p. 320-339.
6. Kaech, S.M., E.J. Wherry, and R. Ahmed, *Effector and memory T-cell differentiation: implications for vaccine development*. Nature Reviews Immunology, 2002. **2**(4): p. 251-262.
7. Qiu, H., et al., *Nanomedicine approaches to improve cancer immunotherapy*. Wiley Interdisciplinary Reviews: Nanomedicine and Nanobiotechnology, 2017. **9**(5): p. e1456.
8. Whiteside, T.L., et al., *Emerging opportunities and challenges in cancer immunotherapy*. 2016, AACR.
9. Chen, D.S. and I. Mellman, *Elements of cancer immunity and the cancer-immune set point*. Nature, 2017. **541**(7637): p. 321-330.
10. Khair, D.O., et al., *Combining immune checkpoint inhibitors: established and emerging targets and strategies to improve outcomes in melanoma*. Frontiers in immunology, 2019. **10**.
11. Solinas, C., et al., *LAG3: The biological processes that motivate targeting this immune checkpoint molecule in human cancer*. Cancers, 2019. **11**(8): p. 1213.
12. Mochizuki, K., et al., *Various checkpoint molecules, and tumor-infiltrating lymphocytes in common pediatric solid tumors: Possibilities for novel immunotherapy*. Pediatric hematology and oncology, 2019. **36**(1): p. 17-27.
13. Sharma, P. and J.P. Allison, *The future of immune checkpoint therapy*. Science, 2015. **348**(6230): p. 56-61.
14. Topalian, S.L., C.G. Drake, and D.M. Pardoll, *Immune checkpoint blockade: a common denominator approach to cancer therapy*. Cancer cell, 2015. **27**(4): p. 450-461.
15. Brahmer, J., et al., *Nivolumab versus docetaxel in advanced squamous-cell non-small-cell lung cancer*. New England Journal of Medicine, 2015. **373**(2): p. 123-135.
16. Hodi, F.S., et al., *Improved survival with ipilimumab in patients with metastatic melanoma*. New England Journal of Medicine, 2010. **363**(8): p. 711-723.
17. Chu, C., D. Artis, and I.M. Chiu, *Neuro-immune interactions in the tissues*. Immunity, 2020. **52**(3): p. 464-474.
18. Godinho-Silva, C., et al., *Light-entrained and brain-tuned circadian circuits regulate ILC3s and gut homeostasis*. Nature, 2019. **574**(7777): p. 254-258.
19. Baral, P., et al., *Nociceptor sensory neurons suppress neutrophil and $\gamma\delta$ T cell responses in bacterial lung infections and lethal pneumonia*. Nature medicine, 2018. **24**(4): p. 417.

20. Huh, J.R. and H. Veiga-Fernandes, *Neuroimmune circuits in inter-organ communication*. Nature Reviews Immunology, 2020. **20**(4): p. 217-228.
21. Klose, C.S. and D. Artis, *Neuronal regulation of innate lymphoid cells*. Current opinion in immunology, 2019. **56**: p. 94-99.
22. Veiga-Fernandes, H. and D. Mucida, *Neuro-immune interactions at barrier surfaces*. Cell, 2016. **165**(4): p. 801-811.
23. Julio-Pieper, M., et al., *Exciting times beyond the brain: metabotropic glutamate receptors in peripheral and non-neural tissues*. Pharmacological reviews, 2011. **63**(1): p. 35-58.
24. Cryan, J.F. and K.K. Dev, *The glutamatergic system as a potential therapeutic target for the treatment of anxiety disorders*. Handbook of behavioral neuroscience, 2008. **17**: p. 269-301.
25. Conn, P.J., *Physiological roles and therapeutic potential of metabotropic glutamate receptors*. Annals of the New York Academy of Sciences, 2003. **1003**(1): p. 12-21.
26. Gerlai, R., J.C. Roder, and D.R. Hampson, *Altered spatial learning and memory in mice lacking the mGluR4 subtype of metabotropic glutamate receptor*. Behavioral neuroscience, 1998. **112**(3): p. 525.
27. Pacheco, R., et al., *Glutamate released by dendritic cells as a novel modulator of T cell activation*. The Journal of Immunology, 2006. **177**(10): p. 6695-6704.
28. Ferrarese, C., et al., *Increased glutamate in CSF and plasma of patients with HIV dementia*. Neurology, 2001. **57**(4): p. 671-675.
29. Lombardi, G., et al., *Characterization of ionotropic glutamate receptors in human lymphocytes*. British journal of pharmacology, 2001. **133**(6): p. 936-944.
30. Rezzani, R., et al., *Cyclosporine-A treatment inhibits the expression of metabotropic glutamate receptors in rat thymus*. Acta histochemica, 2003. **105**(1): p. 81-87.
31. Boldyrev, A.A., et al., *Rodent lymphocytes express functionally active glutamate receptors*. Biochemical and biophysical research communications, 2004. **324**(1): p. 133-139.
32. Hildeman, D.A., et al., *Reactive oxygen species regulate activation-induced T cell apoptosis*. Immunity, 1999. **10**(6): p. 735-744.
33. Fallarino, F., et al., *Metabotropic glutamate receptor-4 modulates adaptive immunity and restrains neuroinflammation*. Nature medicine, 2010. **16**(8): p. 897-902.
34. Besong, G., et al., *Activation of group III metabotropic glutamate receptors inhibits the production of RANTES in glial cell cultures*. Journal of Neuroscience, 2002. **22**(13): p. 5403-5411.
35. Milovanovic, J., et al., *Interleukin-17 in chronic inflammatory neurological diseases*. Frontiers in Immunology, 2020. **11**: p. 947.
36. Volpi, C., et al., *Allosteric modulation of metabotropic glutamate receptor 4 activates IDO1-dependent, immunoregulatory signaling in dendritic cells*. Neuropharmacology, 2016. **102**: p. 59-71.
37. Wan, Z., et al., *Dual functional immunostimulatory polymeric prodrug carrier with pendent indoximod for enhanced cancer immunochemotherapy*. Acta biomaterialia, 2019. **90**: p. 300-313.
38. Yan, Y., et al., *IDO upregulates regulatory T cells via tryptophan catabolite and suppresses encephalitogenic T cell responses in experimental autoimmune encephalomyelitis*. The Journal of Immunology, 2010. **185**(10): p. 5953-5961.

39. Fazio, F., et al., *Cinnabarinic acid, an endogenous agonist of type-4 metabotropic glutamate receptor, suppresses experimental autoimmune encephalomyelitis in mice*. *Neuropharmacology*, 2014. **81**: p. 237-243.
40. Fazio, F., et al., *Cinnabarinic acid, an endogenous metabolite of the kynurenine pathway, activates type 4 metabotropic glutamate receptors*. *Molecular pharmacology*, 2012. **81**(5): p. 643-656.
41. Ribeiro, M.P., J.B. Custódio, and A.E. Santos, *Ionotropic glutamate receptor antagonists and cancer therapy: time to think out of the box?* *Cancer chemotherapy and pharmacology*, 2017. **79**(2): p. 219-225.
42. Stepulak, A., et al., *Glutamate and its receptors in cancer*. *Journal of neural transmission*, 2014. **121**(8): p. 933-944.
43. Stepulak, A., et al., *Expression of glutamate receptor subunits in human cancers*. *Histochemistry and cell biology*, 2009. **132**(4): p. 435-445.
44. Ohtani, Y., et al., *Metabotropic glutamate receptor subtype-1 is essential for in vivo growth of melanoma*. *Oncogene*, 2008. **27**(57): p. 7162-7170.
45. Speyer, C.L., et al., *Riluzole mediates anti-tumor properties in breast cancer cells independent of metabotropic glutamate receptor-1*. *Breast cancer research and treatment*, 2016. **157**(2): p. 217-228.
46. Mehnert, J.M., et al., *A phase II trial of riluzole, an antagonist of metabotropic glutamate receptor 1 (GRM 1) signaling, in patients with advanced melanoma*. *Pigment cell & melanoma research*, 2018. **31**(4): p. 534-540.
47. Chang, H.J., et al., *Metabotropic glutamate receptor 4 expression in colorectal carcinoma and its prognostic significance*. *Clinical cancer research*, 2005. **11**(9): p. 3288-3295.
48. Yoo, B.C., et al., *Metabotropic glutamate receptor 4-mediated 5-Fluorouracil resistance in a human colon cancer cell line*. *Clinical cancer research*, 2004. **10**(12): p. 4176-4184.
49. Zhang, Z., et al., *Activation of type 4 metabotropic glutamate receptor promotes cell apoptosis and inhibits proliferation in bladder cancer*. *Journal of cellular physiology*, 2019. **234**(3): p. 2741-2755.
50. Park, S.-Y., et al., *Clinical significance of metabotropic glutamate receptor 5 expression in oral squamous cell carcinoma*. *Oncology reports*, 2007. **17**(1): p. 81-87.
51. Battaglia, G., et al., *Pharmacological activation of mGlu4 metabotropic glutamate receptors reduces nigrostriatal degeneration in mice treated with 1-methyl-4-phenyl-1, 2, 3, 6-tetrahydropyridine*. *Journal of Neuroscience*, 2006. **26**(27): p. 7222-7229.
52. Dröge, W., et al., *Plasma glutamate concentration and lymphocyte activity*. *Journal of cancer research and clinical oncology*, 1988. **114**(2): p. 124-128.
53. Kansara, M., et al., *Infiltrating myeloid cells drive osteosarcoma progression via GRM4 regulation of IL23*. *Cancer discovery*, 2019. **9**(11): p. 1511-1519.
54. Chan, I., et al., *Interleukin-23 is sufficient to induce rapid de novo gut tumorigenesis, independent of carcinogens, through activation of innate lymphoid cells*. *Mucosal immunology*, 2014. **7**(4): p. 842-856.
55. Lake, R.A. and B.W. Robinson, *Immunotherapy and chemotherapy—a practical partnership*. *Nature Reviews Cancer*, 2005. **5**(5): p. 397-405.
56. Gotwals, P., et al., *Prospects for combining targeted and conventional cancer therapy with immunotherapy*. *Nature Reviews Cancer*, 2017. **17**(5): p. 286-301.

57. Kroemer, G., et al., *Immunogenic cell death in cancer therapy*. Annual review of immunology, 2013. **31**: p. 51-72.
58. Munn, D.H. and V. Bronte, *Immune suppressive mechanisms in the tumor microenvironment*. Current opinion in immunology, 2016. **39**: p. 1-6.
59. Andersen, M.H., *The targeting of immunosuppressive mechanisms in hematological malignancies*. Leukemia, 2014. **28**(9): p. 1784-1792.
60. Munn, D.H. and A.L. Mellor, *IDO in the tumor microenvironment: inflammation, counter-regulation, and tolerance*. Trends in immunology, 2016. **37**(3): p. 193-207.
61. Holmgaard, R.B., et al., *Indoleamine 2, 3-dioxygenase is a critical resistance mechanism in antitumor T cell immunotherapy targeting CTLA-4*. Journal of Experimental Medicine, 2013. **210**(7): p. 1389-1402.
62. Hou, D.-Y., et al., *Inhibition of indoleamine 2, 3-dioxygenase in dendritic cells by stereoisomers of 1-methyl-tryptophan correlates with antitumor responses*. Cancer research, 2007. **67**(2): p. 792-801.
63. Monjazebe, A.M., et al., *Blocking indoleamine-2, 3-dioxygenase rebound immune suppression boosts antitumor effects of radio-immunotherapy in murine models and spontaneous canine malignancies*. Clinical cancer research, 2016. **22**(17): p. 4328-4340.
64. Muller, A.J., et al., *Inhibition of indoleamine 2, 3-dioxygenase, an immunoregulatory target of the cancer suppression gene Bin1, potentiates cancer chemotherapy*. Nature medicine, 2005. **11**(3): p. 312-319.
65. Vacchelli, E., et al., *Trial watch: IDO inhibitors in cancer therapy*. Oncoimmunology, 2014. **3**(10): p. e957994.
66. Prendergast, G.C., et al., *Discovery of IDO1 inhibitors: from bench to bedside*. Cancer research, 2017. **77**(24): p. 6795-6811.
67. Metz, R., et al., *Novel tryptophan catabolic enzyme IDO2 is the preferred biochemical target of the antitumor indoleamine 2, 3-dioxygenase inhibitory compound D-1-methyl-tryptophan*. Cancer research, 2007. **67**(15): p. 7082-7087.
68. Opitz, C.A., et al., *The indoleamine-2, 3-dioxygenase (IDO) inhibitor 1-methyl-D-tryptophan upregulates IDO1 in human cancer cells*. PloS one, 2011. **6**(5): p. e19823.
69. Ball, H.J., et al., *Indoleamine 2, 3-dioxygenase-2; a new enzyme in the kynurenine pathway*. The international journal of biochemistry & cell biology, 2009. **41**(3): p. 467-471.
70. Metz, R., et al., *IDO inhibits a tryptophan sufficiency signal that stimulates mTOR: a novel IDO effector pathway targeted by D-1-methyl-tryptophan*. Oncoimmunology, 2012. **1**(9): p. 1460-1468.
71. Soliman, H.H., et al., *A first in man phase I trial of the oral immunomodulator, indoximod, combined with docetaxel in patients with metastatic solid tumors*. Oncotarget, 2014. **5**(18): p. 8136.
72. Soliman, H.H., et al., *A phase I study of indoximod in patients with advanced malignancies*. Oncotarget, 2016. **7**(16): p. 22928.
73. Mautino, M.R., et al., *A novel prodrug of indoximod with enhanced pharmacokinetic properties*. 2017, AACR.
74. Mautino, M., et al., *Salts and prodrugs of 1-methyl-d-tryptophan*. 2017, Google Patents.
75. Xiao, B., et al., *Glutamate metabotropic receptor 4 (GRM4) inhibits cell proliferation, migration and invasion in breast cancer and is regulated by miR-328-3p and miR-370-3p*. BMC cancer, 2019. **19**(1): p. 1-10.

76. Turnis, M.E., et al., *Interleukin-35 limits anti-tumor immunity*. *Immunity*, 2016. **44**(2): p. 316-329.
77. Zhang, Y., W.Y. Kim, and L. Huang, *Systemic delivery of gemcitabine triphosphate via LCP nanoparticles for NSCLC and pancreatic cancer therapy*. *Biomaterials*, 2013. **34**(13): p. 3447-3458.
78. Dobin, A., et al., *STAR: ultrafast universal RNA-seq aligner*. *Bioinformatics*, 2013. **29**(1): p. 15-21.
79. Trapnell, C., et al., *Differential analysis of gene regulation at transcript resolution with RNA-seq*. *Nature biotechnology*, 2013. **31**(1): p. 46-53.
80. Subramanian, A., et al., *Gene set enrichment analysis: a knowledge-based approach for interpreting genome-wide expression profiles*. *Proceedings of the National Academy of Sciences*, 2005. **102**(43): p. 15545-15550.
81. Mootha, V.K., et al., *PGC-1 α -responsive genes involved in oxidative phosphorylation are coordinately downregulated in human diabetes*. *Nature genetics*, 2003. **34**(3): p. 267-273.
82. Liberzon, A., et al., *Molecular signatures database (MSigDB) 3.0*. *Bioinformatics*, 2011. **27**(12): p. 1739-1740.
83. Liu, J., et al., *An integrated TCGA pan-cancer clinical data resource to drive high-quality survival outcome analytics*. *Cell*, 2018. **173**(2): p. 400-416. e11.
84. Liang, W.S., et al., *Integrated genomic analyses reveal frequent TERT aberrations in acral melanoma*. *Genome research*, 2017. **27**(4): p. 524-532.
85. Van Allen, E.M., et al., *Genomic correlates of response to CTLA-4 blockade in metastatic melanoma*. *Science*, 2015. **350**(6257): p. 207-211.
86. Böttcher, J.P., et al., *NK cells stimulate recruitment of cDC1 into the tumor microenvironment promoting cancer immune control*. *Cell*, 2018. **172**(5): p. 1022-1037. e14.
87. Yao, C., et al., *Prostaglandin E 2 promotes Th1 differentiation via synergistic amplification of IL-12 signalling by cAMP and PI3-kinase*. *Nature communications*, 2013. **4**(1): p. 1-15.
88. Butler, A., et al., *Integrating single-cell transcriptomic data across different conditions, technologies, and species*. *Nature biotechnology*, 2018. **36**(5): p. 411-420.
89. Borchert, N., N.L. Bormann, and G. Kraus, *scRepertoire: An R-based toolkit for single-cell immune receptor analysis*. *F1000Research*, 2020. **9**.
90. Zhang, Q., et al., *Landscape and dynamics of single immune cells in hepatocellular carcinoma*. *Cell*, 2019. **179**(4): p. 829-845. e20.
91. Guo, X., et al., *Global characterization of T cells in non-small-cell lung cancer by single-cell sequencing*. *Nature medicine*, 2018. **24**(7): p. 978-985.
92. Zilionis, R., et al., *Single-cell transcriptomics of human and mouse lung cancers reveals conserved myeloid populations across individuals and species*. *Immunity*, 2019. **50**(5): p. 1317-1334. e10.
93. Tirosh, I., et al., *Dissecting the multicellular ecosystem of metastatic melanoma by single-cell RNA-seq*. *Science*, 2016. **352**(6282): p. 189-196.
94. Liu, C., et al., *Treg cells promote the SREBP1-dependent metabolic fitness of tumor-promoting macrophages via repression of CD8⁺ T cell-derived interferon- γ* . *Immunity*, 2019. **51**(2): p. 381-397. e6.

95. Satpathy, A.T., et al., *Massively parallel single-cell chromatin landscapes of human immune cell development and intratumoral T cell exhaustion*. Nature Biotechnology, 2019. **37**(8): p. 925-936.
96. Vita, M. and M. Henriksson. *The Myc oncoprotein as a therapeutic target for human cancer*. in *Seminars in cancer biology*. 2006. Elsevier.
97. Pelletier, J., G. Thomas, and S. Volarević, *Ribosome biogenesis in cancer: new players and therapeutic avenues*. Nature Reviews Cancer, 2018. **18**(1): p. 51-63.
98. Anderson, N.M., et al., *The emerging role and targetability of the TCA cycle in cancer metabolism*. Protein & cell, 2018. **9**(2): p. 216-237.
99. Weathington, N.M. and R.K. Mallampalli, *Emerging therapies targeting the ubiquitin proteasome system in cancer*. The Journal of clinical investigation, 2014. **124**(1): p. 6-12.
100. Hsu, T.Y.-T., et al., *The spliceosome is a therapeutic vulnerability in MYC-driven cancer*. Nature, 2015. **525**(7569): p. 384-388.
101. Pollak, M., *Targeting oxidative phosphorylation: why, when, and how*. Cancer cell, 2013. **23**(3): p. 263-264.
102. Kaiko, G.E., et al., *Immunological decision - making: how does the immune system decide to mount a helper T - cell response?* Immunology, 2008. **123**(3): p. 326-338.
103. Hayashi, K., et al., *Tipping the immunostimulatory and inhibitory DAMP balance to harness immunogenic cell death*. Nature Communications, 2020. **11**(1): p. 6299.
104. Lieberman, J., *Anatomy of a murder: how cytotoxic T cells and NK cells are activated, develop, and eliminate their targets*. Immunological reviews, 2010. **235**(1): p. 5-9.
105. Szabo, P.A., et al., *Single-cell transcriptomics of human T cells reveals tissue and activation signatures in health and disease*. Nature communications, 2019. **10**(1): p. 1-16.
106. Kang, Y.H., et al., *STAT1 signaling shields T cells from NK cell-mediated cytotoxicity*. Nature communications, 2019. **10**(1): p. 1-13.
107. Allen, F., et al., *CCL3 enhances antitumor immune priming in the lymph node via IFN γ with dependency on natural killer cells*. Frontiers in immunology, 2017. **8**: p. 1390.
108. Rapp, M., et al., *CCL22 controls immunity by promoting regulatory T cell communication with dendritic cells in lymph nodes*. Journal of Experimental Medicine, 2019. **216**(5): p. 1170-1181.
109. Colucci, F., et al., *Functional dichotomy in natural killer cell signaling: Vav1-dependent and-independent mechanisms*. The Journal of experimental medicine, 2001. **193**(12): p. 1413-1424.
110. Maxwell, J.R., et al., *IL-18 bridges innate and adaptive immunity through IFN- γ and the CD134 pathway*. The Journal of Immunology, 2006. **177**(1): p. 234-245.
111. Engelhardt, J.J., et al., *Marginating dendritic cells of the tumor microenvironment cross-present tumor antigens and stably engage tumor-specific T cells*. Cancer cell, 2012. **21**(3): p. 402-417.
112. Gabrilovich, D.I. and S. Nagaraj, *Myeloid-derived suppressor cells as regulators of the immune system*. Nature reviews immunology, 2009. **9**(3): p. 162-174.
113. Serrels, A., et al., *Nuclear FAK controls chemokine transcription, Tregs, and evasion of anti-tumor immunity*. Cell, 2015. **163**(1): p. 160-173.
114. Chittezhath, M., et al., *Molecular profiling reveals a tumor-promoting phenotype of monocytes and macrophages in human cancer progression*. Immunity, 2014. **41**(5): p. 815-829.

115. Kuczynski, E.A., et al., *Impact of chemical-induced mutational load increase on immune checkpoint therapy in poorly responsive murine tumors*. *Molecular cancer therapeutics*, 2018. **17**(4): p. 869-882.
116. Schoenborn, J.R. and C.B. Wilson, *Regulation of interferon - γ during innate and adaptive immune responses*. *Advances in immunology*, 2007. **96**: p. 41-101.
117. Sun, R., et al., *Eomes Impedes Durable Response to Tumor Immunotherapy by Inhibiting Stemness, Tissue Residency, and Promoting the Dysfunctional State of Intratumoral CD8+ T Cells*. *Frontiers in cell and developmental biology*, 2021. **9**: p. 1.
118. Bald, T., et al., *The NK cell–cancer cycle: advances and new challenges in NK cell–based immunotherapies*. *Nature Immunology*, 2020. **21**(8): p. 835-847.
119. Di Biase, S., et al., *Creatine uptake regulates CD8 T cell antitumor immunity*. *Journal of Experimental Medicine*, 2019. **216**(12): p. 2869-2882.
120. Takahashi, T., et al., *Immunologic self-tolerance maintained by CD25+CD4+ regulatory T cells constitutively expressing cytotoxic lymphocyte-associated antigen 4*. *J. Exp. Med*, 2000. **192**: p. 295.
121. Wu, Y., et al., *FOXP3 controls regulatory T cell function through cooperation with NFAT*. *Cell*, 2006. **126**(2): p. 375-387.
122. Seidel, J.A., A. Otsuka, and K. Kabashima, *Anti-PD-1 and anti-CTLA-4 therapies in cancer: mechanisms of action, efficacy, and limitations*. *Frontiers in oncology*, 2018. **8**: p. 86.
123. Moroishi, T., et al., *The Hippo pathway kinases LATS1/2 suppress cancer immunity*. *Cell*, 2016. **167**(6): p. 1525-1539. e17.
124. Im, S.J. and S.-J. Ha, *Re-defining T-cell exhaustion: subset, function, and regulation*. *Immune network*, 2020. **20**(1).
125. Im, S.J., et al., *Defining CD8+ T cells that provide the proliferative burst after PD-1 therapy*. *Nature*, 2016. **537**(7620): p. 417-421.
126. Nicolet, B.P., et al., *CD29 identifies IFN- γ -producing human CD8+ T cells with an increased cytotoxic potential*. *Proceedings of the National Academy of Sciences*, 2020. **117**(12): p. 6686-6696.
127. Doedens, A.L., et al., *Hypoxia-inducible factors enhance the effector responses of CD8+ T cells to persistent antigen*. *Nature immunology*, 2013. **14**(11): p. 1173.
128. Syage, A.R., et al., *Single-Cell RNA Sequencing Reveals the Diversity of the Immunological Landscape following Central Nervous System Infection by a Murine Coronavirus*. *Journal of virology*, 2020. **94**(24).
129. Thiem, A., et al., *IFN-gamma-induced PD-L1 expression in melanoma depends on p53 expression*. *Journal of Experimental & Clinical Cancer Research*, 2019. **38**(1): p. 1-15.
130. Wang, X.B., et al., *Regulation of surface and intracellular expression of CTLA - 4 on human peripheral T cells*. *Scandinavian journal of immunology*, 2001. **54**(5): p. 453-458.
131. de Goeje, P.L., et al., *Induction of peripheral effector CD8 T-cell proliferation by combination of paclitaxel, carboplatin, and bevacizumab in non–small cell lung cancer patients*. *Clinical Cancer Research*, 2019. **25**(7): p. 2219-2227.
132. Viola, A. and A. Lanzavecchia, *T cell activation determined by T cell receptor number and tunable thresholds*. *Science*, 1996. **273**(5271): p. 104-106.
133. Nozuma, S., et al., *Immunopathogenic CSF TCR repertoire signatures in virus-associated neurologic disease*. *JCI insight*, 2021. **6**(4).

134. Spitzer, M.H., et al., *Systemic immunity is required for effective cancer immunotherapy*. Cell, 2017. **168**(3): p. 487-502. e15.
135. Gutierrez, L., J. Beckford, and H. Alachkar, *Deciphering the TCR repertoire to solve the COVID-19 mystery*. Trends in pharmacological sciences, 2020.
136. Qiu, X., et al., *Reversed graph embedding resolves complex single-cell trajectories*. Nature methods, 2017. **14**(10): p. 979.
137. Woolaver, R.A., et al., *Differences in TCR repertoire and T cell activation underlie the divergent outcomes of antitumor immune responses in tumor-eradicating versus tumor-progressing hosts*. Journal for ImmunoTherapy of Cancer, 2021. **9**(1): p. e001615.
138. Fourcade, J., et al., *Upregulation of Tim-3 and PD-1 expression is associated with tumor antigen-specific CD8+ T cell dysfunction in melanoma patients*. Journal of Experimental Medicine, 2010. **207**(10): p. 2175-2186.
139. Liu, C., et al., *Neuropilin-1 is a T cell memory checkpoint limiting long-term antitumor immunity*. Nature Immunology, 2020. **21**(9): p. 1010-1021.
140. Mombaerts, P., et al., *RAG-1-deficient mice have no mature B and T lymphocytes*. Cell, 1992. **68**(5): p. 869-877.
141. Conn, P.J. and J.-P. Pin, *Pharmacology and functions of metabotropic glutamate receptors*. Annual review of pharmacology and toxicology, 1997. **37**(1): p. 205-237.
142. Samten, B., et al., *CREB, ATF, and AP-1 transcription factors regulate IFN- γ secretion by human T cells in response to mycobacterial antigen*. The Journal of Immunology, 2008. **181**(3): p. 2056-2064.
143. Roper, R.L., B. Graf, and R.P. Phipps, *Prostaglandin E2 and cAMP promote B lymphocyte class switching to IgG1*. Immunology letters, 2002. **84**(3): p. 191-198.
144. Li, J., et al., *MiR-335 is involved in major depression disorder and antidepressant treatment through targeting GRM4*. Neuroscience letters, 2015. **606**: p. 167-172.
145. Shah, R., et al., *Concurrent Targeting of Glutaminolysis and Metabotropic Glutamate Receptor 1 (GRM1) Reduces Glutamate Bioavailability in GRM1+ Melanoma*. Cancer research, 2019. **79**(8): p. 1799-1809.
146. Wang, Y., et al., *Down regulation of c-FLIPL Enhance PD-1 blockade Efficacy in B16 Melanoma*. Frontiers in oncology, 2019. **9**: p. 857.
147. De Henau, O., et al., *Overcoming resistance to checkpoint blockade therapy by targeting PI3K γ in myeloid cells*. Nature, 2016. **539**(7629): p. 443-447.
148. Caldwell, J., I. Gardner, and N. Swales, *An introduction to drug disposition: the basic principles of absorption, distribution, metabolism, and excretion*. 1995, Sage Publications Sage CA: Thousand Oaks, CA.
149. Savage, S.A., et al., *Genome-wide association study identifies two susceptibility loci for osteosarcoma*. Nature genetics, 2013. **45**(7): p. 799-803.
150. Paccani, S.R., et al., *Suppression of T-lymphocyte activation and chemotaxis by the adenylate cyclase toxin of Bordetella pertussis*. Infection and immunity, 2008. **76**(7): p. 2822-2832.
151. Conche, C., et al., *T cell adhesion primes antigen receptor-induced calcium responses through a transient rise in adenosine 3' , 5' -cyclic monophosphate*. Immunity, 2009. **30**(1): p. 33-43.
152. Schnurr, M., et al., *Extracellular nucleotide signaling by P2 receptors inhibits IL-12 and enhances IL-23 expression in human dendritic cells: a novel role for the cAMP pathway*. Blood, 2005. **105**(4): p. 1582-1589.

153. Iacovelli, L., et al., *Native group - III metabotropic glutamate receptors are coupled to the mitogen - activated protein kinase/phosphatidylinositol - 3 - kinase pathways*. Journal of neurochemistry, 2002. **82**(2): p. 216-223.
154. Jiang, Q., Z. Yan, and J. Feng, *Activation of group III metabotropic glutamate receptors attenuates rotenone toxicity on dopaminergic neurons through a microtubule-dependent mechanism*. Journal of Neuroscience, 2006. **26**(16): p. 4318-4328.
155. Xu, X., et al., *Calcium phosphate nanoparticles-based systems for siRNA delivery*. Regenerative Biomaterials, 2016. **3**(3): p. 187-195.
156. Klein, S.L. and K.L. Flanagan, *Sex differences in immune responses*. Nature Reviews Immunology, 2016. **16**(10): p. 626-638.
157. Munn, D.H. and V. Bronte, *Immune suppressive mechanisms in the tumor microenvironment*. Curr Opin Immunol, 2016. **39**: p. 1-6.
158. Lake, R.A. and B.W. Robinson, *Immunotherapy and chemotherapy—a practical partnership*. Nature Reviews Cancer, 2005. **5**(5): p. 397.
159. Holmgaard, R.B., et al., *Indoleamine 2, 3-dioxygenase is a critical resistance mechanism in antitumor T cell immunotherapy targeting CTLA-4*. Journal of Experimental Medicine, 2013: p. jem. 20130066.
160. Muller, A.J., et al., *Inhibition of indoleamine 2, 3-dioxygenase, an immunoregulatory target of the cancer suppression gene Bin1, potentiates cancer chemotherapy*. Nature medicine, 2005. **11**(3): p. 312.
161. Gotwals, P., et al., *Prospects for combining targeted and conventional cancer therapy with immunotherapy*. Nat Rev Cancer, 2017. **17**(5): p. 286-301.
162. Kroemer, G., et al., *Immunogenic cell death in cancer therapy*. Annu Rev Immunol, 2013. **31**: p. 51-72.
163. Lake, R.A. and B.W. Robinson, *Immunotherapy and chemotherapy--a practical partnership*. Nat Rev Cancer, 2005. **5**(5): p. 397-405.
164. Senkus, E., et al., *Primary breast cancer: ESMO Clinical Practice Guidelines for diagnosis, treatment and follow-up*. Ann Oncol, 2015. **26 Suppl 5**: p. v8-30.
165. Sun, J., et al., *A Multi-Functional Polymeric Carrier for Simultaneous Positron Emission Tomography Imaging and Combination Therapy*. Acta biomaterialia, 2018.
166. Sun, J., et al., *Doxorubicin delivered by a redox-responsive dasatinib-containing polymeric prodrug carrier for combination therapy*. Journal of Controlled Release, 2017. **258**: p. 43-55.
167. Qu, Y., et al., *Recent progress in functional micellar carriers with intrinsic therapeutic activities for anticancer drug delivery*. Journal of biomedical nanotechnology, 2017. **13**(12): p. 1598-1618.
168. Chen, Y., et al., *An immunostimulatory dual-functional nanocarrier that improves cancer immunochemotherapy*. Nature communications, 2016. **7**: p. 13443.
169. Dolušić, E., et al., *Tryptophan 2, 3-dioxygenase (TDO) inhibitors. 3-(2-(pyridyl) ethenyl) indoles as potential anticancer immunomodulators*. Journal of medicinal chemistry, 2011. **54**(15): p. 5320-5334.
170. Liu, X., et al., *Selective inhibition of indoleamine 2, 3-dioxygenase (IDO1) effectively regulates mediators of anti-tumor immunity*. Blood, 2010: p. blood-2009-09-246124.
171. Brincks, E., et al., *Indoximod modulates AhR-driven transcription of genes that control immune function*. Ratio, 2018. **1**: p. 0.25.

172. Chang, M.Y., et al., *Cardiac and gastrointestinal liabilities caused by deficiency in the immune modulatory enzyme indoleamine 2, 3-dioxygenase*. *Cancer biology & therapy*, 2011. **12**(12): p. 1050-1058.
173. 'Mac'Cheever, M.A., *Twelve immunotherapy drugs that could cure cancers*. *Immunological reviews*, 2008. **222**(1): p. 357-368.
174. Godin-Ethier, J., et al., *Indoleamine 2, 3-dioxygenase expression in human cancers: clinical and immunologic perspectives*. *Clinical cancer research*, 2011.
175. Prendergast, G.C., et al., *Discovery of IDO1 Inhibitors: From Bench to Bedside*. *Cancer Res*, 2017. **77**(24): p. 6795-6811.
176. Prendergast, G.C., et al., *Indoleamine 2, 3-dioxygenase pathways of pathogenic inflammation and immune escape in cancer*. *Cancer immunology, immunotherapy*, 2014. **63**(7): p. 721-735.
177. Bahary, N., et al., *Phase 2 trial of the indoleamine 2, 3-dioxygenase pathway (IDO) inhibitor indoximod plus gemcitabine/nab-paclitaxel for the treatment of metastatic pancreas cancer: Interim analysis*. 2016, American Society of Clinical Oncology.
178. Jackson, E., et al., *A phase I study of indoximod in combination with docetaxel in metastatic solid tumors*. 2013, American Society of Clinical Oncology.
179. Soliman, H.H., et al., *A phase I study of Ad. p53 DC vaccine in combination with indoximod in metastatic solid tumors*. 2013, American Society of Clinical Oncology.
180. Soliman, H.H., et al., *A phase 2 study of docetaxel in combination with indoximod in metastatic breast cancer*. 2014, American Society of Clinical Oncology.
181. Zakharia, Y., et al., *A phase I/II study of the combination of indoximod and temozolomide for adult patients with temozolomide-refractory primary malignant brain tumors*. 2014, American Society of Clinical Oncology.
182. Zakharia, Y., et al., *Abstract CT117: interim analysis of the phase 2 clinical trial of the IDO pathway inhibitor indoximod in combination with pembrolizumab for patients with advanced melanoma*. 2017, AACR.
183. Calleja, P., et al., *A combination of nanosystems for the delivery of cancer chemoimmunotherapeutic combinations: 1-Methyltryptophan nanocrystals and paclitaxel nanoparticles*. *Pharmacological research*, 2017. **126**: p. 77-83.
184. Lu, J., et al., *Nano-enabled pancreas cancer immunotherapy using immunogenic cell death and reversing immunosuppression*. *Nature communications*, 2017. **8**(1): p. 1811.
185. Yu, S., et al., *Injectable Bioresponsive Gel Depot for Enhanced Immune Checkpoint Blockade*. *Advanced Materials*, 2018: p. 1801527.
186. Xu, J., et al., *Pendant HDAC inhibitor SAHA derivatised polymer as a novel prodrug micellar carrier for anticancer drugs*. *Journal of drug targeting*, 2018. **26**(5-6): p. 448-457.
187. Song, X., et al., *Development of a multi-target peptide for potentiating chemotherapy by modulating tumor microenvironment*. *Biomaterials*, 2016. **108**: p. 44-56.
188. Huang, Y., et al., *C ring may be dispensable for β -carboline: design, synthesis, and bioactivities evaluation of tryptophan analog derivatives based on the biosynthesis of β -carboline alkaloids*. *Bioorganic & medicinal chemistry*, 2016. **24**(3): p. 462-473.
189. Yoo, H.S. and T.G. Park, *Biodegradable polymeric micelles composed of doxorubicin conjugated PLGA-PEG block copolymer*. *Journal of controlled Release*, 2001. **70**(1-2): p. 63-70.

190. Duong, H.H.P. and L.-Y.L. Yung, *Synergistic co-delivery of doxorubicin and paclitaxel using multi-functional micelles for cancer treatment*. International journal of pharmaceuticals, 2013. **454**(1): p. 486-495.
191. Lee, E.S., K. Na, and Y.H. Bae, *Doxorubicin loaded pH-sensitive polymeric micelles for reversal of resistant MCF-7 tumor*. Journal of controlled release, 2005. **103**(2): p. 405-418.
192. Zhu, J., et al., *Identification of novel pathways in idelalisib metabolism and bioactivation*. Chemical research in toxicology, 2018. **31**(7): p. 548-555.
193. Zhao, J., et al., *Hyaluronic Acid Layer-By-Layer (LbL) Nanoparticles for Synergistic Chemo-Phototherapy*. Pharmaceutical research, 2018. **35**(10): p. 196.
194. YANG, Q., et al., *A reversible decomposition approach for the formation of injectable, excipient - free, self - assembling nanocrystals*. Chemical Communications, 2019.
195. Yi, X., et al., *Co-delivery of pirarubicin and paclitaxel by human serum albumin nanoparticles to enhance antitumor effect and reduce systemic toxicity in breast cancers*. Molecular pharmaceuticals, 2015. **12**(11): p. 4085-4098.
196. Jiang, K., et al., *Enhanced antitumor and anti-metastasis efficacy against aggressive breast cancer with a fibronectin-targeting liposomal doxorubicin*. Journal of Controlled Release, 2018. **271**: p. 21-30.
197. Song, X., et al., *A Submicron Emulsion for Intravenous Injection of 7-Ethyl-10-Hydroxycamptothecin: Characterization, Pharmacokinetic and Biodistribution Studies, In Vitro and In Vivo Antitumor Effect*. LATIN AMERICAN JOURNAL OF PHARMACY, 2016. **35**(6): p. 1369-1377.
198. WAN, Z., *TUNABLE IMMUNOSTIMULATORY NANOCARRIER FOR IMPROVING CANCER IMMUNOCHEMOTHERAPY*. 2017, University of Pittsburgh.
199. Awuah, S.G., et al., *A Pt (IV) pro-drug preferentially targets indoleamine-2, 3-dioxygenase, providing enhanced ovarian cancer immuno-chemotherapy*. Journal of the American Chemical Society, 2015. **137**(47): p. 14854-14857.
200. Sun, J., et al., *A prodrug micellar carrier assembled from polymers with pendant farnesyl thiosalicylic acid moieties for improved delivery of paclitaxel*. Acta biomaterialia, 2016. **43**: p. 282-291.
201. Shi, Y., et al., *π - π stacking induced enhanced molecular solubilization, singlet oxygen production, and retention of a photosensitizer loaded in thermosensitive polymeric micelles*. Advanced healthcare materials, 2014. **3**(12): p. 2023-2031.
202. Shi, Y., C.F. van Nostrum, and W.E. Hennink, *Interfacially Hydrazone cross-linked thermosensitive polymeric micelles for acid-triggered release of paclitaxel*. ACS Biomaterials Science & Engineering, 2015. **1**(6): p. 393-404.
203. Rosenblum, D., et al., *Progress and challenges towards targeted delivery of cancer therapeutics*. Nature communications, 2018. **9**(1): p. 1410.
204. Huo, M., et al., *Tumor-targeted delivery of sunitinib base enhances vaccine therapy for advanced melanoma by remodeling the tumor microenvironment*. Journal of Controlled Release, 2017. **245**: p. 81-94.
205. Zhou, C., et al., *A novel honokiol liposome: formulation, pharmacokinetics, and antitumor studies*. Drug development and industrial pharmacy, 2018. **44**(12): p. 2005-2012.
206. Pack, D.W., et al., *Design and development of polymers for gene delivery*. Nature reviews Drug discovery, 2005. **4**(7): p. 581.

207. Patil, M.L., M. Zhang, and T. Minko, *Multifunctional triblock nanocarrier (PAMAM-PEG-PLL) for the efficient intracellular siRNA delivery and gene silencing*. ACS nano, 2011. **5**(3): p. 1877-1887.
208. Murakami, T. and R. Yumoto, *Role of phosphatidylserine binding in tissue distribution of amine-containing basic compounds*. Expert opinion on drug metabolism & toxicology, 2011. **7**(3): p. 353-364.
209. Chander, A., et al., *Lung lamellar bodies maintain an acidic internal pH*. Journal of Biological Chemistry, 1986. **261**(13): p. 6126-6131.
210. Tan, T., et al., *Deep Tumor - Penetrated Nanocages Improve Accessibility to Cancer Stem Cells for Photothermal - Chemotherapy of Breast Cancer Metastasis*. Advanced Science, 2018. **5**(12): p. 1801012.
211. Cui, X., et al., *Enhanced Chemotherapeutic Efficacy of Paclitaxel Nanoparticles Co-delivered with MicroRNA-7 by Inhibiting Paclitaxel-Induced EGFR/ERK pathway Activation for Ovarian Cancer Therapy*. ACS applied materials & interfaces, 2018. **10**(9): p. 7821-7831.
212. Feng, B., et al., *Binary Cooperative Prodrug Nanoparticles Improve Immunotherapy by Synergistically Modulating Immune Tumor Microenvironment*. Advanced Materials, 2018: p. 1803001.
213. Gabrilovich, D.I. and S. Nagaraj, *Myeloid-derived suppressor cells as regulators of the immune system*. Nature reviews immunology, 2009. **9**(3): p. 162.